8-1-2018

Computational Study of Free Jets Emanating from Circular and Lobed Orifice-Lattice Boltzmann Method

Yang Chen
Lehigh University, yac310@lehigh.edu

Recommended Citation

Chen, Yang, "Computational Study of Free Jets Emanating from Circular and Lobed Orifice-Lattice Boltzmann Method" (2018). *Theses and Dissertations*. 4269.
https://preserve.lehigh.edu/etd/4269

Computational Study of Free Jets Emanating from Circular and Lobed Orifice-Lattice Boltzmann Method

by

Yang Chen

A Dissertation

Presented to the Graduate and Research Committee

of Lehigh University

in Candidacy for the Degree of

Doctor of Philosophy

in

Mechanical Engineering

Lehigh University

August 2018

DISSERTATION SIGNATURE SHEET

Approved and recommended for acceptance as a dissertation in partial fulfillment of the requirements for the degree of Doctor of Philosophy.

____
Date

____
Dr. Alparslan Oztekin
Dissertation Director

____
Accepted Date

Committee Members:

____
Dr. Alparslan Oztekin

____
Dr. Yue Yu

____
Dr. Edmund Webb III

____
Dr. Yaling Liu

ACKNOWLEDGEMENTS

There are many people, whom I would like to acknowledge for their support, suggestions and help. I express extraordinary respect to my great two advisors. I would first like to thank Dr. Alparslan Oztekin and Dr. Yue Yu for their patient guidance, solid support and meticulous help. Alp's solid background and extreme research experience helped me expand my academic breadth. Yue gave me patient suggestions about Mathematic modeling and coding and helped me significantly on code debugging. I also would like to appreciate Dr. Edmund Webb III and Dr. Yaling Liu for serving as committee members for this dissertation. I also wish to thank Dr. Xiaoyi He, one of the top experts in the field of Lattice Boltzmann Method around the world and my PhD internship supervisor at Air Products & Chemicals.

Through some emotional moments, some great friends I made at Lehigh give me tremendous help not only about the academic research and about mental support. Wei Wei, Haolin Ma, Guosong Zeng, Shengmeng Rong, Weina Wang, Xiao Ma and Jia Liu became good friends, inspiring each other with brilliant ideas, sharing both happiness and sadness and material and spiritual help.

I would also like to thank my parents, Yuangang Chen and Jinchuan Shi, for all their support and love all the time during my whole doctoral journey. They are always my spiritual support.

Thanks Lehigh for all the wonderful memories.

TABLE OF CONTENTS

LIST OF TABLES

LIST OF FIGURES

ABSTRACT

The Lattice Boltzmann method is an effective computational fluid dynamics tool to study complex flows. Unlike conventional numerical schemes based on discretization of macroscopic continuum equations, the Lattice Boltzmann method is based on particles and mesoscopic kinetic equations. Single-Relaxation Time Lattice Boltzmann Method (SRTLBM) with Smagorinsky LES model is applied to simulate high Reynolds number jet flows of single and multiphase flows emanating. The multi-block approach is implemented to refine the mesh when the high resolution is needed in the region around the core jet. An 2nd order accurate interface treatment between neighboring blocks is derived to satisfy the conservation of mass momentum and the continuity of the stresses across the interface. The bounce back boundary condition and curve boundary condition using extrapolation approach based on the idea of bounce back of the non-equilibrium part is implemented to impose the velocity boundary conditions at surfaces. The core jet length, velocity decay, turbulence intensity, vortex generation, jet breakup and noise spectrum analysis are studied for both circular and lobed jet orifices for a range of Reynolds number from 1000 to 72000. The pseudopotential Shan/Chen model Lattice Boltzmann Method is applied to study the small density ratio at low Reynold’s number and low Weber number liquid jet breakup of the water/silicon oil multiphase fluid. Multiphase jet flow simulations at high Reynold’s number and high Weber number are performed by utilizing OpenFOAM and predicted results are compared with results of documented experimental measurements.

NOMENCLATURES

f	Distribution function
f^{eq}	Equilibrium distribution function
SRT	Single-Relaxation time
e	Lattice directional velocity
Ω	Collision term
X	Spatial coordinate
t	Time
τ	Relaxation time
ρ	Density
u	Bulk velocity of the fluid
w	Weighting factor
c	Lattice speed
∂_t	Differential time operator
c_s	Speed of sound
ϑ	Kinematic viscosity
ϑ_{eddy}	Turbulent viscosity
$S_{\alpha\beta}$	Filtered strain rate tensor
C_s	Smagorinsky constant
Re	Reynolds number
T	Time step
f^{neq}	Non-equilibrium distribution function
F	Interaction force
g	Gravity acceleration
R	Gas constant
T	Temperature
a	Attractive parameter
b	Repulsion parameter
AR	Aspect ratio
D_e	Equivalent diameter
L	Length of domain
W	Width of domain

H	Height of domain
St	Strouhal number
S/D	Normalized distance by diameter of cylinder
U^*	Normalized velocity
Z/D	Normalized distance by diameter of jet orifice
TI	Turbulence intensity
f	Frequency in Hz
rms	Root-mean square
$\bar{k}$	Turbulence kinetic energy
G	Strength of interaction force
P	Pressure
γ_ρ	Density ratio
γ_ϑ	Kinematic viscosity ratio
We	Weber number
Fr	Froude number
Oh	Ohnesorege’s number

Subscripts

α	Lattice branch
x	x coordinate
y	y coordinate
z	z coordinate
w	water
o	oil

Greek’s Symbol

Δ	Difference
∇	Gradient
ψ	Effective mass
σ	Surface tension
θ	Contact angle

Chapter 1

Introduction

1.1 Motivation

Single and multiphase jets emanating from circular and lobed orifices are encountered in a number of diverse applications. Some of typical applications include air supply for mechanical ventilation in buildings, heat exchangers in industrial processes, aircraft propulsion, etc. Such flows are useful because of their intrinsic properties of providing an efficient mixing by exchanging mass, momentum and/or heat. Liquid-liquid jet flows appear in many natural and industrial processes, e.g., chemical processing and industrial gas storage in oceans. Especially in the nuclear engineering field, the interaction between melt and coolant must be well understood for the safety design of nuclear reactors. Although the air jet and liquid-liquid jets issued from circular and lobed orifices are well studied using computational and experimental methods, there are still outstanding issues to be addressed Lattice Boltzmann Method can be used to study these flows. Compared with other macroscopic CFD methods based on the Naiver-Stokes equations solvers, Lattice Boltzmann Method focuses on microscopic kinetic equations and offers several advantages. First, the macroscopic mass and momentum is calculated from the discretized distribution functions of each node, which is related to the local neighboring nodes. Second, Lattice Boltzmann Method is easy to be implemented for flow in complex geometries. Third, parallel computing using sub domain with Message Passing Interface approach can be effectively applied to solve Lattice

Boltzmann governing equations. Fourth, comparing with VOF method, pseudopotential Lattice Boltzmann Method for multi-phase flow simulations can dispose phases separations automatically avoiding tracking the fluid phase fracture.

1.2 Literature Review

The Lattice Boltzmann method is widely used to simulate complex flow problems. Unlike conventional numerical schemes based on discretization of macroscopic continuum equations, the Lattice Boltzmann method is based on microscopic models and mesoscopic kinetic equations.

The kinetic nature of the LBM introduces three important features that distinguish it from other numerical methods such as finite element method (FEM) and finite difference method (FDM). First, the convection operator (the streaming process) of the LBM in phase space (velocity space) is linear. This feature is borrowed from the kinetic theory and contrasts with the nonlinear convection terms in other approaches that use a macroscopic representation. Simple convection combined with a relaxation operator (the collision process) of the LBM allows the recovery of the nonlinear macroscopic advection through multi-scale expansions. Second, the incompressible Naiver-Stokes (NS) equations can be obtained in the nearly incompressible limit of LBM. The pressure of LBM is calculated by using an equation of state. In contract, in the direct numerical simulation of the incompressible NS equations, the pressure satisfies a Poisson equation with velocity strains acting as sources. Solving this equation for the pressure often produces numerical difficulties, which requires special treatment, such as iteration or relaxation. Third, the LBM utilizes a minimal set of velocities in phase space. Because only one or two speeds and a few directions are used in LBM, the transformation relates to the microscopic distribution function and macroscopic quantities is greatly simplified and required of simple arithmetic calculations. Additionally, most properties in Lattice Boltzmann method are local, which means a large matrix calculation is not needed. For each lattice, mass and momentum are calculated by 9 local discretized distribution populations (or nineteen for three-dimensional model). In addition, Lattice Boltzmann Method can be easily parallelized [1] [2] [3].

In the literature, the lattice Boltzmann equation with the single-relaxation-time (SRT) approximation also known as Bhavnagar-Gross-Krook (BGK) model [4], is the most popular, accurate and efficient scheme. However, the simplicity of the lattice BGK model comes at the expense of numerical instability and inaccuracy in implementing boundary conditions, especially with high Reynolds number flows. These deficiencies in the LBGK models can be overcome with the use of SRT-LES model [5]. In the Smagorinsky model, the sub-grid stress is determined with the strain-rate tensor from the non-equilibrium moments [6].

Several treatments for the curve solid boundary condition are researched, e.g. Guo et al., [7]; Ladd, 1994 [8]; Mei et al., 1999 [9]; He et al. [10]. In the present study of single phase fluid flow, an extrapolation method developed by Guo et al. is adopted for the jet emanating from circular orifice. This treatment has been proved to be of the second order accuracy and has well-behaved stability characteristics.

Considering the simulation efficiency and computational cost, a low-resolution LBM simulation runs on a coarse grid and models global flow behavior of the entire domain with low consumption of computational resources. For regions of inner volume including jet orifice, LBM simulation is performed on fine grids, which are superposed on the coarse one [11]. The global simulation on the coarse grids determines the flow properties on boundaries of the fine grids. Thus, the locally refined fine-grid simulations follow the global fluid behavior and model the desired small-scale and turbulent flow motion with their denser numerical discretization [12]. Besides the performance improvement of the adaptive simulation, the locally refined LBM is suitable for acceleration on parallel computing (openMPI).

The pseudopotential model presented by Shan and Chen in 1993 [13], is the most widely used LBM for multi-phase flow problems. The basic concept is to obtain the microscopic molecular interactions at the mesoscopic scale using an effective mass depending on the local microscopic density. With such interaction forces, the fluid flow separates into two phases with high and low densities when the interaction force strength is modified under critical values. Such automatic phase separation is an attractive character as the phase interface is no longer a mathematical boundary and no explicit interface tracking or capturing is needed [14]. The densities change smoothly from one bulk value to another across the phase interface, which usually occupied several lattice nodes. Due to its computational efficiency, and clear representation of microscopic physics, this pseudopotential model has been successfully applied into a wealth of research fields such as fluid mixing, energy, environment, biology and geology [15].

1.3 Dissertation structure

In this study, we implement the Lattice Boltzmann Method to investigate single-phase and multi-phase jet flow issued from circular and lobed jet orifices. Simulations are conducted for a widely range of Reynolds number. The jet breakup phenomenon and vortex generation shall be studied for the air jet and water/silicon oil liquid-liquid systems. The numerical method is detailed in Chapter 2 with a summary included for the algorithm employed. In Chapter 3, the results of single-phase air jet flows issued from circular and lobed orifices are presented. In Chapter 4, the results of large density ratio droplets and liquid-liquid system jet breakup simulations are presented. Conclusion and outlook for future research and investigations are presented in Chapter 5.

Chapter 2

Mathematical Model and Numerical Algorithm

2.1 Single-relaxation time Lattice Boltzmann Method with LES model

In D3Q19 lattice configuration, space is discredited into a cube lattice, and there are 19 discrete velocities. Lattice Boltzmann governing equation yields:

$$f_\alpha(x + e_\alpha \nabla t, t + \nabla t) - f_\alpha(x, t) = \Omega_\alpha \tag{1}$$

$$e_\alpha = \begin{cases} (0,0,0), & \alpha = 0 \\ (\pm1,0,0), (0,\pm1,0), (0,0,\pm1), & \alpha = 1 - 6 \\ (\pm1,\pm1,0), (\pm1,0,\pm1), (0,\pm1,\pm1), & \alpha = 7 - 18 \end{cases} \tag{2}$$

where $f_\alpha(x, t)$ is the distribution function at computing node x at time t, and $f_\alpha(x + e_\alpha \nabla t, t + \nabla t)$ is the distribution function after advection and changes due to Ω_α. Ω_α satisfies conservation laws and be compatible with the symmetry of the model.

For the single-relaxation time collision term yields

$$\Omega_\alpha = -\frac{1}{\tau}[f_\alpha(x, t) - f_\alpha^{eq}(x, t)] \tag{3}$$

where τ is the dimensionless relaxation time, and $f_\alpha^{eq}(x, t)$ is the equilibrium distribution function defined as:

$$f_\alpha^{eq}(x, t) = w_\alpha \rho[1 + \left(\frac{3\overrightarrow{e_\alpha}\cdot\vec{u}}{c^2} + \frac{9(\overrightarrow{e_\alpha}\cdot\vec{u})^2}{c^4} - \frac{3}{2}\frac{u^2}{c^2}\right)] \tag{4}$$

where ρ is the local density, and $c = \frac{\nabla x}{\nabla t} = 1$ (in lattice unit). The speed of sound is $c_s = c/\sqrt{3}$. The weighting factors w_α for the D3Q19 are $w_0 = \frac{1}{3}, w_{1-6} = \frac{1}{18}, w_{7-18} = \frac{1}{36}$.

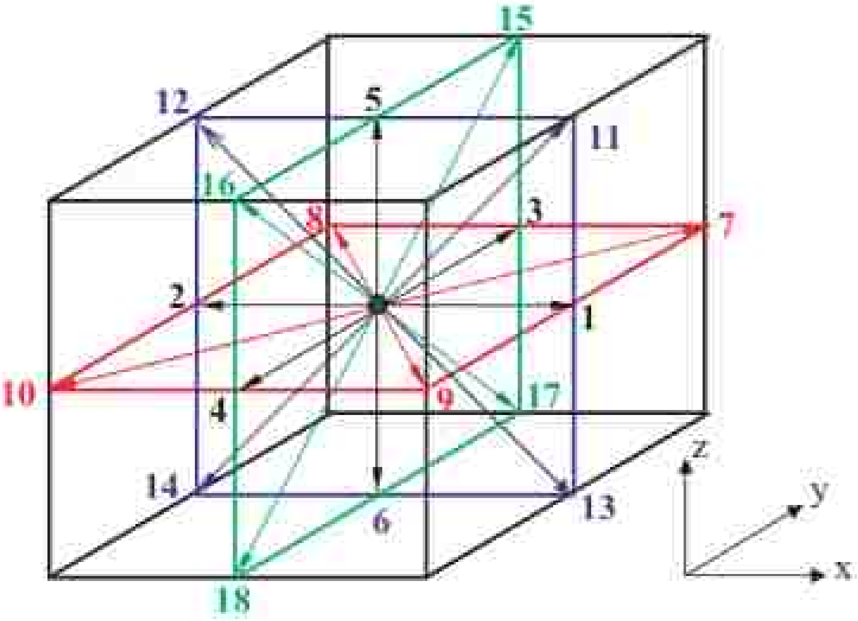

Figure 1 D319 lattice units velocity directions on cube lattice

The mass and momentum conservations are strictly enforced

$$\rho = \sum_{\alpha=0}^{18} f_\alpha \tag{5}$$

$$\rho u = \sum_{\alpha=0}^{18} f_\alpha \cdot e_\alpha \tag{6}$$

The hydrodynamic equations derived from above equations via the Chapman-Enskog analysis are

$$\partial_t \rho + \vec{\nabla} \cdot \rho \vec{u} = 0 \tag{7}$$

$$\partial_t \vec{u} + \vec{u} \cdot \vec{\nabla} \vec{u} = -\vec{\nabla} p + \vartheta \nabla^2 \vec{u} + \vec{a} \tag{8}$$

Where $p = c_s^2 \rho/\rho_0$ and the kinematic viscosity ϑ has the following relation with the relaxation time

$$\vartheta = \frac{1}{3}(\tau - \frac{1}{2}) \tag{9}$$

The LES method is a powerful tool in numerical simulation of turbulent flows. The basic idea of LES is based on the following assumptions: the small-scale structures of sub-grid flow field is not sensitive to the large-scale structures of flow field, neither to the influence of boundary conditions. Therefore, small-scale structures are more general, and easier to model [6].

For LES turbulence model, $\vartheta_{total} = \vartheta + \vartheta_{eddy}$, where ϑ and ϑ_{eddy} are the molecular viscosity and turbulent viscosity (or eddy viscosity), respectively. In the Smagorinsky model, the eddy viscosity ϑ_{eddy} is determined with the filtered strain rate tensor $S_{\alpha\beta} = (\partial_\alpha u_\beta + \partial_\beta u_\alpha)/2$, a filter length scale Δ_x and the Smagorinsky constant C_s [6]:

$$S_{ij} \approx \frac{-3}{2\rho c^2 \tau \Delta t} Q_{ij} \tag{10}$$

where $Q_{ij} = \sum_\alpha e_{\alpha,i} e_{\alpha,j} (f_\alpha - f_\alpha^{eq})$.

For convenience, we use the notation f_α and S_{ij} to denote the filtered variables of the resolved scale in the LBM-LES algorithm. The eddy kinematic viscosity can be calculated according to Smagorinsky model [16]:

$$\vartheta_{eddy} = (C_s \Delta_x)^2 \bar{S}, \bar{S} = \sqrt{2S\colon S} \tag{11}$$

In the LBM-LES algorithm, the relationship between the non-dimensional relaxation time and the kinematic viscosity is

$$\vartheta = \frac{1}{3}(\tau - 0.5)c^2 \Delta t,\ \vartheta_{total} = \vartheta + \vartheta_{eddy} = \frac{1}{3}[(\tau + \tau_{eddy)} - 0.5)]c^2 \Delta t \tag{12}$$

τ_{eddy} can be determined from (11) and (12):

$$\tau_{total} = 0.5\left[\sqrt{\tau^2 + 18(C_s\Delta x)^2(\rho c^4\Delta t^2)^{-1}\sqrt{2\sum_{i,j} Q_{ij}Q_{ij}}} - \tau\right] \tag{13}$$

2.2 Multi-block approach in Lattice Boltzmann Method

When the high resolution around the core jet is needed, the multi-block approach is used. An accurate interface treatment between neighboring blocks is derived by He et al [17], to satisfy the conservation of mass momentum and the continuity of stresses across the interface.

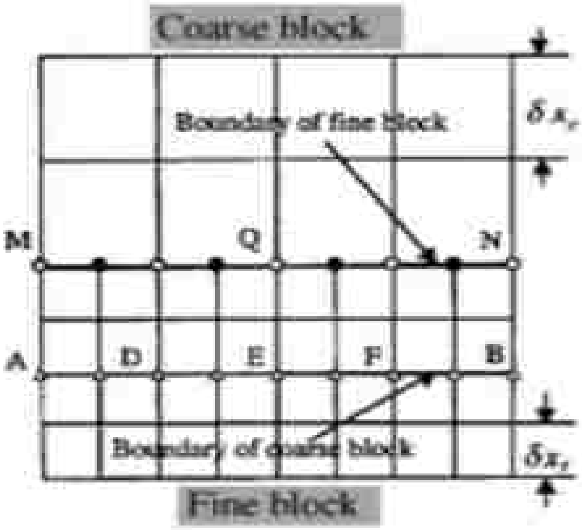

Figure 2 Interface structure between two blocks of different lattice spacing

To illustrate the basic idea of grid refinement in our simulation, a horizontal plane three-block (coarse block, finer block and finest block) system as shown in Figure 2 is considered in the derivation for the interface information exchange. The ratio of the lattice space between the neighboring two blocks is

$$n = \delta x_c/\delta x_f \tag{14}$$

For a given Re, in order to keep a consistent viscosity $\vartheta = (2\tau - 1)\delta_x/6$, the relation between relaxation times τ_f on the fine block and τ_c on the coarse block must obey [18]

$$\tau_f = \frac{1}{2} + n(\tau_c - \frac{1}{2}) \tag{15}$$

Since the velocity and density are continuous across the interface between two blocks, the equilibrium part across the interface follow:

$$f_\alpha^{eq,c}(x,t)\text{=}f_\alpha^{eq,f}(x,t) \tag{16}$$

In the LBER-LES with non-uniform mesh, we set ${C_s}^2 = 0.16$, and $\Delta_x\text{=}\ \delta_x$ for each blocks, which means $\Delta_x^c\text{=}\ \delta_x^c = 1$ for coarse block, $\Delta_x^{finer}\text{=}\ \delta_x^{finer} = 1/2$ for finer block and $\Delta_x^{finest}\text{=}\ \delta_x^{finest} = 1/4$ for finest block.

At the interface, the spatial and temporal interpolation is needed [9]. The typical transverse surface structure is shown in Figure2. The time step size of a LBM simulation is partially defined by the grid spacing, which is the spacing between two neighboring grid sites. For LBM simulation, the computations on the coarse grid and fine grid must be synchronized. The fine grid must perform the computations with several smaller steps to advance its simulation to the same time, as well as the simulation proceeds with one large time step on the coarse grid. At first, the global simulation on the coarse grid is running with a large time step t_c, from the initial time T_1 to time T_3. Synchronously, the fine grid simulation is starting from time T_1 to T_2. When the fine grid simulation starts at time T_2, it runs with a smaller time step $t_f(t_c = 2t_f)$. The coarse grid computation does not provide the values of the particle distributions f_i, on the interfaces at time T_2 due to its large time step size. Therefore, we perform a temporal interpolation to compute f_i at time T_2 from the global computation results on the coarse grid at time T_1 and T_3, with the following scheme [12]:

$$f_\alpha^c(x, T_2) = \left(1 - \frac{t_f}{t_c}\right) f_\alpha^c(x, T_1) + \frac{t_f}{t_c} f_\alpha^c(x, T_3) \tag{17}$$

After the temporal interpolation, we have computed the particle distributions of grid sites on the coarse grid at time T_2. However, we still need more information for fine grid on the interface, which is the 'ghost point'. Therefore, we execute a spatial interpolation to compute ghost point for fine grid on the interface with the second order 2D Lagrange interpolation [19].

2.3 Boundary condition

The bounce back boundary condition based on the idea of bounce back of the non-equilibrium part is implemented [20]. The primary boundary conditions are involved: no-slip boundary wall, periodic boundaries, and curve boundaries using extrapolation approach [7].

Considering the uniform velocity flow field, the velocity boundary condition for the LBGK model is implemented. As D2Q9 LBGK example, the boundary is aligned with f_1, f_5, f_8 pointing into the domain. After streaming, $f_0, f_2, f_3, f_4, f_6, f_7$ are known. Suppose that $u_x = u_{in}, u_y = 0$ are specified on the wall and we want to use Eq. to determine f_1, f_5, f_8 and ρ, which can be put into the form

$$f_1 + f_5 + f_8 = \rho - (f_0 + f_2 + f_4 + f_3 + f_6 + f_7) \tag{18}$$

$$f_1 + f_5 + f_8 = \rho u_x + (f_3 + f_6 + f_7) \tag{19}$$

$$f_5 - f_8 = f_4 - f_2 + f_7 - f_6 \tag{20}$$

Equations (18-20) satisfy

$$\rho = \frac{(f_0 + f_2 + f_4 + 2(f_3 + f_6 + f_7))}{1 - u_x} \tag{21}$$

We use the bounce back rule for the non-equilibrium part of the particle distribution normal to the inlet, to find $f_1 - f_1^{eq} = f_3 - f_3^{eq}$. With f_1 known, f_5, f_8 are obtained by the remaining two equations:

$$f_1 = f_3 + \frac{2}{3}\rho u_x \tag{22}$$

$$f_5 = f_7 - \frac{(f_2 - f_4)}{2} + \frac{\rho u_x}{6} \tag{23}$$

$$f_8 = f_6 + \frac{(f_2 - f_4)}{2} + \frac{\rho u_x}{6} \tag{24}$$

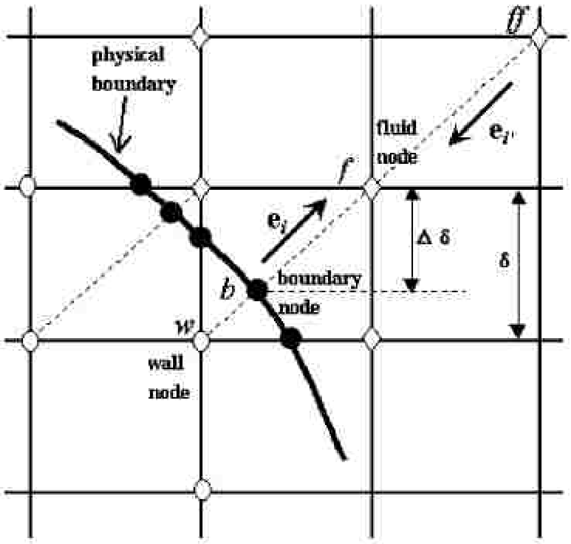

Figure 3 Lattice nodes of curved boundary

In evolution, the distribution functions at the boundaries need to be specified according to the conditions for the macroscopic variables. Here we consider the velocity boundary conditions at the wall and use extrapolation method to apply the curve boundary condition at the circular boundary of the orifice. As it is shown in Figure 3, the link between the fluid node x_f and solid node x_s intersects the curve wall at the node x_w. The fraction of the intersected link in the fluid region is defined as $\Delta = \frac{|X_f - X_w|}{|X_s - X_w|}$. After the collision step, the distribution functions $f_\partial(x_f, t)$ at the fluid node x_f are known, however, we also need to know the distribution function

$f_\partial(x_w, t)$ at the solid node x_w that moves from x_w to x_f in the streaming step. The so-called boundary condition here is to get $f_\partial(x_w, t)$. The basic idea of the extrapolation method is to decompose $f_\partial(x_w, t)$ into the equilibrium and non-equilibrium functions. The equilibrium part could be determined by a fictitious equilibrium distribution, while the non-equilibrium part is approximated by that of neighboring fluid node along the link. Thus, the distribution function at the node x_w could be expressed as:

$$f_\alpha(x_w, t) = f_\alpha^{eq}(x_w, t) + f_\alpha^{neq}(x_w, t) \tag{25}$$

in the above equation, the equilibrium distribution could be approximated by a fictitious one:

$$f_\alpha^{eq}(x_w, t) = w_\alpha \rho[1 + \left(\frac{3\overrightarrow{e_\alpha}\cdot\vec{u}_w}{c^2} + \frac{9(\overrightarrow{e_\alpha}\cdot\vec{u}_w)^2}{c^4} - \frac{3}{2}\frac{u_w{}^2}{c^2}\right)] \tag{26}$$

with the velocity at the solid node could be chosen as followed relations:

$$u_w = \begin{cases} [u_b + (\Delta - 1)u_f]/\Delta, & \Delta \geq \Delta_c \\ u_b + (\Delta - 1)u_f + \frac{\frac{1-\Delta}{1+\Delta}[2u_b + (\Delta-1)u_{ff}]}{1+\Delta}, & \Delta < \Delta_c \end{cases} \tag{27}$$

while Δ_c is the judgment parameter and in the current study $\Delta_c = 0.65$ [7].

The non-equilibrium part could be approximated by the non-equilibrium part of the distribution function at the fluid nodes x_f and x_{ff}:

$$f_\alpha^{neq}(x_w, t) = \begin{cases} f_\alpha(x_f, t) - f_\alpha^{eq}(x_f, t), & \Delta \geq \Delta_c \\ \Delta\left(f_\alpha(x_f, t) - f_\alpha^{eq}(x_f, t)\right) + (1 - \Delta)\left(f_\alpha(x_{ff}, t) - f_\alpha^{eq}(x_{ff}, t)\right), & \Delta < \Delta_c \end{cases} \tag{28}$$

2.4 pseudopotential Lattice Boltzmann Model

As a mesoscopic method with microscopic models, Lattice Boltzmann method (LBM) has an instinct kinetic nature and only involves simple algorithm with collision-streaming processes. The phase segregation and surface tension in multiphase flow are due to the interparticle forces/microscopic interactions. The LBM is capable of incorporating these interactions without tracking/capturing the interface between immiscible phases/components. Hence, the LBM attracted attention in simulating multiphase flow. Shan and Chen [13] developed a potential multiphase LB model for multiphase and multi-component flows with introducing inter-particle interaction forces between fluid particles at neighboring lattice sites. The interaction potentials control the form of the equation of state (EOS) of the fluid. Phase separation occurs automatically when the interaction potentials are properly chosen. This interaction force includes two parts for the multi-component fluid. One is the interaction between molecules from the same component, $\vec{F}_{i,i}$, and another is the interaction between molecules from different components, $\vec{F}_{i,j}$, which are calculated by the interaction potential. However, this pseudopotential model cannot satisfy the momentum conservation law at a local position and limited by the density ratio (maximum value is 10). In 2006, Yuan and Schaeffer [21] developed a relatively simple but effective method to incorporate various EOS into the pseudo potential model. The general idea is to associate the effective mass with different EOS i.e. vdW-EOS, C-S EOS and P-R EOS. The density ratio is only one defining characteristic of a MCMP flow system. A water-air system and an oil-air system perform very differently, although they have a similar density ratio. To capture these effects, the viscosity and the surface tension are two important factors [22]. For solid and wetting boundary, an additional force term should be introduced to the fluid-solid interaction, $\vec{F}_{s,i}$, which is dominated by above effective mass and an indicator function that equals 1 for solid nodes and 0 for fluid nodes. Hence, the total force on each particle can be expressed as:

$$\vec{F}_{total,i} = \vec{F}_{\sigma,\sigma} + \vec{F}_{\sigma,\overline{\sigma}} + \vec{F}_{b,\overline{\sigma}} + \vec{F}_{s,\overline{\sigma}} \quad (29)$$

These forces are represents respectively as shown below.

$$F_{\sigma,\overline{\sigma}}(X) = -c_0\psi_\sigma(X)g_{\sigma\overline{\sigma}}\nabla\psi_{\overline{\sigma}}(X) \quad (30)$$

$$F_{\sigma,\sigma}(X) = -c_0\psi_\sigma(X)g_{\sigma\sigma}\nabla\psi_\sigma(X) \quad (31)$$

where c_0 is a constant that depends on the lattice structure. For the D2Q9 and D3Q19 lattices, $c_0 = 6.0$, and for the D3Q15 lattice, $c_0 = 10.0$ [22]. The coefficients for the strength of the interparticle force are $\mathrm{g}_{\sigma\overline{\sigma}}$ and $\mathrm{g}_{\sigma\sigma}$, with negative value representing an attractive force between particles and positive value a repulsive force [23].

$$F_{b,\sigma}(X) = \Delta\rho g \quad (32)$$

where g is the acceleration of gravity,

$$F_{s,\sigma}(X) = g_w\psi(\rho_\sigma)\sum_{\alpha=1}^{N} w(|e_\alpha|^2)\,\psi(\rho_{solid})s(x+e_\alpha)e_\alpha \quad (33)$$

where $\mathrm{g_w}$ determines the strength of the interaction force between fluid and solid. In most studies employing the MCMP pseudopotential model, the interaction strength within each component, namely $g_{\sigma\sigma}\ and\ g_{\overline{\sigma}\overline{\sigma}}$ is set as zero, and only the interaction between different components $g_{\sigma\overline{\sigma}}$ contributes to the phase separation. Unfortunately, by using only one free parameter $g_{\sigma\overline{\sigma}}$ to control the two-fluid system, the density ratio between the components is only unit and the maximum kinematic viscosity ratio achievable is less than 5 [15]. These forces can be incorporated into the model by shifting the velocity in the equilibrium distribution. This means that the velocity $\vec{u}$ in the equilibrium equation is replaced by

$$\vec{u}_i^{eq} = \vec{u}_i + \frac{\tau_i\vec{F}_{total,i}}{\rho_i(\vec{x})} \quad (34)$$

Unlike in the original Shan and Chen model, the coefficient of interaction strength within a component ($g_{i,i}$) here cannot control the overall interaction strength.

However, the coefficient of interaction strength between different components ($g_{i,j}$) is very important for creating and extending the MCMP LBE model. The behavior of interactions between different components is mainly controlled by this force, so the interaction can be adjusted through changing the value of $g_{i,j}$. For MCMP model, this force usually plays a critical role in adjusting the system density ratio, which need to be investigated and explained in different cases.

The effective of mass can be defined as:

$$\psi_{\sigma}(\rho) = \sqrt{\frac{2(P_{\sigma} - c_s^2)}{c_0 g_{\sigma\sigma}}} \tag{35}$$

where p is the pressure. We implement Peng-Robinson (P-R) EOS into the effective mass, because P-R EOS provided a maximum increase in the density ratio while maintaining small spurious currents around the interface. The P-R EOS is expressed as:

$$P = \frac{\rho RT}{1 - b\rho} - \frac{a\alpha(T)\rho^2}{1 + 2b\rho - b^2\rho^2} \tag{36}$$

$$\alpha(T) = [1 + (0.37464 + 1.5422\omega - 0.26992\omega^2)(1 - \sqrt{T/T_c})]^2 \tag{37}$$

with a $= \frac{0.4572R^2T_c^2}{P_c}, b = \frac{0.07788T_c}{P_c}$, where a is the attractive parameter, b is the repulsion parameter, R is the gas constant, ω is the acentric factor, and T_c and $P_c$are the critical temperature and critical pressure, respectively. T is the temperature, since only isothermal systems are considered in our validation case, we set T as a constant, which equals 1.

2.5 openMPI parallel algorithm

The Message Passing Interface (MPI) is a message-passing library based on a distributed parallel programming model and achieves a process-level parallelism. It employs message passing for the necessary communication between the processes running in parallel, to achieve parallelization of programs. Each of the processes involved has its own resources different from the others'. A process can send a message or data to another process and receive data from another process.

A process can send a message to all other processes in its" communication world" or in its group and gather data from them as well.

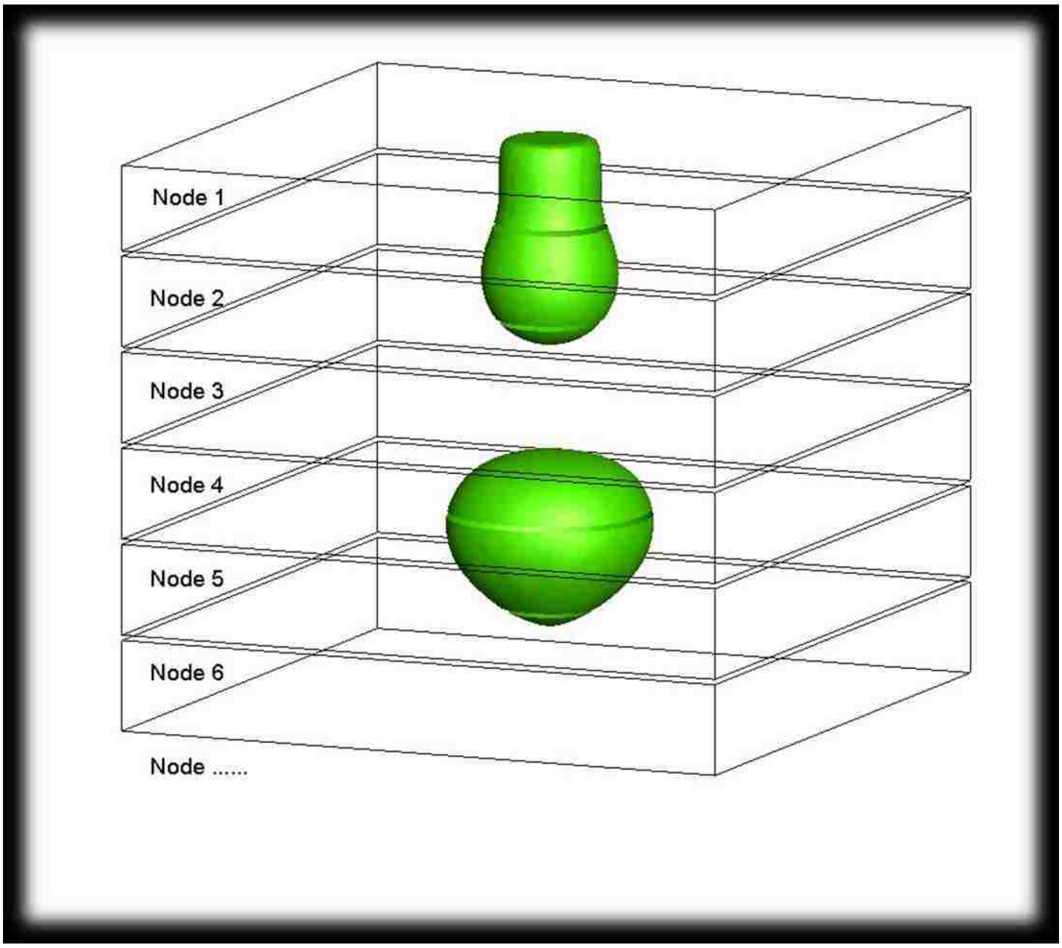

Figure 4 Schematic of domain decomposition along streamwise direction for openMPI parallel computing algorithm

We use C++ and openMPI library to implement parallel computing for the multi-phase LBM simulations. Figure 4 shows the concept of decomposition of the whole domain along the streamwise direction. With the definition of nodes number and rank size using, *MPI_Comm_size(MPI_COMM_WORLD, &numnodes);*

MPI_Comm_rank(MPI_COMM_WORLD, &mynode);

the whole domain is divided into couple segmentations and with several interfaces between two neighboring sub-domains created. The distribution functions on the interface of each node are packed as two-dimensional arrays and stored temporally. All the information transfer to the arrays of the interfaces belong to the neighboring nodes with *MPI_SEND* using same tag. Meanwhile, the arrays receive all the information on the interfaces belong to the neighboring nodes with *MPI_RECV* using a different tag. After the transfer process, all the information is unpacked to the original four-dimensional distribution functions, then the LBM algorithm proceeds in every single node independently.

2.6 Summary

Our Lattice Boltzmann Method solver is build and developed using C++ based on classic BGK Lattice Boltzmann Method. In the solver, the multi-block is included for mesh refinement, and we use this approach to refine the mesh for simulations of the single-phase air jet flow issued from circular and lobed orifice. Results of these simulations are presented and discussed in Chapter 3. For high Reynolds number cases, the LES turbulence model is modified in our solver. In our single-phase and multi-phase jet breakup simulations, the LES model is applied. For the curve boundary, we implement the extrapolation approach to modify the circular jet orifice boundary condition. For water-silicon oil jet investigations, we build the multi-phase module using original Shan/Chen model. Using the benchmark of the static droplet without gravity force, Laplace analysis and three-dimensional droplet including gravity force, we validated our multi-phase Lattice Boltzmann solver. We implemented the solver in liquid-liquid jet breakup simulations. Results of these simulations are presented and discussed in Chapter 4. Our single-phase simulations are parallelized using openMP and multi-phase simulations are parallelized using openMPI.

Chapter 3

Single-phase jet from circular and lobed orifice

3.1 Introduction

In the modern industry, air jets are widely used for diverse applications: including air supply for mechanical ventilation in buildings, heat exchange in industrial processes and aircraft propulsion, etc. Such flows are useful because of their intrinsic properties of providing an efficient mixing by exchanging mass, momentum, heat. These flows are also encountered often since it is easily to generate them.

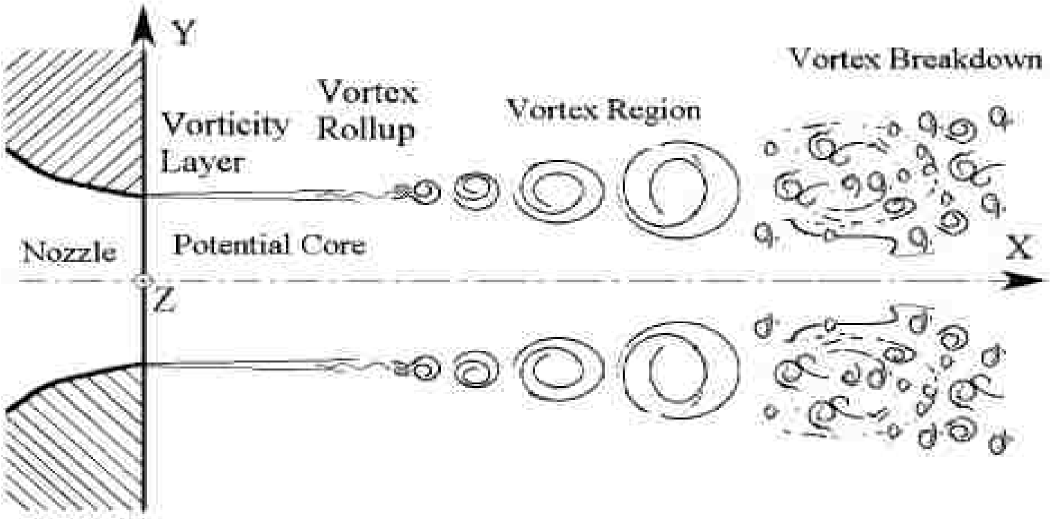

Figure 5 Sketch of expected topology of circular free jet

Figure 5 displays a schematic diagram of the expected general topology of a free circular jet [24]. With the orifice, the jet is blown with an nearly uniform flow velocity W_0 into the stationary ambient air. The vorticity layer rolls up, generating vortex and providing regularity of formation and evolution [25].

The shear layer structure influences the uniform core, that result in oscillation and reduction in the local mean velocity [26]. The generated vortices move downstream with the shear layer, due to the interaction between the jet core and ambient air [27]. The organized vortices break down, become unstable, decay to smaller structures, and eventually tune into fully developed turbulence. The decay can be triggered in two ways: 1) for low Reynolds number, the vortices are more likely to survive until the end of the potential core, where the inner border rotation region is met. In such case, the structure is symmetric and unstable [28]; 2) for higher Reynolds number flow, the evolution of the vortices is more rapid than the previous case. The decay starts before the "self-closure", therefore the large-scale structure cannot be observed around the later part of the core. The distance, from the exit section required for the roll-up, evolution, and decay of the vortices, is based on the Reynolds number and the thickness boundary layer [24].

For rectangular jets with an aspect ratio greater than 1, the azimuthal curvature variation of initial vertical structures produces non-uniform self-induction and three-dimensional structures. As a result, these flows spread out to the ambient with greater rate in the plane through the minor axis of their orifice exit than the one through major axis. In other words, as such flow proceeds downstream, the mean-flow cross-section tends to flip the minor and major axes at a certain distance from the orifice [29].

In noncircular jets studies, the axisymmetric lobed jet orifice geometry is usually included. It is applied as a baseline to quantify the relative mixing performance and to describe the behavior of the noncircular jet [30]. Two types of instabilities are mainly presented in the simulations of asymmetric lobed jet: the primary Kelvin-Helmholtz instability (K-H) and secondary-type instability. The growing of the K-H structures results in the secondary-type instabilities of the braid between two successive rings [31]. Thus, it appears that the production of streamwise structures in the round jet is governed by the K-H rings. Unlike the circular jet, the streamwise structures in the non-circular jet are generated by the transverse shear that is induced by the shape of the orifice, and may dominate the mixing phenomenon [32].

The main objective of this research is to investigate the mixing processes of the circular and lobed jets by studying the spread speed, the vortex generation, the core jet length, the main jet breakup, and the turbulence effects in the near fields of jet orifice. Next, we compare flow-fields of the circular and lobed jets in the near and transition fields. Boundary conditions, hydraulic diameters of the orifice and, Reynolds number are matched for comparisons of the circular and lobed. It aims at reporting the instantaneous/mean flow fields and the turbulence Reynolds stresses to quantify the differences/similarities between them.

In this chapter, we implement the single-phase Lattice Boltzmann Method along with LES turbulence model to handle high Reynold's number jet flows. To reduce the computational requirement, the multi-block approach has been applied to refine the mesh around the core jet and jet orifice.

Single-phase jet flow simulations are conducted using openMP (for parallel computing) on 16-core workstation. The total resolution with refined mesh is about 30 million and the total run time for each case is around 140 hours.

Source codes and post-processing codes are developed in C++ and run on Linux systems. Flow images are generated by TECPLOT.

[redacted]

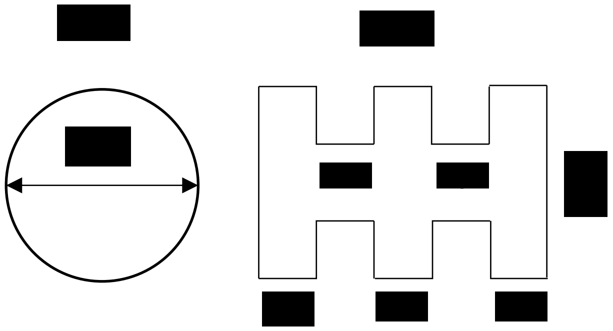
[redacted] [redacted] [redacted] [redacted] [redacted] [redacted] [redacted] [redacted] [redacted]

Figure 6 Schematic representation of jet nozzle exit for circular and 6-lobde case; (a) Diameter of circular orifice exits; (b) equivalent diameter of 6-lobed nozzle exit

Figure 6 shows the shape and dimensions of the two orifice plates used in the present study. For the circular jet orifice, the orifice cross-section AR, is 1, and the hydraulic diameter is 40mm. The computational domain for the circular jets matches the experimental setup of Todde. V. et, al [24]. For the 6-lobed jet, the orifice cross-section AR, is 1.5. The hydraulic diameter is $D_e = 12mm$, which is similar to the experimental setup of by Mi. et, al [33]. Figure 7 illustrates the schematic diagram of the computational domain and boundary conditions imposed for the single-phase circular and 6-lobed jet flow simulations, and the details are discussed in the following sections.

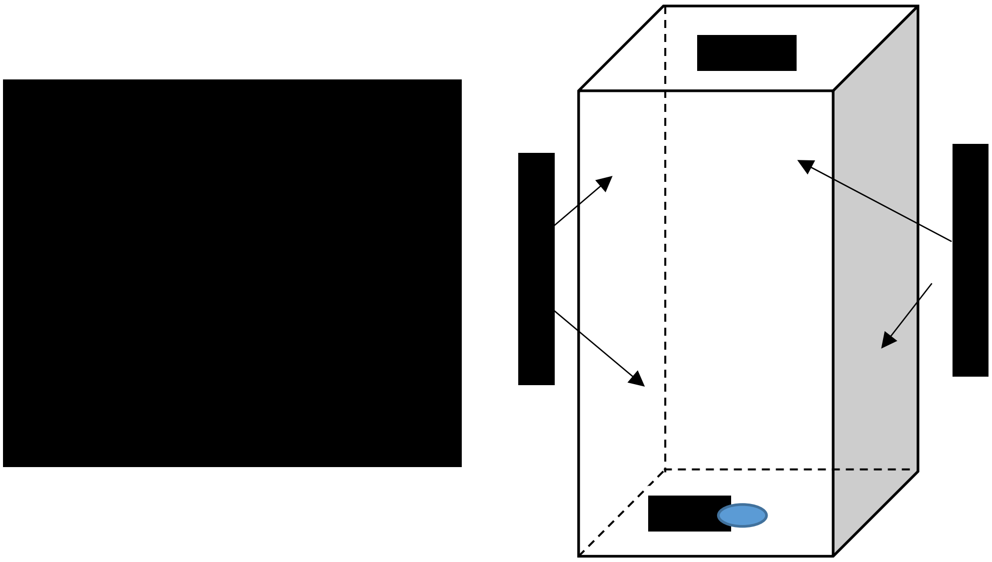

[redacted]
[redacted]
[redacted]
[redacted]
[redacted]

Figure 7 boundary conditions for single-phase circular and 6-lobed jet simulation

3.2 Single-phase jet from circular orifice

3.2.1 Simulation Setup

Reynolds number for different jet flow cases are listed in Table 1. The dimensions of the flow domain are 0.2m(L)*0.2m(W)*0.8m(H). The jet orifice is located at the center of the bottom plane, and the orifice has the hydraulic diameter D_e = 40 mm related to the exit area S, with definition of $D_e = \sqrt{4S/\pi}$. The Reynolds number Re_D is based on the hydraulic diameter and the uniform inlet velocity varying from 0.4 m/s to 26.7 m/s.

Table 1 Uniform exit velocity and actual exit Reynolds Number (built with the equiseta diameter and the exit velocity)

Test Case	Uniform exit velocity (m/s)	Exit Reynolds Number, $\mathbf{Re_D}$
1	0.4	1050
2	0.62	1620
3	1.0	2700
4	1.5	4050
5	2.5	6750

We impose a non-dimensional uniform velocity and density (pressure) profile for the jet at the exit of the orifice: $\mathrm{w}_0 = 0.1$ and $\rho_0 = 1.0$ ($P = c * \rho_0$). The desired Reynolds number is selected, then the molecular viscosity ϑ_0 is achieved with $w_0 = 0.1$ and $D_e = 20$ (in lattice units). Initially, the system is set at a quiescent state with $\rho = \rho_0 = 1.0$ and $\mathrm{u} = \mathrm{v} = \mathrm{w} = 0$ everywhere except at the jet orifice, where $w = w_0\hat{z}$.

With the refined mesh and time step, the actual simulation time step is 0.002s, and the early stage results during 0-12s for all cases are shown in the following sections. Because for the downstream field fluids to reach fully developed state requires much longer domain length along streamwise direction than our setup, we present the near fields fluid flow visualizations and flow profiles in the results discussion section.

3.2.2 Mesh Refinement

In the application of LBM, one limitation to the numerical efficiency is that it is constrained by a special uniform lattice. The challenge of the uniform grid is how to offer high resolution near the jet orifice and core jet regions. It is desired to split the computational domain into grid blocks: within each block, uniform lattice spacing can be performed. For the grid block near jet orifice and core jet regions, the lattice separation is minimized, while the spacing could be large near the outer regions. The blocks are connected through the interfaces. An accurate interface treatment between neighboring blocks can be derived to satisfy the conservation of mass and momentum and the continuity of stresses across the interface [12].

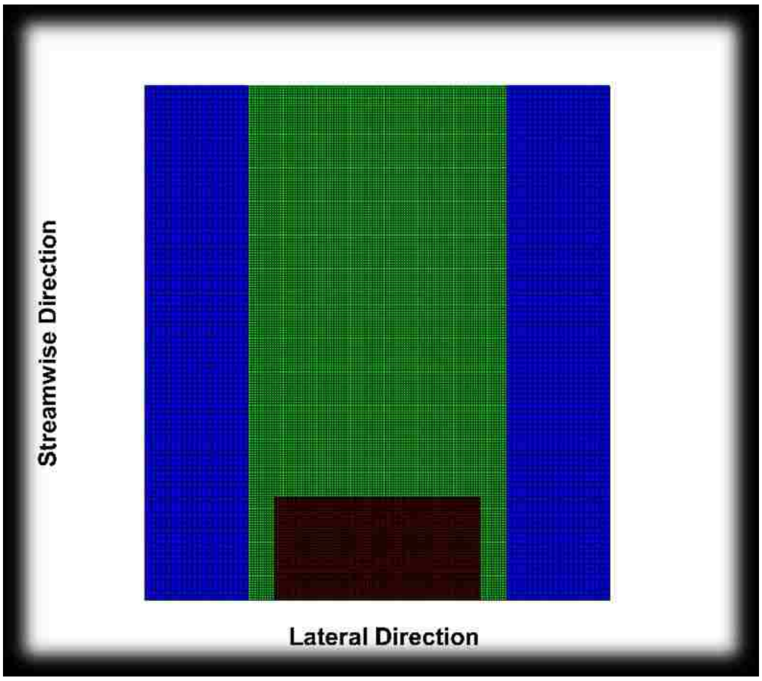

Figure 8 Structured mesh shown in XZ plane view

In the single-phase simulations, the domain size is two times finer in the fine block than that in the coarse one, which means the finer block contains 2 times finer mesh at the sub-block refined domain.

Between coarse, fine and finer blocks, two interfaces are introduced and need to be considered for the distribution functions transfer between each interface.

The information of the coarse block nodes is stored on the interface between two neighboring blocks temperately:

$$\begin{cases} f_{store}^{coarse}(a,i,j,k) = f_{interface}^{coarse}(a,i,j,k), \\ f_{store}^{eq,coarse}(a,i,j,k) = f_{interface}^{eq,coarse}(a,i,j,k) \end{cases} \quad (38)$$

$$\begin{cases} f_{store}^{finer}(a,i,j,k) = f_{interface}^{finer}(a,i,j,k), \\ f_{store}^{eq,finer}(a,i,j,k) = f_{interface}^{eq,finer}(a,i,j,k) \end{cases} \quad (39)$$

It's then transferred from the temporarily storage to the fine blocks. However, some nodes on the interface of finer blocks do not exist on the interface of coarse blocks. Such nodes are so-called “Ghost nodes”. In order to get the information of the ghost nodes for coarse blocks, both spatial and temporal interpolation is necessary to get the distribution function on the ghost nodes. For the spacing interpolation, considering the viscosity terms, a 2nd order two-dimensional interpolation is applied:

Forward one-dimensional interpolation for interface sides:

$$f_{store}(a,i,j) = \\ \big(3f_{store}(a,i,j-1) + 6f_{store}(a,i,j+1) - f_{store}(a,i,j+3)\big) \tag{40}$$

Backward one-dimensional interpolation for interface sides:

$$f_{store}(a,i,j) = \\ \big(-f_{store}(a,i,j-3) + 6 * f_{store}(a,i,j-1) + 3 * f_{store}(a,i,j+1)\big) \tag{41}$$

Forward two-dimensional interpolation for the inner interface:

$$f_{store}(a,i,j) = \\ \big(9 * f_{store}(a,i-1,j-1) + 18 * f_{store}(a,i+1,j-1) - 3 * f_{store}(a,i+3,j-1) + \\ 18 * f_{store}(a,i-1,j+1) + 36 * f_{store}(a,i+1,j+1) - 6 * f_{store}(a,i+3,j+1) - \\ 3 * f_{store}(a,i-1,j+3) - 6 * f_{store}(a,i+1,j+3) + f_{store}(a,i+3,j+3)\big)/64 \tag{42}$$

Backward two-dimensional interpolation for the inner interface:

$$f_{store}(a,i,j) = \\ \big(-3 * f_{store}(a,i-3,j-1) + 18 * f_{store}(a,i-1,j-1) + 9 * f_{store}(a,i+1,j-1) - \\ 6 * f_{store}(a,i-3,j+1) + 36 * f_{store}(a,i-1,j+1) + 18 * f_{store}(a,i+1,j+1) + \\ f_{store}(a,i-1,j+3) - 6 * f_{store}(a,i-1,j+3) - 3 * f_{store}(a,i+1,j+3)\big)/64 \tag{43}$$

For the temporal interpolation, a 1st order one-dimensional interpolation is adopted.

After the interpolation for ghost nodes, all the information is transferred from the temporally storage including the ghost nodes to the finer block side interface by:

$$f^{finer}(a,i,j,k) = f^{coarse}_{store}(a,i,j,k) \\ + \left(\frac{1}{ref}\right)\left(\frac{\Omega_{coarse}}{\Omega_{finer}}\right)\left(\frac{1-\Omega_{finer}}{1-\Omega_{coarse}}\right)\left(f^{eq,coarse}_{store}(a,i,j,k) - f^{coarse}_{store}(a,i,j,k)\right) \tag{44}$$

Where ref is the refined times. In the solver, we use ref=2.

The calculation algorithm starts once the fine and finer blocks receive all the information from the interfaces. After the algorithm update the inside of the fine blocks, the information for the next time step is transferred back to the coarse blocks by:

$$f^{coarse}(a,i,j,k) = f_{store}^{finer}(a,i,j,k)$$

$$+(ref)*\left(\frac{\Omega_{finer}}{\Omega_{coarse}}\right)*\left(\frac{1-\Omega_{coarse}}{1-\Omega_{finer}}\right)\left(f_{interface}^{eq,finer}(a,i,j,k)-f_{interface}^{finer}(a,i,j,k)\right) \quad (45)$$

The flow chart of the computational procedure for the multi-block Lattice Boltzmann Method is shown in Figure 9 [12].

In our single-phase simulations, the whole domain is refined within three non-uniform meshes using multi-block approach as shown in Figure 8. The red region is the finest block around the jet orifice; the green region is the fine block relatively far from the jet orifice and around the core jet areas; the blue regions are the coarse blocks that away from the jet orifice and core jet areas. Because of the periodic boundary condition implanted for all four sides, the influence from coarse blocks near the side boundaries to the inside domain is acceptable.

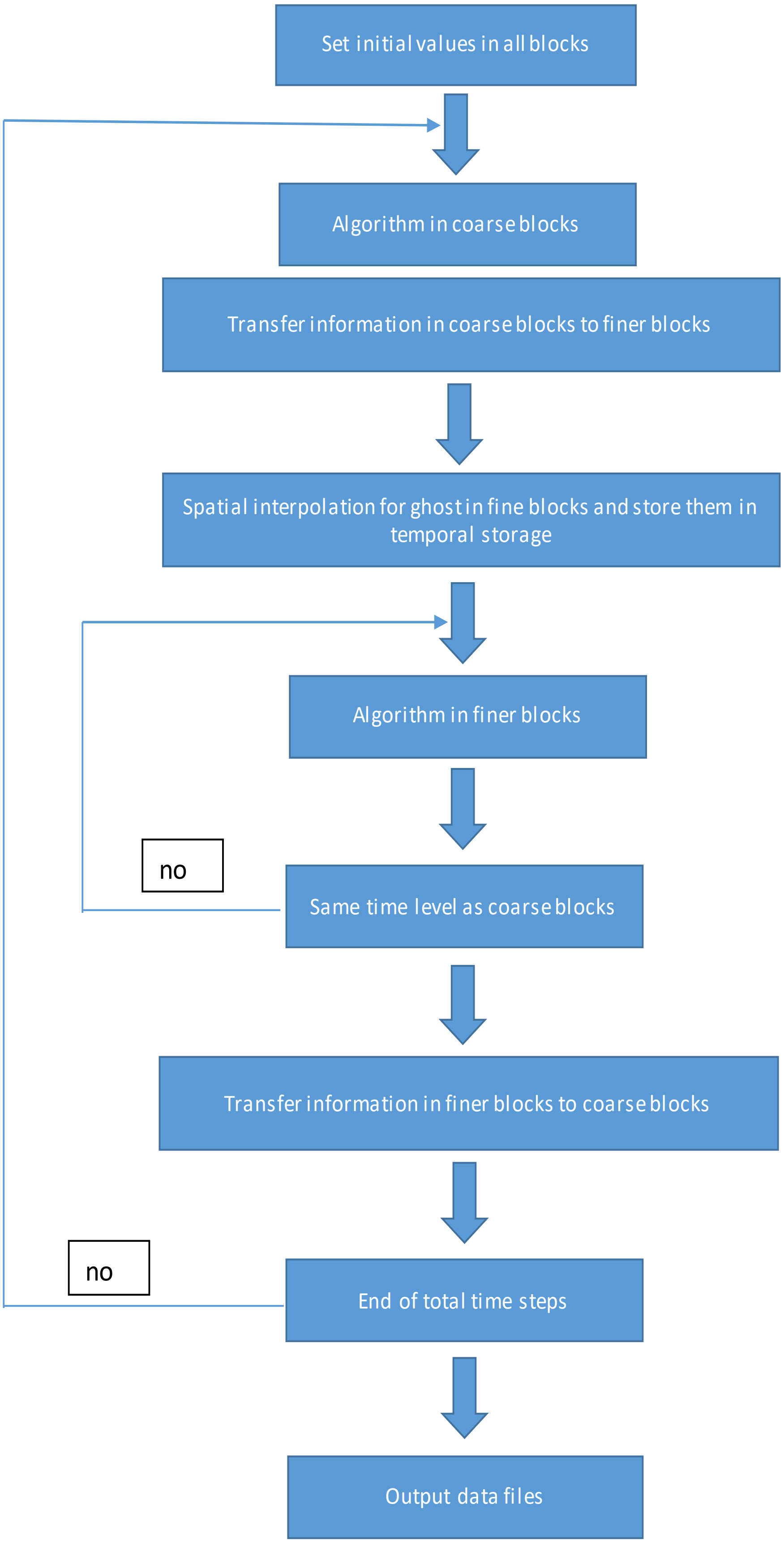

Figure 9 Flow chat of the computational procedure using multi-block approach

3.2.3 Boundary Conditions

For the bottom boundary, we implement uniform streamwise velocity for the jet orifice exit and the no-slip boundary condition for the bottom wall.

For the jet orifice:

$$f_5 = f_6 + W_0 * \rho_0/3 \tag{46}$$

$$f_{11} = f_{14} + W_0 * \frac{\rho_0}{6} - \frac{f_1 - f_2 + f_7 - f_{10} + f_9 - f_8}{2} \tag{47}$$

$$f_{12} = f_{13} + W_0 * \frac{\rho_0}{6} + \frac{f_1 - f_2 + f_7 - f_{10} + f_9 - f_8}{2} \tag{48}$$

$$f_{15} = f_{18} + W_0 * \frac{\rho_0}{6} - \frac{f_3 - f_4 + f_7 - f_{10} + f_8 - f_9}{2} \tag{49}$$

$$f_{16} = 7 + W_0 * \frac{\rho_0}{6} + \frac{f_3 - f_4 + f_7 - f_{10} + f_8 - f_9}{2} \tag{50}$$

For the no-slip bottom wall:

$$f_5 = f_6 + W_0 * \rho_0/3 \tag{51}$$

$$f_{11} = f_{14} - \frac{f_1 - f_2 + f_7 - f_{10} + f_9 - f_8}{2} \tag{52}$$

$$f_{12} = f_{13} + \frac{f_1 - f_2 + f_7 - f_{10} + f_9 - f_8}{2} \tag{53}$$

$$f_{15} = f_{18} - \frac{f_3 - f_4 + f_7 - f_{10} + f_8 - f_9}{2} \tag{54}$$

$$f_{16} = f_{17} + \frac{f_3 - f_4 + f_7 - f_{10} + f_8 - f_9}{2} \tag{55}$$

For the fully-developed top-outlet boundary [34]:

$$f_a(nz) = f_a(nz - 1) \tag{56}$$

At this top boundary, we consider the zero Gradient of velocity,

$$\frac{dU}{dn} = 0 \tag{57}$$

For side boundaries, periodic condition is imposed:

$$f_a(0) = f_a(n) \ or \ f_a(n) = f_a(0) \tag{58}$$

We follow the bounce back boundary condition by Zou/He [20] and modify the equilibrium part to reduce the information loss during the distribution function of collision on the boundary and bounce back processes. We focus on the core jet part and near jet orifice exit. The information loss is still acceptable around the no-slip wall and periodic boundaries.

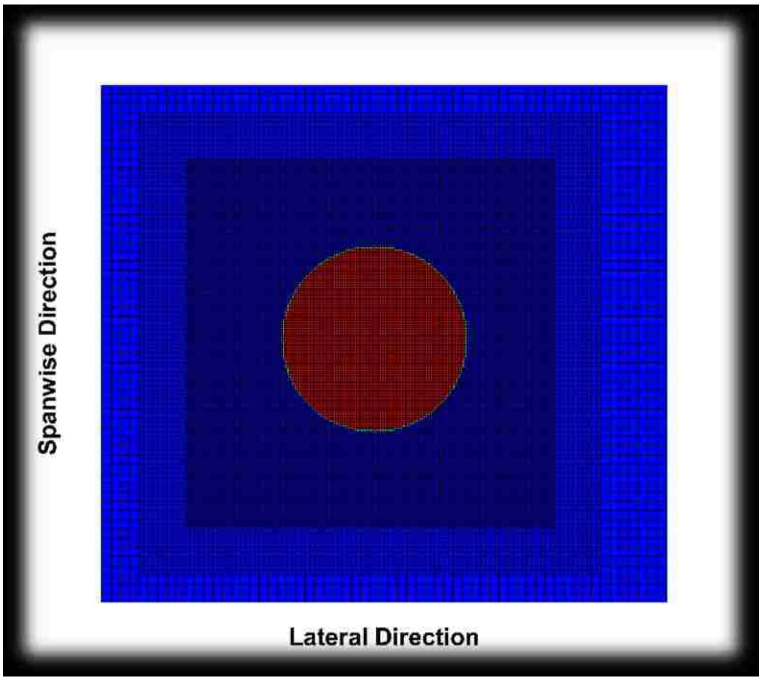

Figure 10 schematic of refined mesh around circular jet nozzle exit

For the curved boundary condition, the extrapolation approach is applied to specify the distribution functions on the boundary that does not belong to any grid blocks. As in Figure 11, we consider the velocity boundary conditions at the wall node, which is the neighboring one and belongs to the no-slip bottom wall. Extrapolation method is applied to handle the boundary condition along the orifice circular side.

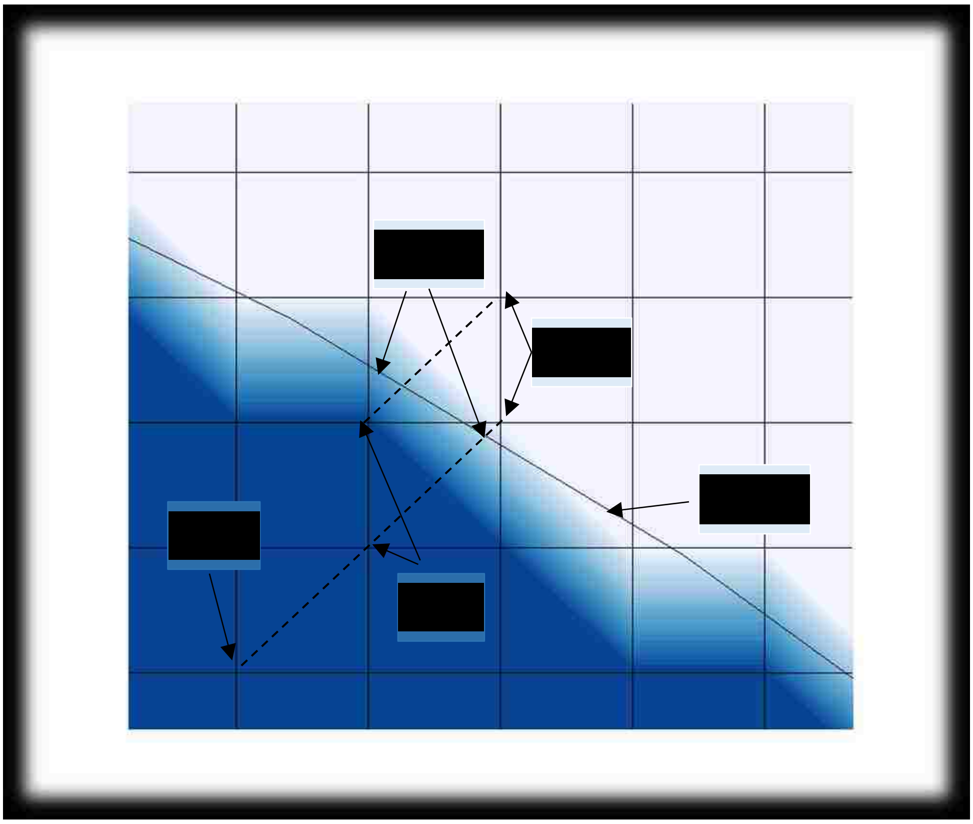

Figure 11 Lattice nodes of curved boundary

In these series of studies, the critical fraction of the intersected link in the fluid region: Δ_c is set to 0.65. As discussed in the Chapter 2, we compare the defined fractions Δ, (where $\Delta = \frac{|X_f - X_w|}{|X_s - X_w|}$) with Δ_c. If $\Delta > 0.65$, the boundary node is closer to the outside the solid region, and we use the macroscopic information of the neighboring nodes at solid region N_w and the fluid region N_f on the intersected link. If $\Delta < 0.65$, the boundary node is closer to the inside fluid region, the macroscopic information of neighboring nodes at the solid region N_w, the fluid region N_f and the successive fluid region nodes N_{ff} is then adopted.

3.2.4 Flow past cylinders

Here we present the simulations of flow past two cylinders as a benchmark of our SRT Lattice Boltzmann Method solver and we compare the Karman vortex street and vortex-shedding phenomenon for validation.

Flow past two tandem stationary cylinders in a uniform stream is a non-trivial nonlinear system, and previous studies demonstrates that the vortices separation between tow cylinders S/D has an important influence on the flow structure. In this section, such a flow configuration is investigated to validate our algorithm, the multi-grid non-uniform mesh model, and the curve boundary conditions with Re=100. The dimensionless computational domain is 25D (L)*10D (H) and the front cylinder center is located at 12.5D downstream of the inlet boundary and is on the centerline of the computational domain. The cylinder diameter is meshed with 20 lattices and the inlet free-stream velocity is V=0.1. The computed Strouhal number is presented in Figure 12. With the separation distance between two cylinders increases from 3D to 8D, Strouhal number increases. Similar trend has been reported by G.V. Papaioannou, et al [35]. When S/D increases from 3 to 3.5, Strouhal number increases gradually, and it is significantly lower value than that from single circular cylinder case ($St_s = 0.167$, as shown in the grey dash line). A sudden jump is observed when S/D increases from 3.5 to 4. The mechanism of the jump is that once S/D increases beyond a critical value the vortex suppression region is translating to the co-shedding regime as the following contours shown.

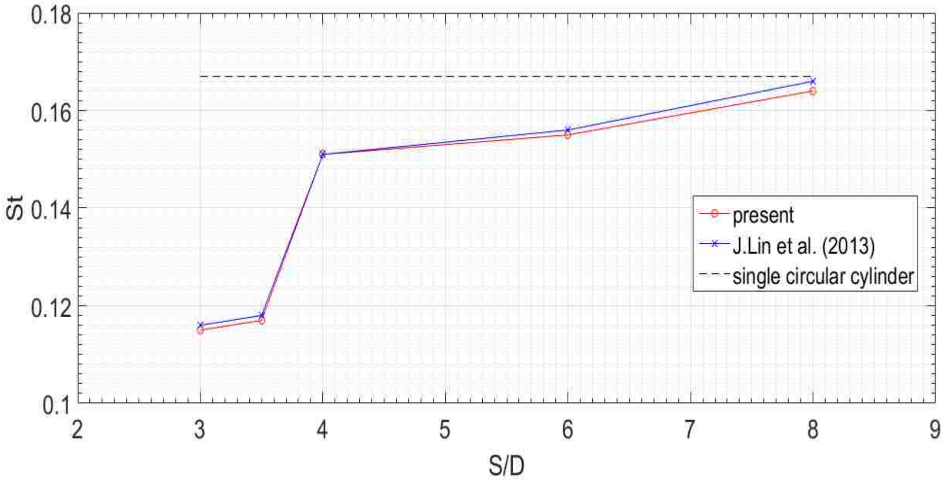

Figure 12 Strouhal number versus scaled distance between two circular cylinders at Re=100

Figure 13 and Figure 14 show the results of flow patterns for the cases of S/D=3.5 and 4 obtained by LBM simulations, and the comparison to the work done by J. Lin et al [36]. The left panels indicate the instantaneous vorticity contours for S/D=3.5 cases, comparing to the results of reference J. Lin et al. [36]. With the free shear layers from the front cylinder reattach to the upstream side of the rear cylinder, the presence of the rear cylinder suppresses the vortex shedding from the front one and vortices are only shed behind the rear cylinder.

The right panels of each figure shows the cases of S/D=4.The vortices are shed from both cylinders, as shown in the contours, which leads to a sudden increase in the Strouhal number. As S/D is increasing further, the interaction from the two cylinders decreases and St approaches the value of the shedding frequency of vortices from the single circular cylinder. Our result has a good agreement with results reported by J. Lin et al [36].

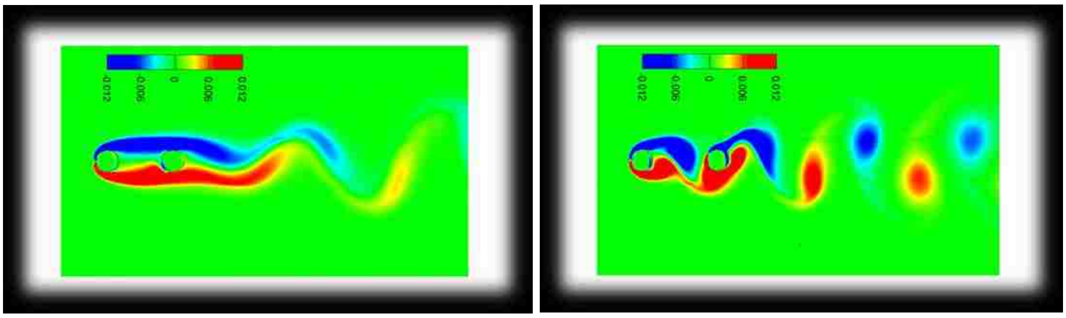

(a) present LBM simulation S/D=3.5 (b) present LBM simulation S/D=4

Figure 13 Instantaneous vorticity contours for the flow past two stationary cylinders in tandem at Re=100 of LBM simulation results: Left is S/D=3.5 case; right is S/D=4.0 case

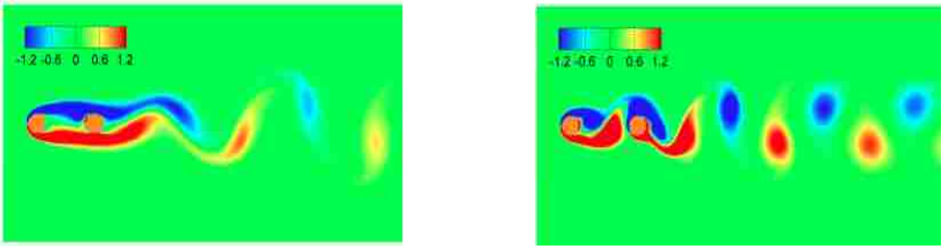

(a) J. Lin et al. [36] S/D=3.5 (b) J. Lin et al. [36] S/D=4

Figure 14 Instantaneous vorticity contours for the flow past two stationary cylinders in tandem at Re=100 of reference in Lin 2012: Left is S/D=3.5 case; right is S/D=4.0 case

3.2.5 Mesh Study

Although the LES method is a powerful tool in numerical simulation of turbulent flows and has less requirement in mesh size comparing to DNS, We should note that the LES method is still a turbulence model with modified small-scale structures of sub-grid flow field. Thus, the mesh convergence check is necessary. Figure 15 depicts the scaled centerline streamwise velocity obtained using two different mesh density levels at Re=72000. The resolution of coarse mesh is 34.304 million; the resolution of finer mesh is 41.165 million, which is 1.6 times finer than the ones in the original refined setup. No significant difference in the mean centerline streamwise velocity is observed; the decay location and spread out rate is similar between two different mesh sizes. Although notable difference is found at the area that is close to the jet orifice, it is still considered as a good match because this area is outside the main interested region in our validations. Thus, the original mesh setup is sufficient to ensure spatial convergence in predicting the development of the flow fields.

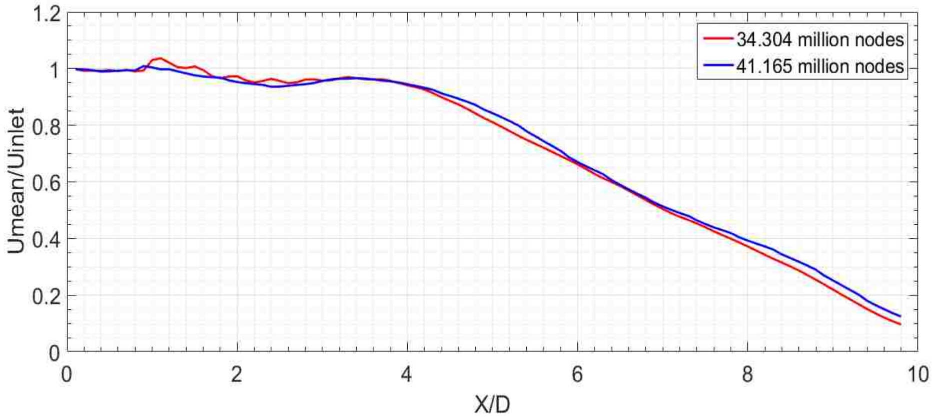

Figure 15 The scaled mean centerline streamwise velocity vs the normalized length obtained by two different mesh density at Re=72000

3.2.6 Statistical Quantities: Mean Velocity

One of the most important phenomena in this study is the core jet length and velocity decay account of the jet breakup at the downstream region. The mean centerline streamwise velocity is the most important statistical representation of the core jet length and velocity decay phenomenon. Since the fluid in the tank is stationary initially, we should not consider the flow field until it is influenced by the impulsive start. For the following centerline streamwise mean velocity calculations, we collect the data with the time interval, from 2.0s to 10.0s. Velocity profiles are presented in non-dimensional units by scaling the distances to the jet orifice diameter and the velocities to the actual uniform inlet velocity. The normalized velocity is indicated as U^* and is defined as

$$U^* = U/U_0.$$

Figure 16 displays the mean centerline streamwise velocity distributions for all cases. The length D denotes the jet orifice diameter. This simulation domain has length of 20D in streamwise direction (z-axis). We present the profiles in 10D, because we set fully developed outflow boundary condition as the outlet. Such outlet simplifies the later part of the computational domain, in an unrealistic way, and hence the effected region is less representative.

At lower Reynolds numbers, all the regions, up to approximately 6 diameters, shows an almost constant speed and no velocity decay. For all cases, in the region very close to the jet orifice ($Z < 0.5D$), small amplitude oscillations are noticed. This noise is more likely to be introduced by the boundary layer of the jet orifice.

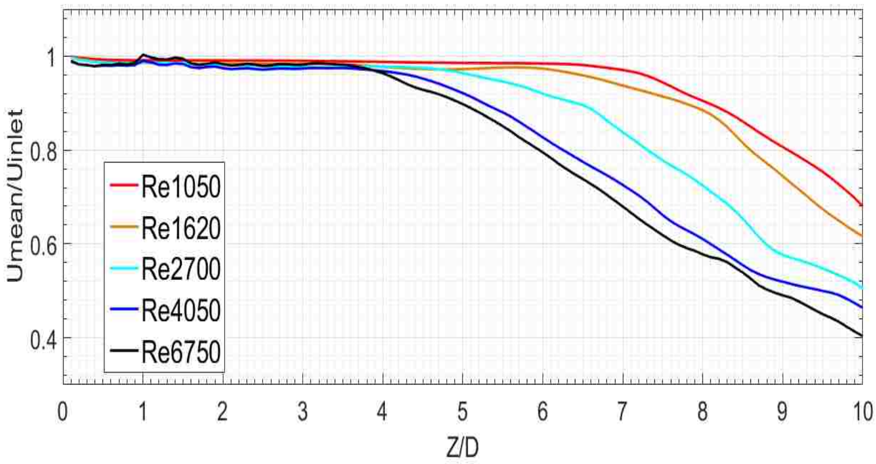

Figure 16 Scaled mean centerline streamwise velocity of all different Reynolds number cases

The amplitude of the fluctuation depends on the Reynolds number. For the lowest Reynolds number case, Re=1050, the mean centerline streamwise velocity remains nearly constant until the start of the velocity decay at 6.5D, which is the location of the jet breakup. The jet decays linearly in the streamwise direction beyond $Z/D \approx 6.5$. For the intermediate Reynolds number flows ($2700 \leq Re \leq 4050$), the mean streamwise velocity decay happens closer to the jet orifice, which means the core jet length is shorter. The mixing regions increase closer to the orifice at higher Reynolds number flow, and the jet spread out to ambient become more rapidly. Lastly, for the highest Reynolds number case (Re=6750), the decay starts at $Z/D \approx 4$.

In Figure 17, Figure 18 and Figure 19, we compare the centerline streamwise mean velocity with the reference case reported by Todde, V. et al [24] for Re=1050, Re=2700 and Re=4050. For the lowest Reynolds number flow, Re=1050, the Lattice Boltzmann simulation result matches well with the reference, and the decay location begins at $Z/D \approx 6.5$. We observed the similar trend for the velocity decay, the jet breakup and spread rate out to the ambient.

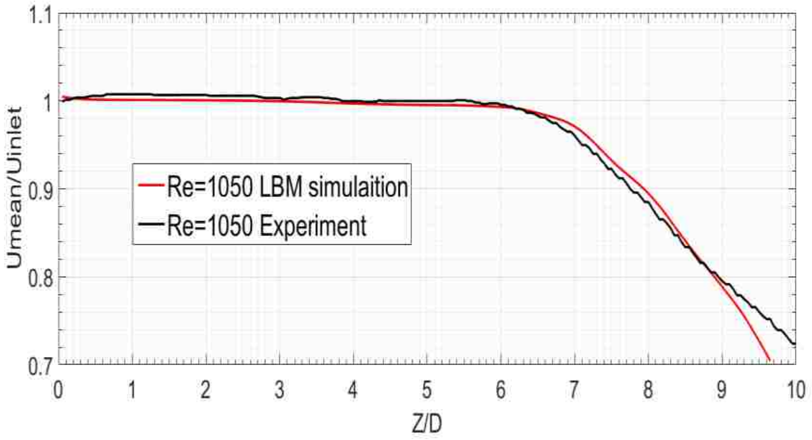

Figure 17 Comparison of scaled mean centerline streamwise velocity at Re=1050 between LBM simulation and experimental reference *[24]*

For higher Reynolds number cases, Re=2700 and Re=4050, although the *plateau* area is not observed clearly in Lattice Boltzmann simulation results, the decay begins location compares well with the reference at $Z/D \approx 4.75$ for Re=2700 and $Z/D \approx 4$ for Re=4050. Moreover, in the jet decay areas, the jet spreads out to the ambient at a similar rate comparing to that reported by the reference experiments.

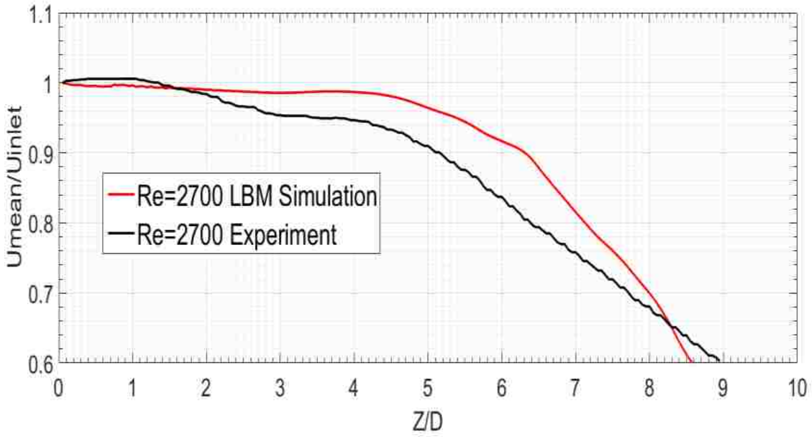

Figure 18 Comparison of scaled mean centerline streamwise velocity at Re=2700 between LBM simulation and experimental reference *[24]*

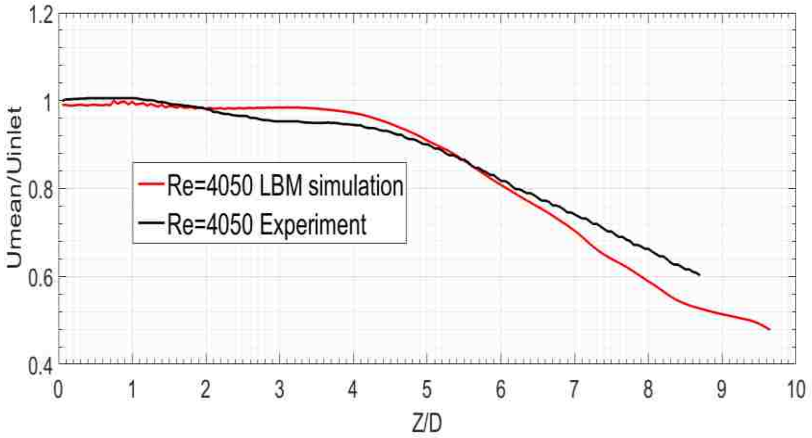

Figure 19 Comparison of scaled mean centerline streamwise velocity at Re=4050 between LBM simulation and experimental reference *[24]*

Unlike the reference experiments reported by Todde, V. et al [24], there's no notable *plateau* area that the velocity drops by 5% and sharp descent located around $Z/D \approx 2$. In all cases, U^* remains constant before $Z/D \approx 4$. The centerline velocity decays with the similar slope for all flow rates considered in this study. Detailed information about the profile of the centerline velocity decay position and decay region slopes are listed in Table 2 and plotted in Figure 20.

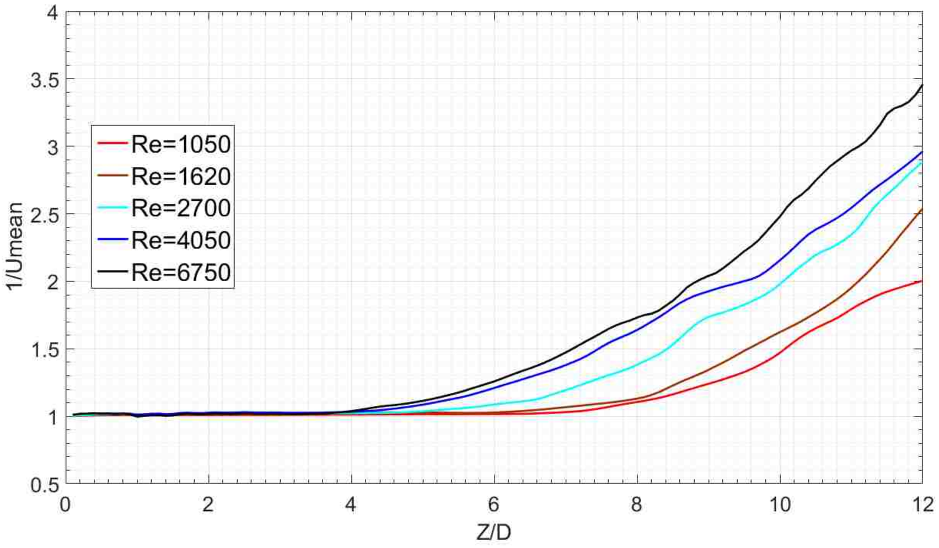

Figure 20 Inverse of scaled mean centerline streamwise velocity of all Reynolds number cases

Table 2 Inverse of scaled centerline streamwise velocity decay starts location and slope as a function of the Reynolds number

Re	1050	1620	2700	4050	6750
Decay region from	6.5D	6D	4.75D	4D	3.8D
Decay slope LBM	0.2302	0.2445	0.2273	0.2129	0.2056
Decay slope experiment	0.2418	0.2471	0.2147	0.2156	0.2011

We note that, for the decay regions, the slopes increase as Reynolds number increases for that is below 1620. At Re=1050, the slope is around 0.2302, and at Re=1620, the slope reaches the highest value, which is around 0.2445. Then the slope decreases with increasing Reynolds number from Re=2700 to Re=4050. On the other hand, for the lower Reynolds number cases, the rate of jet spreading out to ambient increases with Reynolds number increases. However, once the Reynolds number is greater than the critical value at 1620, the rate decreases with Reynolds number increases. The lowest slope, 0.2011, is observed at Re=6750. The slope value and variation tendency match well with the experimental results [24].

3.2.7 Statistical Quantities: Turbulence Intensity

Here, the turbulence intensity is defined as the root-mean square of velocity fluctuation scaled with the inlet uniform velocity.

$$TI_{scaled} = \sqrt{< \bar{U}^2 >/U_{inlet}} \tag{59}$$

Where, $\bar{U}$ represents the z-components of the fluctuating velocity.

The turbulence intensity profiles of different Reynolds number case are shown in Figure 21. As discussed earlier, we assume the flow field to be fully-developed, and the downstream part of the computational region is neglected due to the outlet boundary condition. Thus, we present profiles and flow images up to 15D away from the jet orifice along the streamwise direction (z-axis). The profiles do not start at $Z/D \approx 0$, because of the noise and *vena contracta* effect [24] around the jet orifice. The noise is damped out within 0.5 diameters from the orifice exit. Here, we plot the turbulence intensity profile from $Z/D \approx 0.2$ for comparison. Except the lowest Reynolds number case, Re=1050, sudden rises are observed from $Z/D \approx 1$ for higher Reynolds number cases. For Re=1050 flow, the raise of turbulence intensity begins from $Z/D \approx 2$.

For Re=1620, or 2700, after the initial rising, a clear peak, whose position shows a slight Reynolds dependence, always happens at the location of $Z/D \approx 5$. The turbulence intensity decreases slightly with 0.5D valley path and rises again to a global maximum value at the second peak. For Re=1620, the second peak is located at $Z/D \approx 8.7$; for Re=2700, the second peak is located at $Z/D \approx 7.5$. However, for the lowest Reynolds number case Re=1050 and higher Reynolds number case Re=4050, the first peak and valley path is not clear. This may be due to the coefficient of LES turbulence model against the Kolmogorov scales [38].

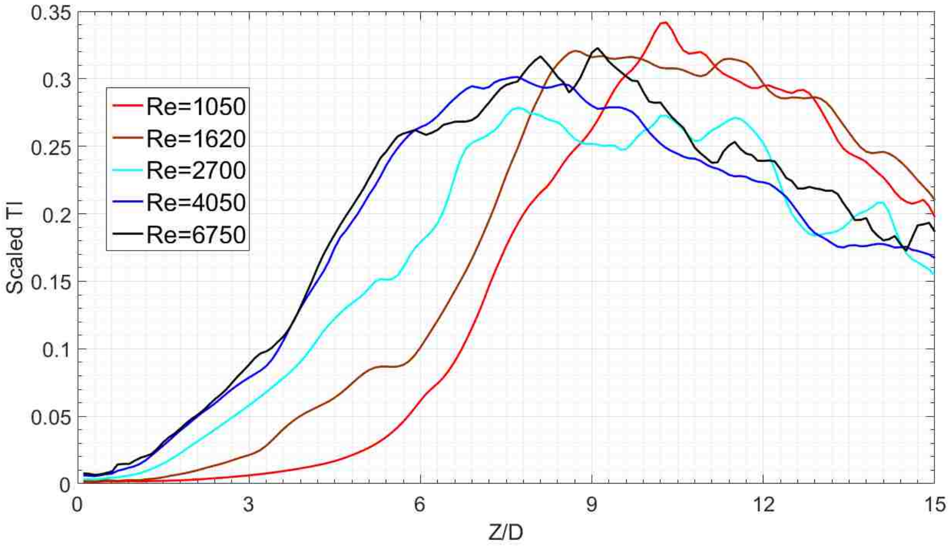

Figure 21 Scaled mean centerline streamwise turbulence intensity of all different Reynolds number cases

We use the same Smagorinsky coefficient for all the cases. At Re=1050, for this particular Smagorinsky coefficient, the Kolmogorov scale is not small enough comparing with the mesh length scale, and the turbulence solver is over modeled. At Re=4050 and Re=6750, although the Kolmogorov scale is small enough, the Smagorinsky coefficient we set is not enough to capture the accuracy of eddy viscosity. After the global peaks, turbulence intensity decreases rapidly to ground in all cases with large fluctuation. This could happen since the simulation results after $x/D \approx 10$ is no longer precise. In addition, around the global peaks, the vortex breaks up and the jet structure becomes irregular, thus the fluctuation of turbulence intensity in the downstream region become remarkable. The detailed location and the peak are listed in Table 3 for different values of Reynolds number.

Table 3 Turbulence plots' features as a function of the jet Reynolds number

Jet Re	First peak location [X/D]	First peak level [%]	Second peak location[X/D]	Second peak level [%]
1050	-	-	10.2	34.5
1620	5.2	8.2	8.7	32.1
2700	5.2	15.2	7.6	27.5
4050	-	-	7.2	30
6750	5.4	26.1	-	-

Although our Lattice Boltzmann simulation results for turbulence intensity do not match well with the reference for the lowest and highest Reynolds number cases, our results for Re=1620 and Re=2700 match well with experimental results. Further investigations can focus on different sub grid scale, and the modification of Smagorinsky coefficient to capture higher accuracy of eddy viscosity.

3.2.8 Spectra Analysis

The features of the statistical quantities along the centerline can be explained by relating the jet mixing structure to the signal time evolution. Figure 22 and Figure 23 display the time evolution of the streamwise velocity at various locations along the centerline for Re=2700 and Re=1620. In order to demonstrate the fluctuation and amplitude, here two-seconds of the time spans is shown. The X-axis represents the recorded time interval and Y-axis represents the scaled instantaneous streamwise velocity.

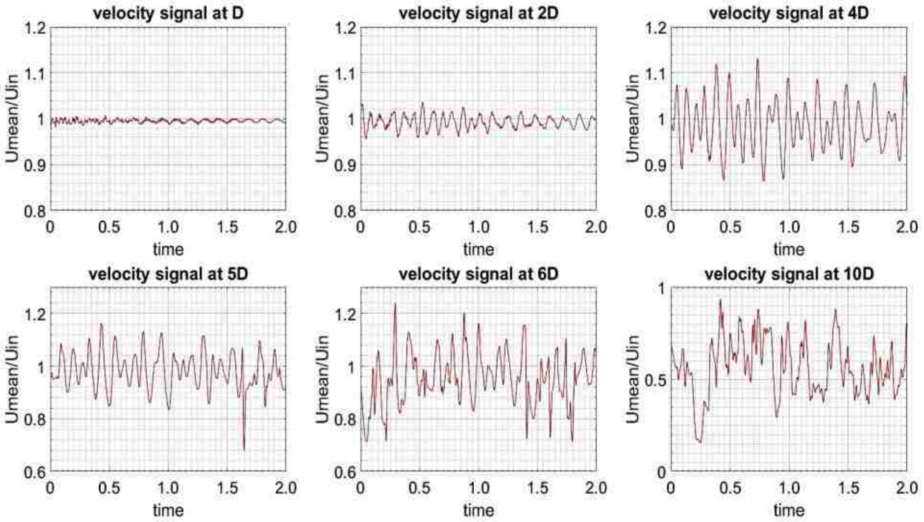

Figure 22 2 seconds spans of velocity signal at X/D = 1, 2, 4, 5, 6 and 10 for Re=2700

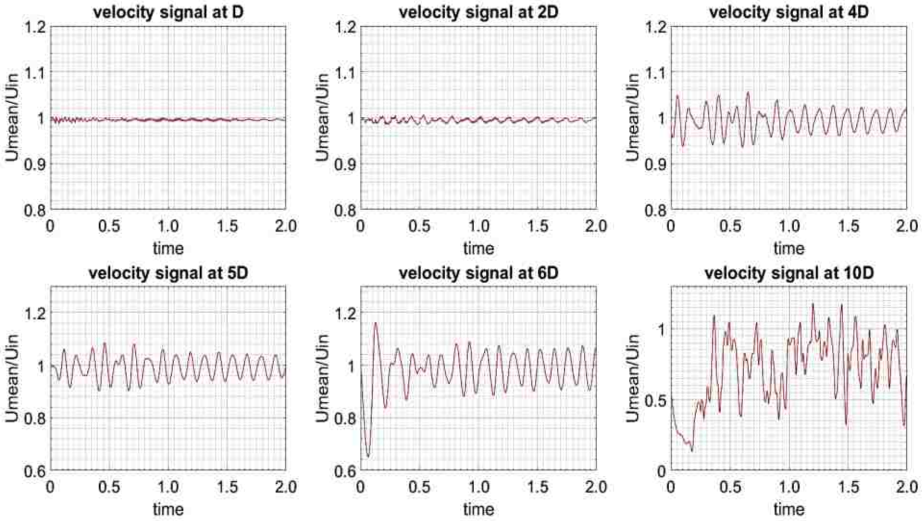

Figure 23 2 seconds spans of velocity signal at X/D = 1, 2, 4, 5, 6 and 10 for Re=1620

The amplitude of signal increases from Z/D = 1 along with the increased turbulence intensity, as illustrated in Figure 22 and Figure 23. The signal profile shows that the flow is very orderly and periodic in the region before Z/D = 5. It becomes irregular and disorderly with a decreasing amplitude as the jet is decaying less than 90% and the vortex breakdown occurs beyond the critical position of Z/D = 6.

For lower Reynolds number flow, Re=1620, as it is shown in Figure 23, the increasing turbulence intensity starts further away from the orifice, at around Z/D = 3. Among the velocity signal at the same position for different Reynolds number, the frequency of fluctuation as well as the signal strength increases with increasing Reynolds number. For Re=162, the signal shows orderly stable and periodic behavior at $Z/D \geq 6$, and the critical position is even further away for Re=2700.

Figure 24 and Figure 25 demonstrate the scaled power spectra obtained by applying the Fast Fourier Transform (FFT) to the time traces corresponding to the plots shown in Figure 22 and Figure 23 from Z/D = 1 to Z/D = 5. In order to compare a temporal and spatial characteristics properties, each spectrum is scaled by the root-mean-square fluctuation of the corresponding signal. In addition, for clarity of representation, each spectrum is shifted one decade downward with respect to the previous one, as shown in Figure 24.

In Figure 24, a clear peak can be observed near Z/D = 1 location at low frequency regions around 3.5Hz. As the distance from the jet orifice increases, the peak becomes weaker and it disappears at Z/D = 10.

Finally, some sharp high-frequency, low energy peaks are present at positions upstream of Z/D = 4, but these ovservations can be attributed to the noise in the signal. The high frequency, low energy peaks are only detectable at locations which are close to the jet orifice.

The data supports typical flow topology in these systems described earlier. The spectral peaks indicate the presence of coherent structures of jet evolution. The frequency corresponding to the peak value of energy displays an evident reduction when the fluid flow entering downstream region. Meanwhile, the spectrum peak expands to the ambient air.

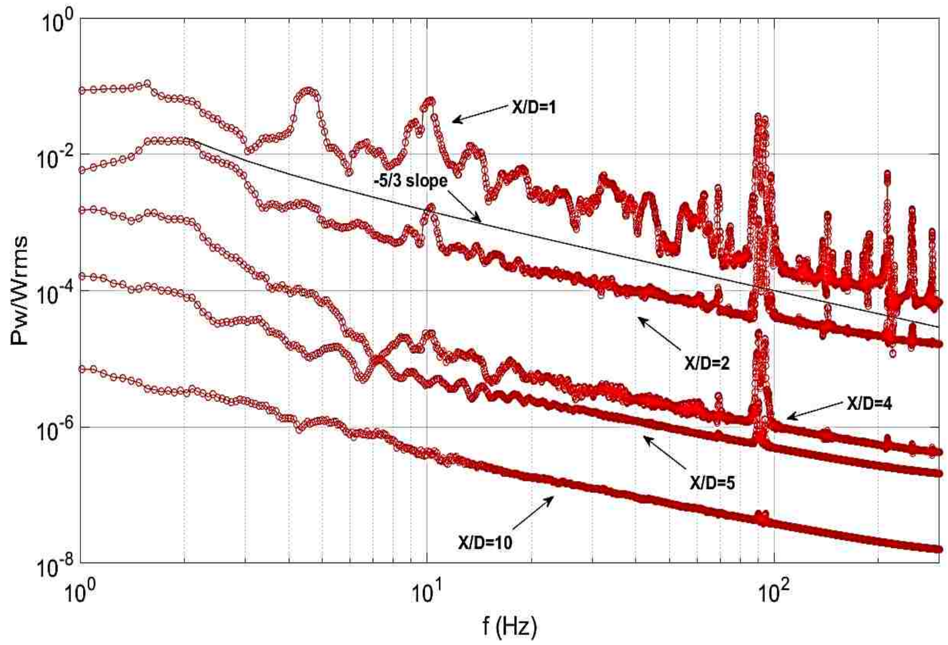

Figure 24 Normalized power spectra of velocity signals for Re = 2700

Similar flow characteristics are observed at all Re considered. Figure 25 shows the scaled spectrum value corresponding to the frequency for Re=4050.

The spectrum peak appears at the location of Z/D = 1 at 5Hz, and the peak value decreases as Reynolds number increases. As the distance from the orifice increases, the spectrum peak disappears beyond Z/D = 4, closer to the jet orifice compared to Re=2700. At this location, the vortex breakdown occurs, and energy spectra dissipates in the frequency domain. For Re = 4050, the spectrum becomes even flatter at Z/D =4, because the vortex breakdown occurs at a location closer to the jet orifice.

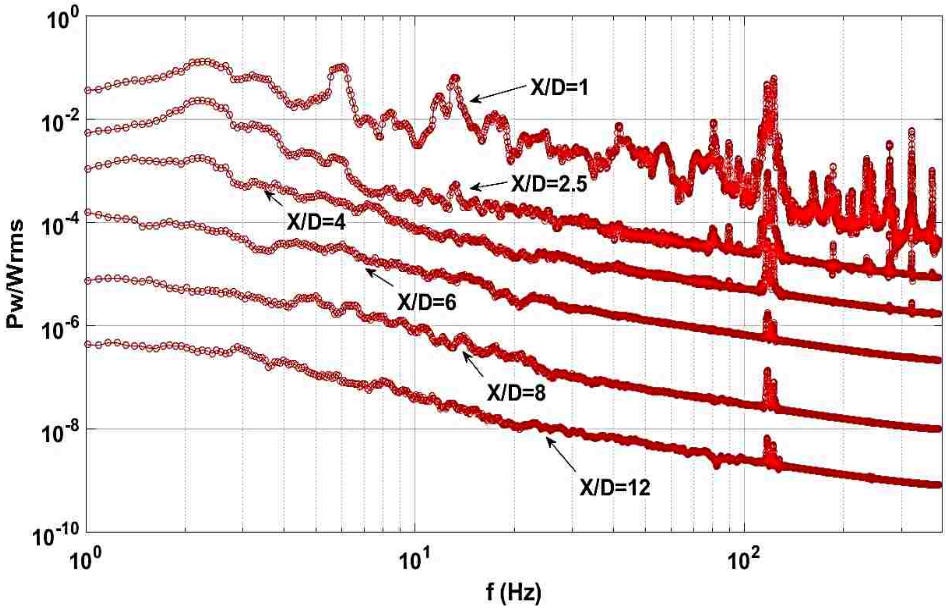

Figure 25 Normalized power spectra of velocity signals for Re = 4050

The sharp high frequency spectrum peaks are also observed for high Reynolds number flow. Unlike lower Reynolds number flow, for Re = 4050, the peak at high frequency spectrum is observed at a downstream region about Z/D = 12, which might be the result of noise.

Also, at Z/D = 1, for low Reynolds number flow, the peak appears at a lower frequency compare to higher Reynolds number flows. Such a behavior can be explained by the trace of a vortex pairing along the jet evolution and the increasing vortex pairing interaction.

3.2.9 Flow Images

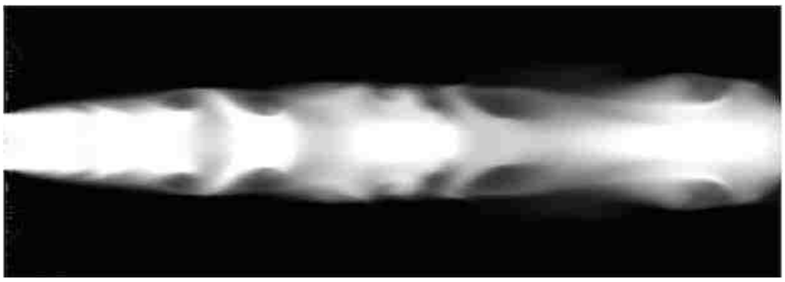

t=2.0s

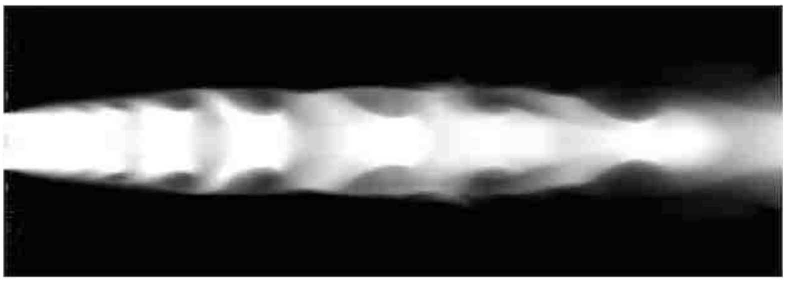

t=2.5s

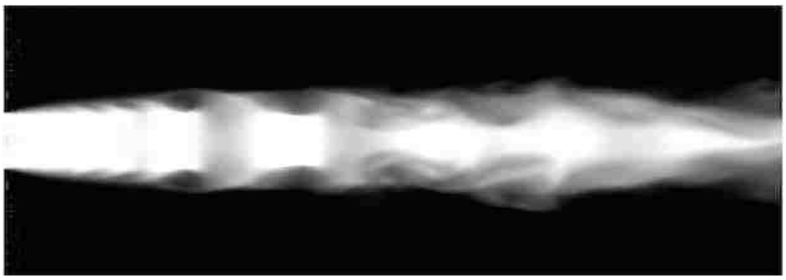

t=3.378s

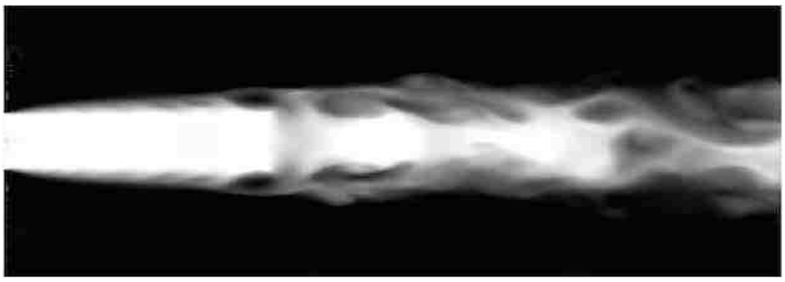

t=4.563s

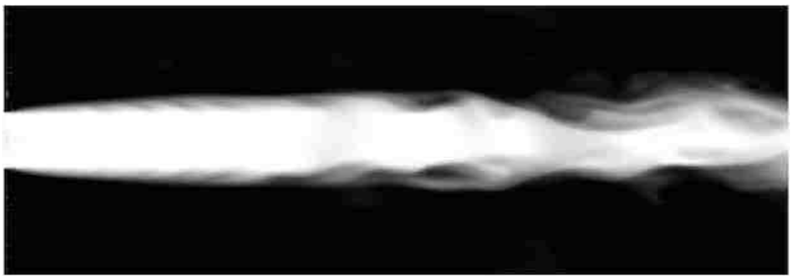

t=6.25s

Figure 26 Flow images, case Re-1050, at 2.0s, 2.5s, 3.378s, 4.563s and 6.25s from top to bottom

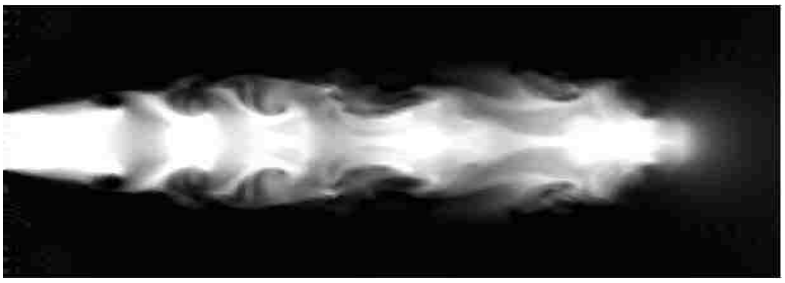

t=1.7s

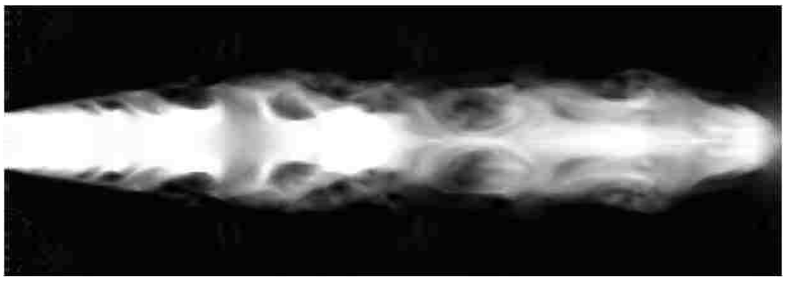

t=1.79s

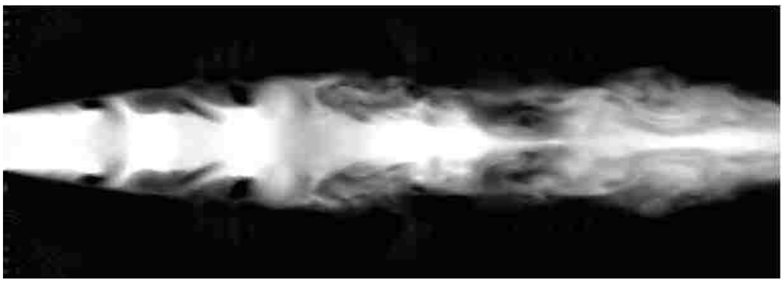

t=1.85s

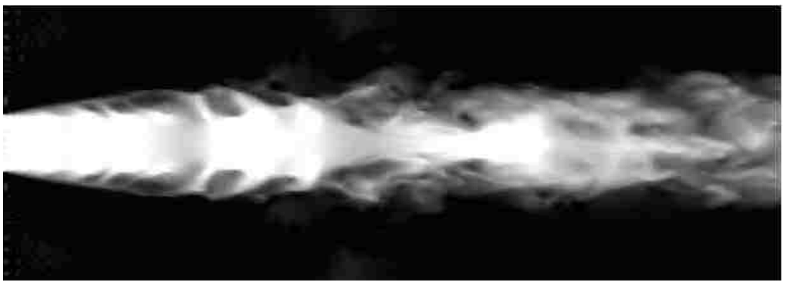

t=2.05s

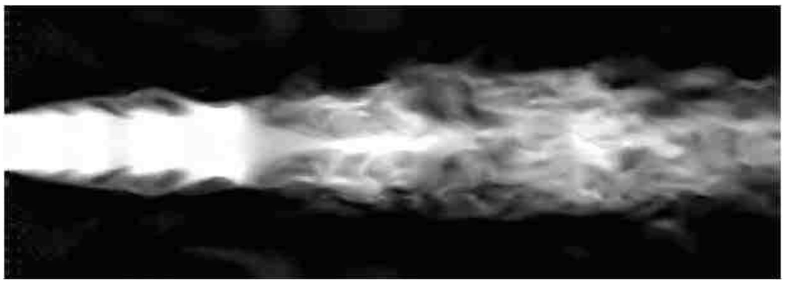

t=2.57s

Figure 27 Flow images, case Re=2700, at 1.7s, 1.79s, 1.85s, 2.05s and 2.57s from top to bottom

To characterize flow dynamics and the jet structure topology, the images of the instantaneous velocity contours are acquired. Figure 26 displays five images at various instant for Re=1050. Five distinct topologies are presented in the field, which are showing the generation, in a symmetrical fashion, of bulks of vortices regularly shed from the main jet core. Vortex generation occurs in a periodic fashion continually. Prior to 2.5s flow time, the vortex generation are nearly symmetric and the core of jet is intact holds the main fluid bulks well. After 4.563s, the jet breakup is observed at downstream locations. For the higher Reynolds number case, the paring vortex is observed at the periphery of the core. However, the pairing for the lower Reynolds number jet is not as clear as that for higher Reynolds number flow. This is because at low fluid speeds the interaction of vortices with the core flow is relatively weak and it is difficult to be differentiated. The jet breakup phenomenon is observed earlier flow times and it occurs closer at locations close to the jet orifice. In Figure 27, five different instantaneous fluid bulks topology of the jet for Re=2700 are presented. Generated vortices are nearly isolated. The interaction between neighboring vortices is stronger compared to vortices that are further away from each other. The mixing region is closer to the jet orifice, and the jet breakup disperse rapidly and the flow becomes fully turbulent in a wider region. Before 1.7s, the jet fluid bulks topology is almost symmetric, and the jet is continuous without breaking down until 1.8s.

When Reynolds number increases, the interaction among shed vortices becomes stronger and the flow structure is influenced profoundly by such interactions. The pairing vortices are observed more clearly. The core jet region becomes shorter and mixing is more effective.

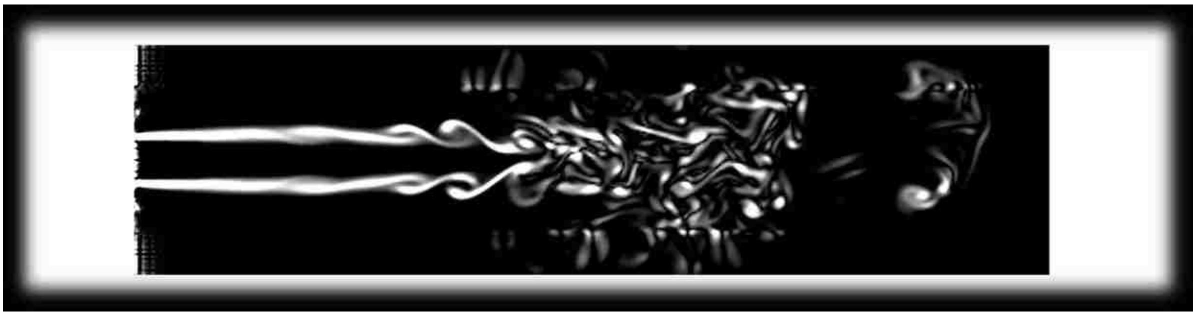

(a) Re1620 at t=10.3s

(b) Re2700 at t=7.6s

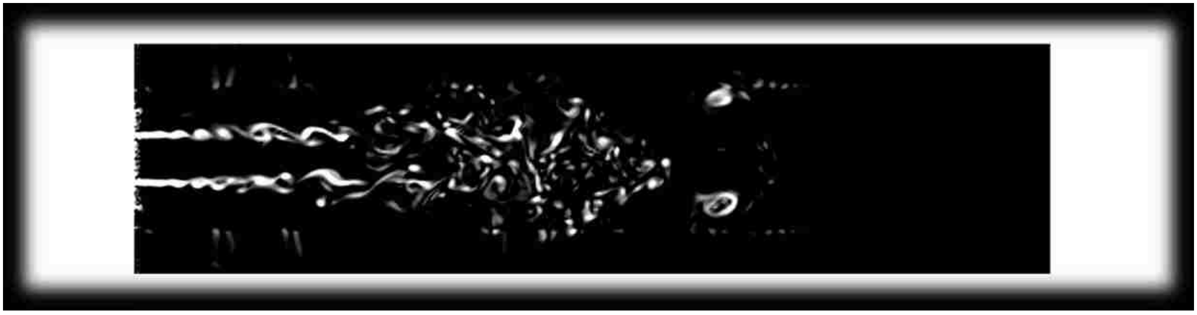

(c) Re4050 at t=3.5s

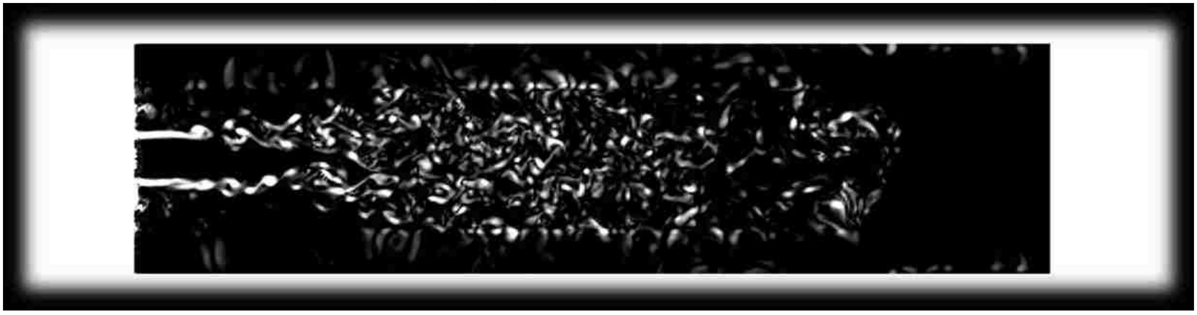

(d) Re6750 at t=2.8s

Figure 28 Instantaneous vorticity images for different Reynolds number cases

The instantaneous images of vorticity are shown in Figure 28 and are compared for flows at different Reynolds number. Generation of vortices at the periphery of the core region is clearly demonstrated.

As Reynolds number increases, the region of vortex generation decreases, and similar with the core jet length as we discussed earlier section. For the lower

Reynolds number flows, Re=1620 or Re=2700, in the region where vortex rollup, the vortex paring phenomenon is difficult to be observed, and the interaction among vortices is weak. On the other hand, for the higher Reynolds number flows, Re=4050 or Re=6750, the pairing vortex is presented in the region of vortex rollup. The vortices are generated separately are disattached from each.

In the vortex breakdown region, vortices generated by the primary Kelvin-Helmholtz instability make the mixing layer grow. For high Reynolds number flows, based on the vorticity thickness of the shear layer in the mixture region, vortex interactions cause jet flow transition to fully turbulent flow regimes. As Reynolds number increases, the flow field becomes more turbulent away from the jet orifice. The vortices in the downstream region breakdown into smaller eddies. This flow phenomenon is referred as the secondary Kelvin-Helmholtz instability.

3.2.10 Conclusion

All the simulations are performed using the Lattice Boltzmann Method solver. Compared with traditional macroscopic numerical method, LBM is more efficient, because it offers straightforward mesh refinement, and parallel computing algorithm implementation. The good agreement is found between predictions and experimental measurements reported in the literature.

The results display several flow regimes for the range of different Reynolds number from 1050 to 6750. For jet flow at Reynolds number below 1620, the jet flow is nearly laminar near the orifice. With weak dissipation of energy, the jet decay starts far from the jet orifice, and the jet spreads out to ambient at a low rate after the core jet structure breaks up.

For high Reynolds number, Re>1620 flows, a stronger dissipation, concomitant to a turbulent regime within the shear layer, is observed. The phenomenon of velocity decay can be captured at a different location that closer to the jet orifice exit, and the fluid flow spread to ambient with a relatively high rate than the lower Reynolds number jet flows.

Flow images are presented to obtain a qualitative description of the flow structures. Such flow images confirmed and clarified the results obtained from the quantitative measurements [24].

This work indicates that the behavior of low-Reynolds number jet flows is quite different than its counterpart at higher Reynolds number flows. The further research devoted to the understanding of such behavior appears to be innovative and several challenging tasks are still need to be completed.

3.3 Single-phase jet from 6-lobed orifice

3.3.1 Simulation setup

We simulate jet flows emanating from the six-lobed rectangular orifice for various values of Reynolds number. The flow field in the region close to the orifice is compared to that for the circular jet with the same initial conditions. The mean centerline streamwise velocity, turbulence intensity and spectra analysis are calculated. In the circular jet, flow motion is dominated by large primary Kelvin-Helmholtz structures, while in the six-lobed rectangular jet, the K-H vortices are very thin compared to the large secondary vortices generated by the high shear at the lobed nozzle lip. The inspection of mean velocity profiles and streamwise evolutions of the spreading rates in the major (MP) and the minor (mP-L) planes of the lobed jet confirm that the axis-switching phenomenon is absent. The streamwise structures that develop in the orifice troughs render the volumetric flow rate significantly higher than that of the circular jet [32].

This section reports results of Lattice Boltzmann Method simulations to investigate the near-field flow characteristics of air/air turbulent jets issuing respectively from notched-rectangular and circular orifice plates with identical opening areas and equivalent diameters. Consistent with previous work on circular jets, the present study finds that the six-lobed jet has a higher rate of mixing than does the circular counterpart [39]. In particular, this jet in the very near field transfers its momentum to the surroundings at a greater rate, evidenced by a notably shorter unmixed core and faster turbulence intensity growth. The higher rates of overall decay and spread of the six-lobed jet are obtained by the post-processing using MATLAB codes.

The schematic geometry of the computational domain is shown in Figure 29 and dimensions are listed in Table 4. The x, y and z axes denotes the lateral, spanwise and streamwise directions, respectively. The jet orifice locates at the center of plane.

We impose a uniform velocity and density (pressure) profile at the orifice: $w_0 = 0.1$ and $\rho_0 = 1.0$. The molecular viscosity ϑ_0 is set so that the desired Reynolds number is achieved with $D_e = 18$. Initially, the fluid is set at a quiescent state with $\rho = \rho_0 = 1.0$ and $\mathrm{u} = \mathrm{v} = \mathrm{w} = 0$ everywhere except at the jet orifice where $w = w_0\hat{z}$.

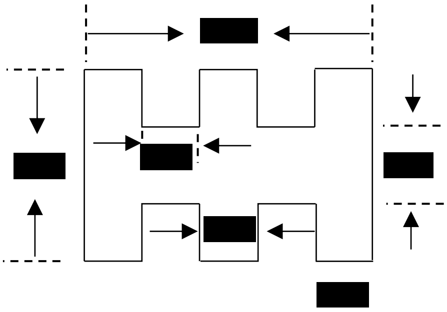

Figure 29 Schematic representation of 6-lobed nozzle exit

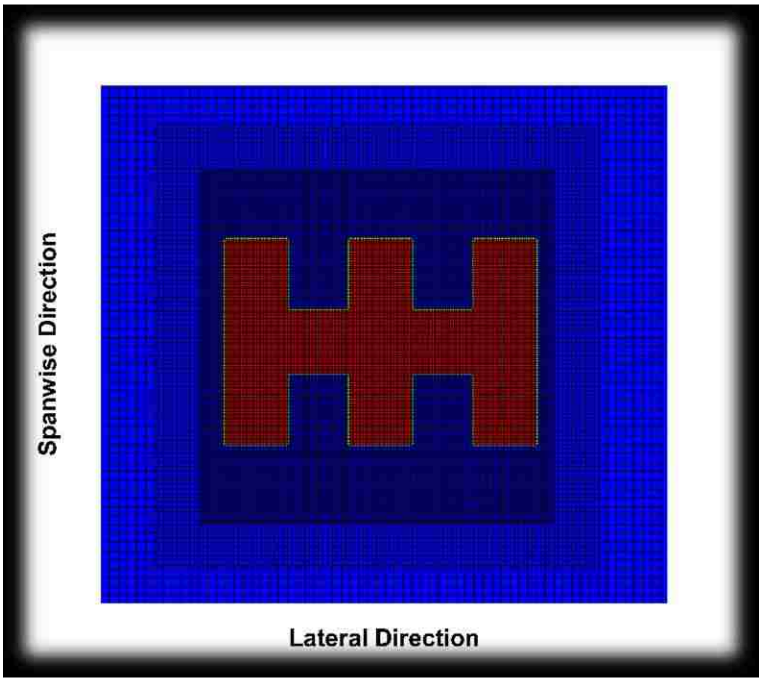

Figure 30 six-lobed jet orifice geometry and refined mesh around the exit

Periodic boundary conditions are imposed at the side boundaries in both x and y directions. It is demonstrated the assumption of periodicity does not affect the jet structure or statistics in the domain of interest. The no-slip boundary condition is applied at the wall ,and fully-developed flow boundary conditions are applied at the outlet:

$$f_\alpha(N_z, t_n) = f_\alpha(N_z - 1, t_n)$$

Table 4 Computational grid size

	w	h	a	b	c	$\mathbf{D_e}$	W*H*L
Experiment (mm)	15	10	3	3	3	12	60 *60 *240
LBM (dimensionless)	30	20	6	6	6	18	100 *100 *400

Table 5 Uniform exit velocity and actual exit Reynolds Number of 6-lobed jet

Test Case	Uniform exit velocity (m/s)	Exit Reynolds Number, Re_D
1	3.4	2700
2	8.4	72000

This condition enforces vanishing spatial derivative along streamwise direction on all quantities of interest. The use of this unrealistic outflow condition renders the computed solution non-physical in a region immediately preceding the outflow boundary. This region which is influenced by the fully-developed flow conditions is called buffer zone. The sole purpose of this zone is to insulate the physically accurate computational zone from the fully-developed outflow conditions. It has been found form experience that the length of buffer zone should be a few integral length scales of the whole domain, which in the present case, the buffer zone accounts for the last third of the entire domain.

3.3.2 Statistical Quantiles: Mean Velocity

First, we present the flow field at the lowest Reynolds number, Re=2700, and compare the results with the case of jet issued from the circular orifice. Figure 31 shows the normalized instantaneous streamwise velocity contours at YZ-plane for Re=2700. The main jet structure is clearly observed at this Re. For the 6-lobed jet, the asymmetric core jet structure is seen in the flow image, and jet spreads out in the minor plane more rapidly compared to the spreads rate of the circular jet. The core jet length is around 0.9D, and the velocity decay starts around $Z/D \approx 0.9$, then the jet continues to spread out in the region $Z/D \approx 2.5 - 7$, and spreads continuously farther downstream. On the other hand, for circular jet, the core jet structure is nearly symmetric, and the core jet length is around much longer. Based on the above observations, the 6-lobed jet is deduced to spread and decay, overall, more rapidly than the circular jet.

The profile of the mean centerline streamwise velocity is shown in Figure 32. The core jet length of 6-lobed jet is shorter than that of the circular jet, which agrees with the contours depicted in Figure 31. For 6-lobed jet, the jet decay starts at $Z/D \approx 3.5$, correspondingly, the jet decay starts later at $X/D \approx 4.5$ for the circular jet. The unmixed region is much shorter for 6-lobed jet. After the jet decay, the core jet structure starts breakup and spreads out rapidly. For the 6-lobed jet, the rate of jet spreads out is much greater than that for the circular jet, and the air mixes with the ambient at a faster rate than that for the circular jet.

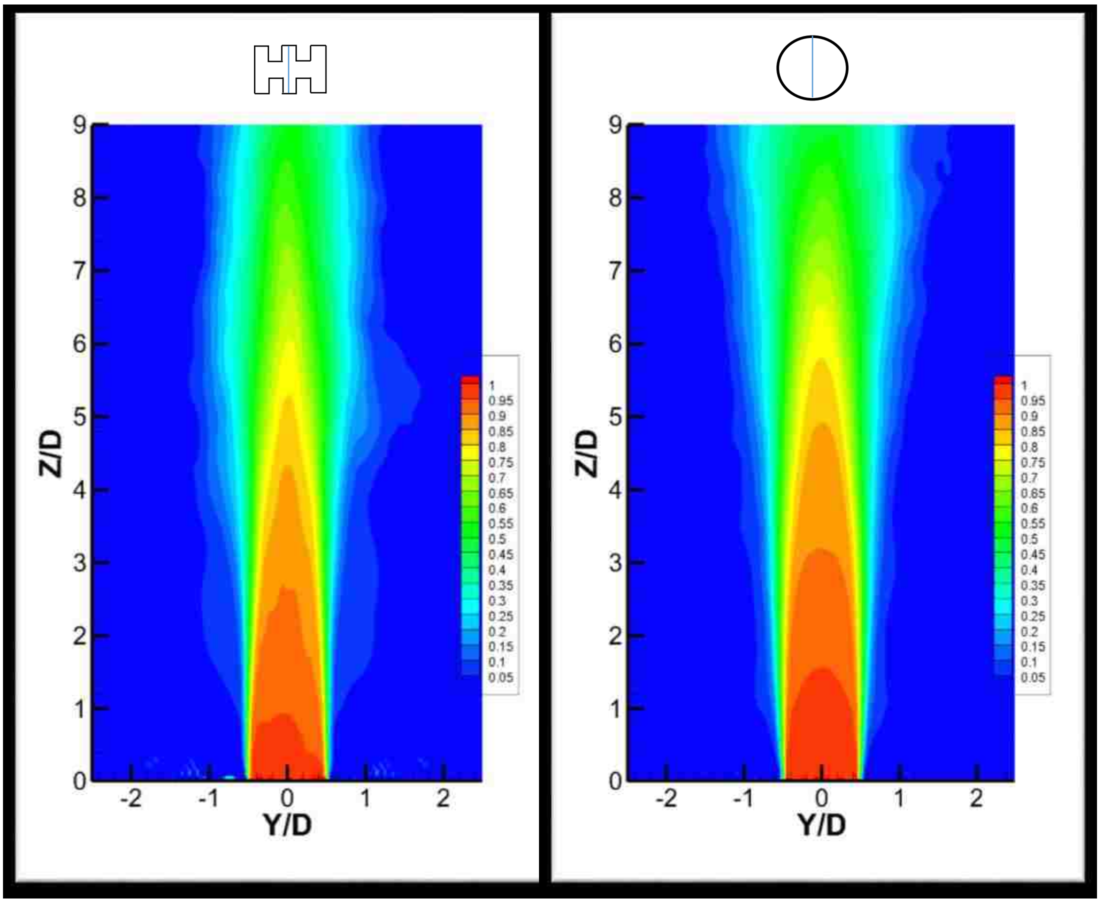

Figure 31 Normalized minor plane instantaneous streamwise velocity contours of 6-lobed jet (left) and circular jet (right) for Re=2700 at t=8s

Thus, for Re=2700, the 6-lobed jet mixes with the ambient with a greater rate, and the unmixed region is shorter than that in the circular jet. The decay in the centerline velocity of the notched jet is significantly faster than that of the circular jet in the near field.

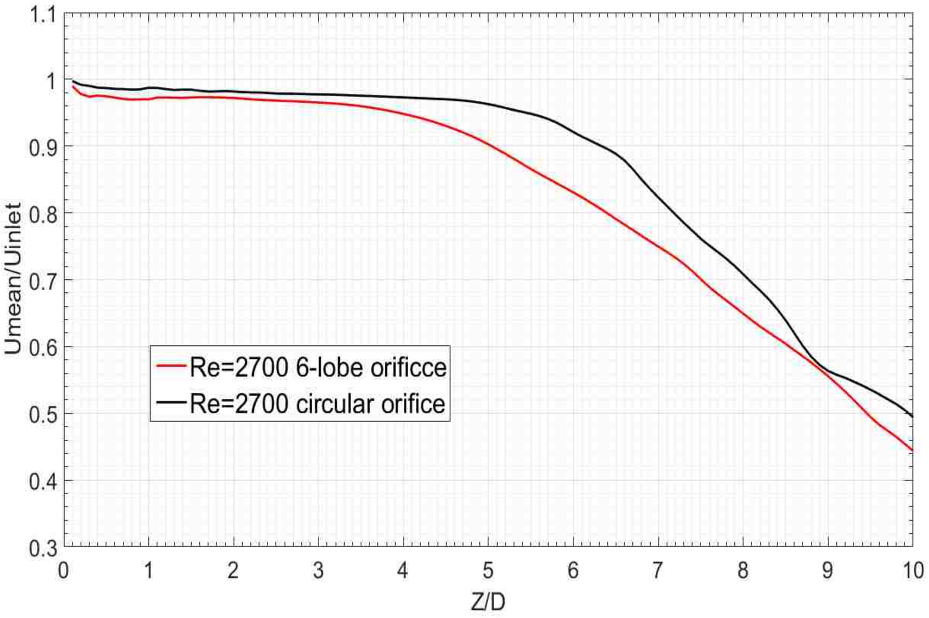

Figure 32 Comparison of 6-lobed orifice and circular orifice for normalized mean centerline streamwise velocity at Re=2700 case

For Re=72000 with Mach number Ma=0.3, Figure 33 shows the normalized mean streamwise velocity (W_{mean}/W_{inlet}) contours in the two center planes (major plane and minor plane) for jets emanating from the 6-lobed jet orifice. Compared with the lower Reynolds number jet, the core jet decay more rapidly for Re=72000. Near the jet orifice $X/D < 0.4$, the jet first contracts slightly, the core jet increases rapidly following the contraction. The lobed jet in the XZ plane spreads out rapidly from the jet orifice to $Z/D \approx 1$, then contracts slowly over the region of $Z/D \approx 2-7$, and spreads continuously farther downstream (not shown here for $Z/D > 9$). On the other hand, the jet in the YZ plane contracts immediately downstream at $Z/D \approx 0-0.7$ and then turns to spread out very rapidly for $Z/D < 1$, and farther the spreading rate becomes nearly constant for $Z/D \geq 1$. Concurrently, the jet core (red areas) contracts slightly in the YZ plane while diverging in the XZ plane in the region $Z/D < 1$.

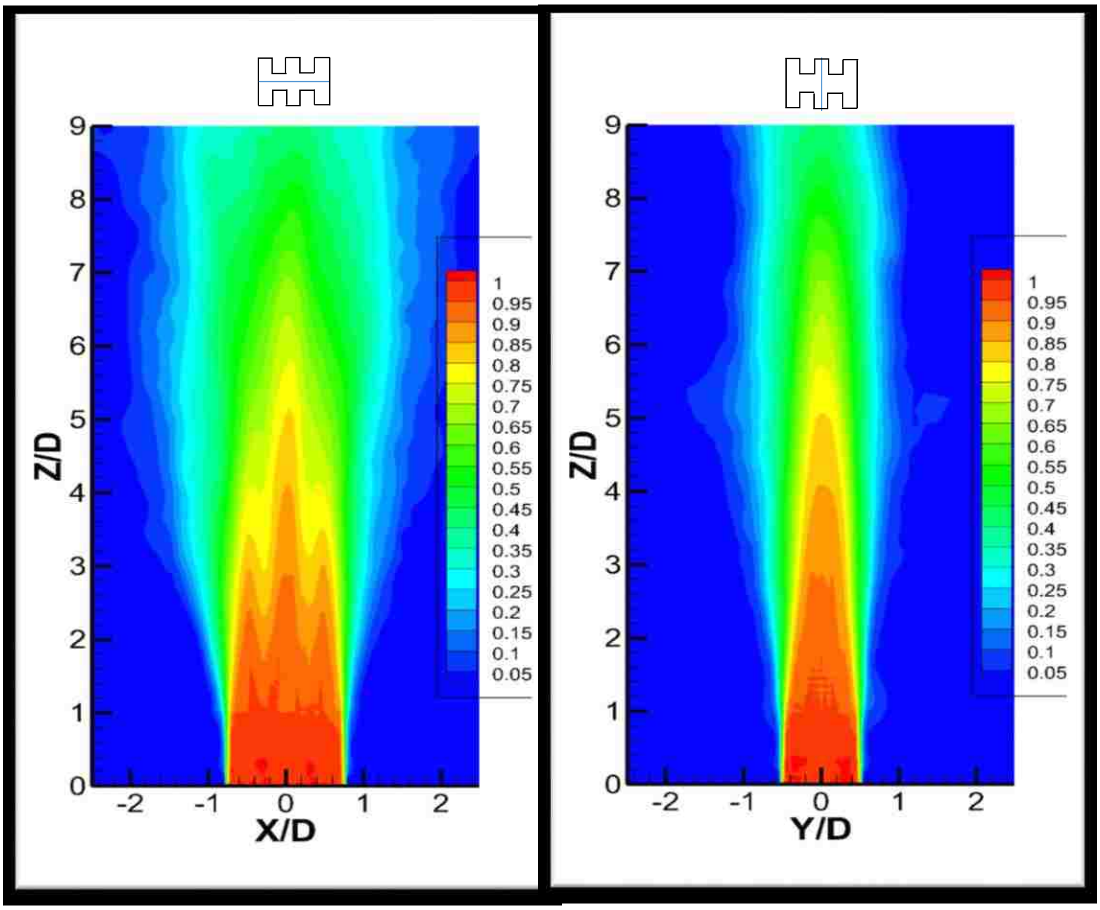

Figure 33 Normalized instantaneous streamwise velocity contours of 6-lobed jet in the XZ plane (left) and YZ plane (right) for Re=72000 at t=2s

More evidence to support the above deduction can be found in Figure 34, which is the profile of streamwise variations of the normalized centerline velocity W_{mean}/W_{inlet}. Figure 34 shows that the decay in centerline velocity of the 6-lobed jet is compared well with the experimental reference result [33]. Since we implement the fully developed outflow boundary condition, and our domain size is not long enough to capture this outflow physics, here we show the mean streamwise velocity profile in the region of $\mathrm{Z/D} < 10$. The velocity decay ($\mathrm{W_{mean}} < 95\%\ \mathrm{W_{inlet}}$) starts at $\mathrm{Z/D} < 4$, which is shown in Figure 34. In the region near the orifice, the jet spreads out with a constant rate. For $\mathrm{Z/D} < 6$, our Lattice Boltzmann results match well with the experimental results. However, for $\mathrm{Z/D} > 6$, especially in the downstream region where the core jet structure breakup, the jet decay rate in our Lattice Boltzmann result shows greater than the rate in experimentally measured profiles. This deviation may be caused by the simulation domain size, Smagorinsky coefficient in the LES model and outflow boundary condition.

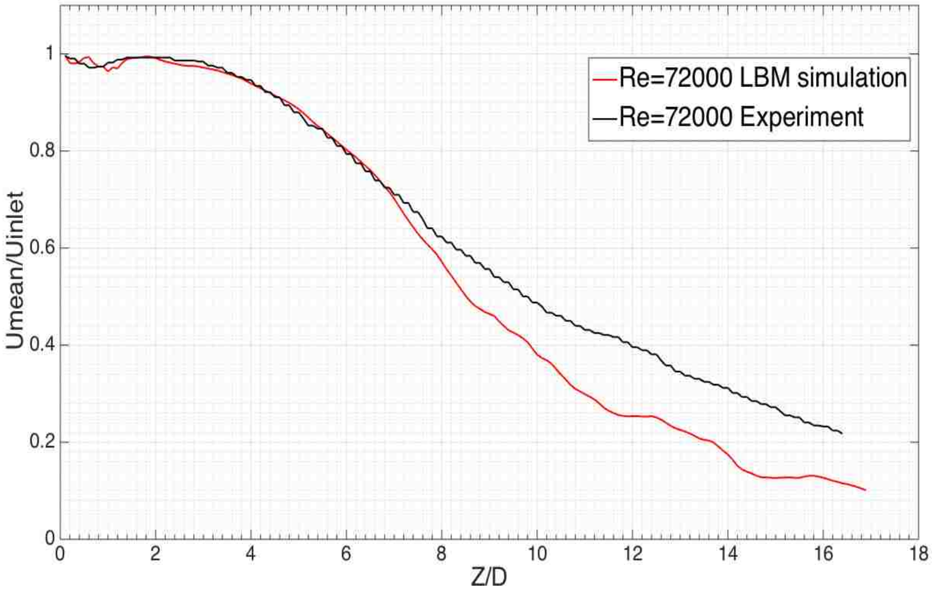

Figure 34 Comparison of centerline streamwise mean velocity with Mi 2010 *[33]* at Re=72000

For comparison, the circular jet spreads out consistently as it proceeds downstream, at a much lower rate than the 6-lobed jet in the minor plane (YZ plane), as shown in Figure 35.

Moreover, as illustrated by contours acquired at the minor plane in Figure 35, the mean velocity of the 6-lobed jet is deduced to decrease in the Z direction at a higher rate, yielding a shorter unmixed region. For the jet issued from the circular orifice, the end of unmixed region and the length of core jet is around $Z/D < 2$, which is much longer than the core length of the jet issued from the 6-lobed orifice. Based on above observations, the 6-lobed jet is deduced to spread and decay, overall, more rapidly than the circular jet. This implies a higher rate of entrainment of the surrounding fluid. In Figure 36 we show the comparison of the mean centerline streamwise velocity for the 6-lobed and circular orifice jet flows at Re=72000. In the region very close to the nozzle ($Z/D < 0.5$), a weak oscillation is observed both for the 6-lobed jet and the circular jet. This may be caused by the boundary layer and vena contracta mentioned in the circular jet section.

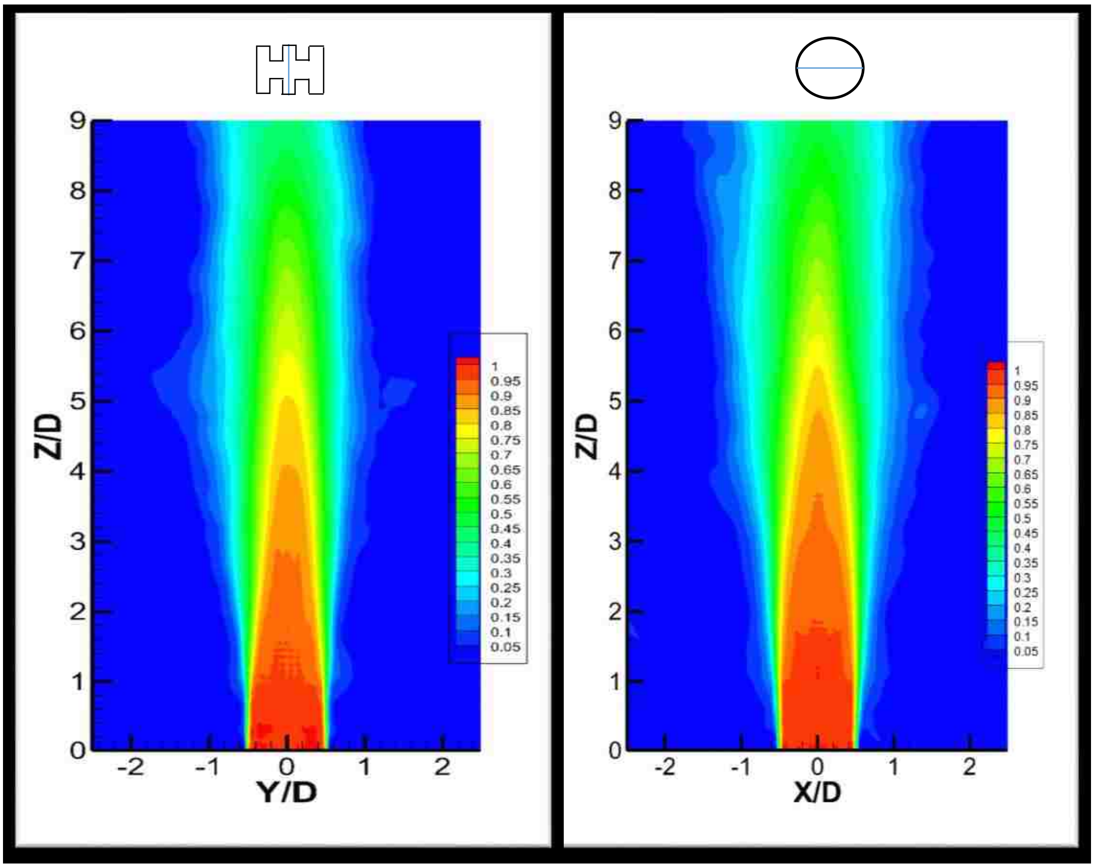

Figure 35 Normalized minor plane instantaneous streamwise velocity contours of 6-lobed jet (left) and circular jet (right) for Re=72000 at t=2s

Figure 36 shows that the decay in the centerline velocity of the 6-lobed jet is significantly faster than that of the circular jet in the near field. For the 6-lobed jet, the velocity decay starts at $Z/D \approx 2$, and for the circular jet, the location of the velocity decay is $Z/D \approx 4.5$. On the other hand, the core jet length of the 6 lobed jet is more than 2 times shorter than that of the circular jet. This also confirms the mean streamwise velocity decay observed in the velocity contours.

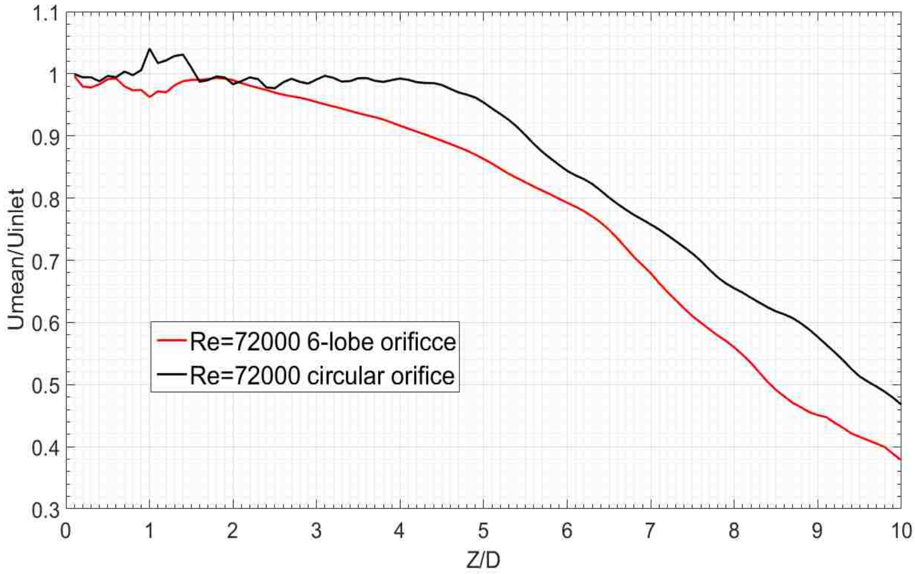

Figure 36 Comparison of mean centerline streamwise velocity for 6-lobed and circular jet orifice for Re=72000 case

3.3.3 Statistical Quantiles: Turbulence Intensity

Figure 37 show contours of the root mean squares (RMS) of streamwise velocity fluctuation of major plane (XZ-axis) and minor plane (YZ-axis) from $Z/D = 0$ to $Z/D = 8.5$ with the following definition:

$$W_{rms} = \sqrt{< \overline{W}^2 >} \tag{60}$$

where $\overline{W}$ is the streamwise velocity fluctuation.

Normalization is based on the inlet streamwise velocity W_{inlet}, and the contour values are indicated on the plots, ranging from W_{rms}/W_{inlet} = 0.02 to 0.24. These plots reveal the following. Firstly, in the region close to the orifice exit, the turbulence intensity is greater along the mixing layer, corresponding the vortex generation and core jet diffusion and dissipation. Secondly, the RMS of streamwise velocity fluctuation increases from $Z/D \approx 3.5$ and the rate increases rapidly from $Z/D \approx 6$, where the core jet decay starts and the core jet structure breakup starts. Then, the RMS of streamwise velocity fluctuation reaches the maximum value around $Z/D \approx 8$, where the peak value of the rate of energy dissipation is reached. In the region very close to the orifice exit $Z/D \approx 0.1$, because of the vena contracta effect, the jet noise is large and the RMS of streamwise velocity fluctuation is higher than the value of ambient.

More evidence of these trends is found from the centerline distribution of turbulence kinetic energy shown in Figure 38.

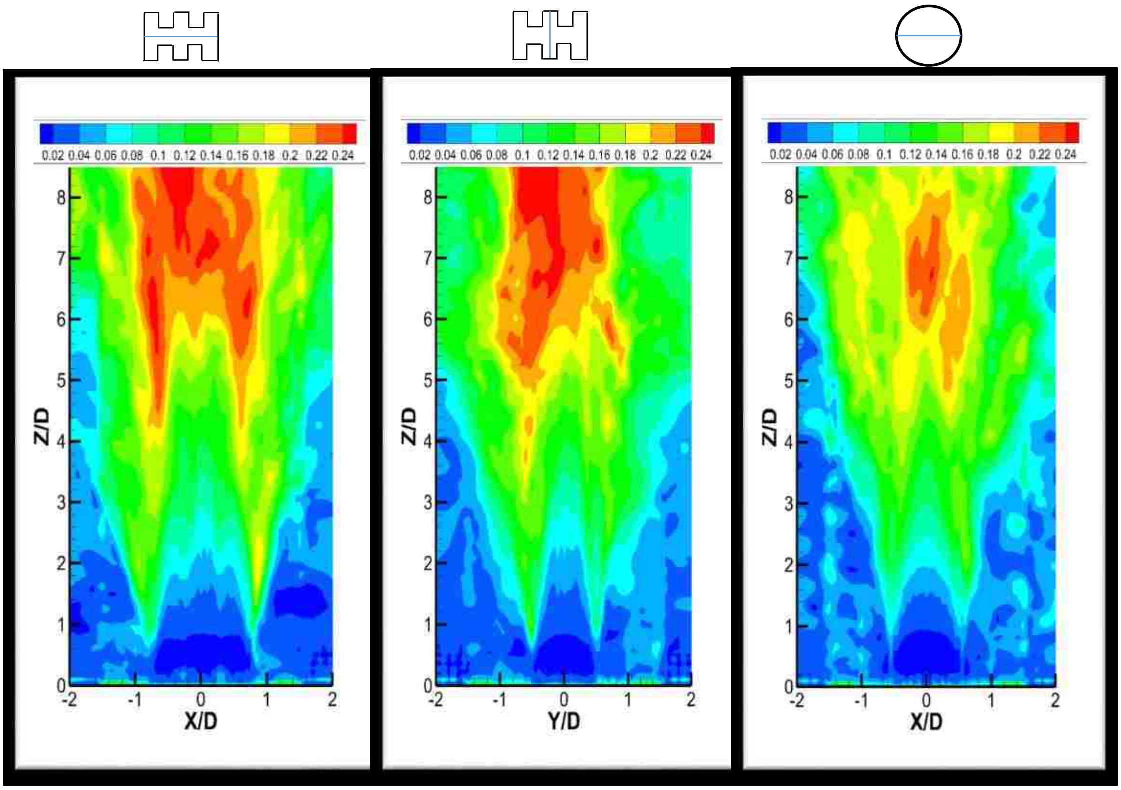

Figure 37 Contours of normalized RMS of streamwise velocity fluctuation at major plane of 6-lobed orifice jet (left); minor plane of 6-lobed jet orifice (middle); major plane of circular jet orifice (right)

The strength of normalized turbulence fluctuations may be assessed quantitatively by the distribution of turbulence kinetic energy, which is defined with the following equation as it is mentioned in the previous section,

$$\bar{k} = (0.5\sqrt{< \bar{U}^2 > + < \bar{V}^2 > + < \bar{W}^2 >})/U_{inlet} \tag{61}$$

Where, $\bar{U}$, $\bar{V}$ and $\bar{W}$ represent the z-components of the fluctuating velocity.

Here, we compare the centerline turbulence intensity and turbulence kinetic energy profile for the 6-lobed jet and the circular jet with experimental measurements at Re=72000.

Figure 38 shows the comparison of the results obtained by Lattice Boltzmann Method simulations and results of the experimental measurements. The turbulence kinetic energy remains constant to the location $Z/D \approx 2$, and increases to the peak value around $TI_N \approx 0.0145$ at location $Z/D \approx 7$ as predicted by LBM simulations and observed by experiments. The turbulence kinetic energy decreases along the streamwise direction in the downstream region. At $Z/D \approx 2$, the turbulence kinetic energy increases rapidly, which is also the evidence of the jet decay shown in Figure 34 for the mean streamwise velocity profiles. However, LBM simulations predicts that, the rate of turbulence kinetic energy increase is greater compared to that observed by experiments. This may be the results of the domain size limitation, filtering of the LES turbulence model, and the size of the computational domain.

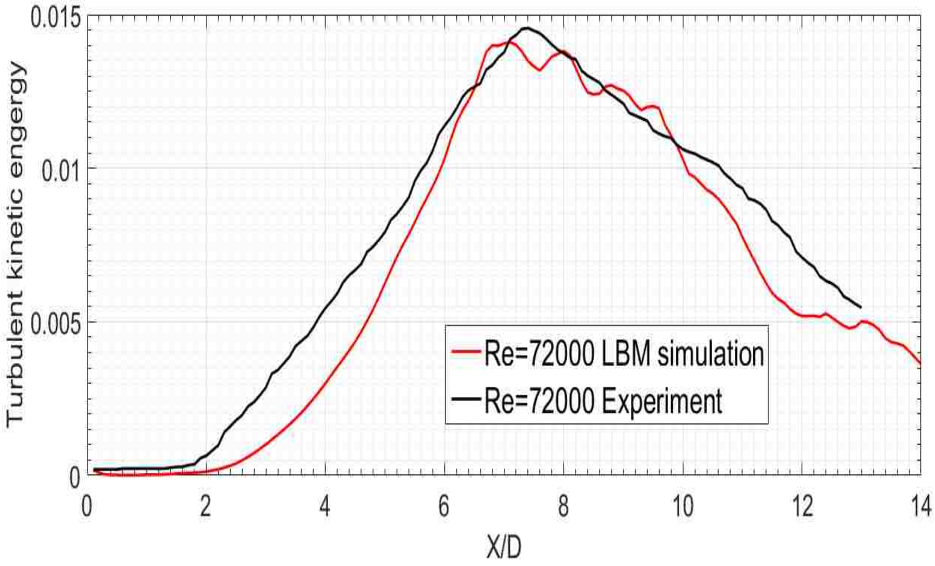

Figure 38 Comparison of centerline turbulent kinetic energy with Mi 2010 *[33]* at Re=72000

3.3.4 Vorticity field

For the circular jet, the vorticity structure mainly contains four regimes: I, vorticity layer; II, vortex rollup; III, vortex region; IV, vortex breakdown. However, for the notched jet, the vorticity structure is very different, as shown in Figure 39.

It is interesting to note that contrary to the circular orifice exit jet, no vortex rollup regime of Kelvin-Helmholtz structure is visible in the minor plane of the 6-lobed jet orifice exit case.

In the near-field of axisymmetric jet, as circular jet orifice in the present investigation, the growing of the Kelvin-Helmholtz instability produces ring-like vertical structures, which in their turn generate streamwise structures. Thus, it appears the production of streamwise structures in the circular jet is governed by

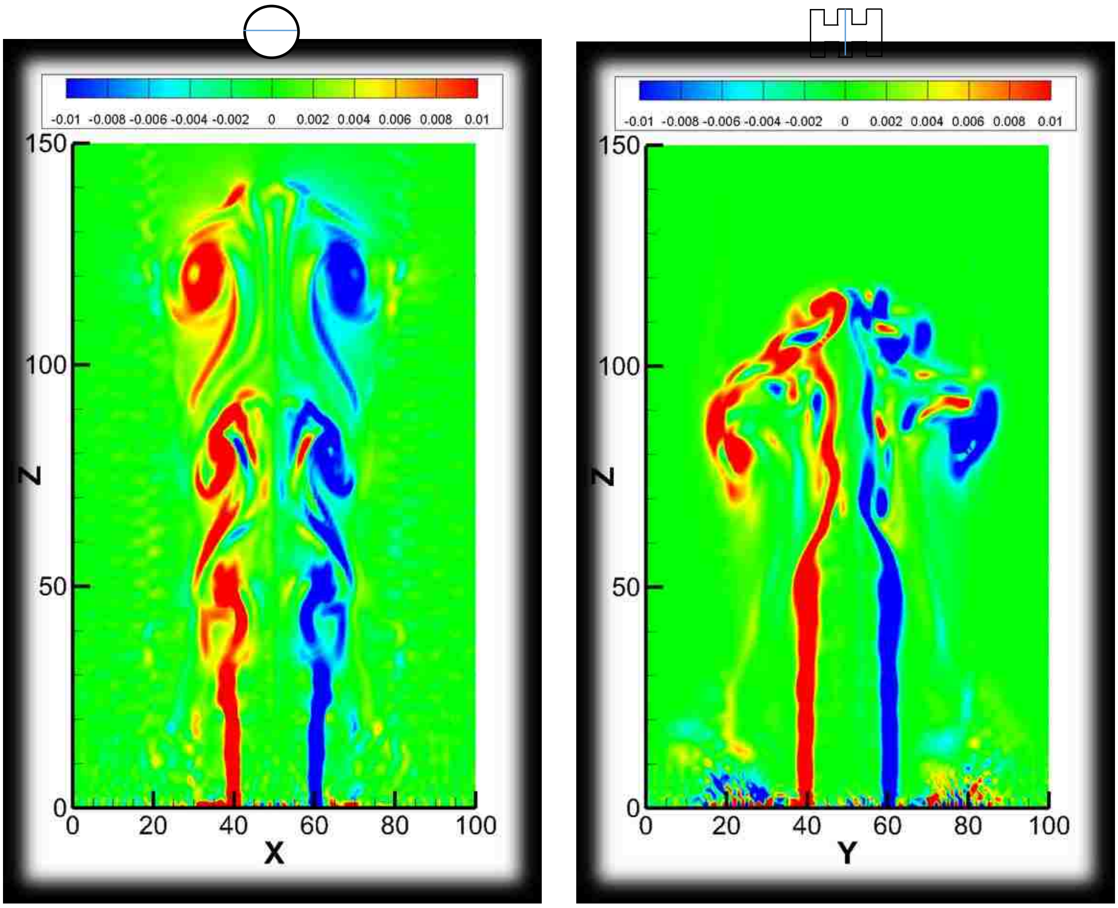

(a) circular nozzle exit

(b) 6-lobed nozzle exit

Figure 39 Instantaneous vorticity contours for Re=72000 case at t=0.006s: (left) circular nozzle exit major plane; (right) 6-lobed nozzle exit minor plane

the K-H rings. On the other hand, for the 6-lobed jet orifice, the streamwise structures are generated by the transverse shear induced by the shape of the nozzle and seem to dominate mixing phenomenon. These structures are very thin and only compression/depression cycles are observed and could be related to the effect of K-H instabilities in this jet. In addition, at the very near region to the orifice exit, the noise of the 6-lobed jet orifice is stronger than that of the circular one, corresponding to the shape of orifice exit and boundary layer at the near field of jet orifice.

3.3.5 Flow Images

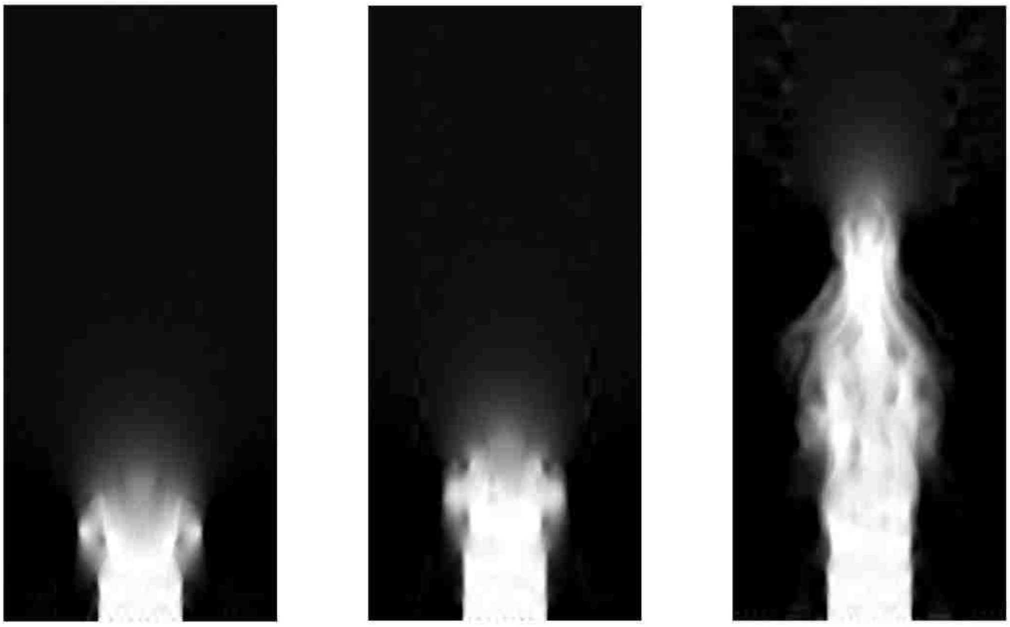

(a) t=0.0015s (b) t=0.0021s (c) t=0.0051s

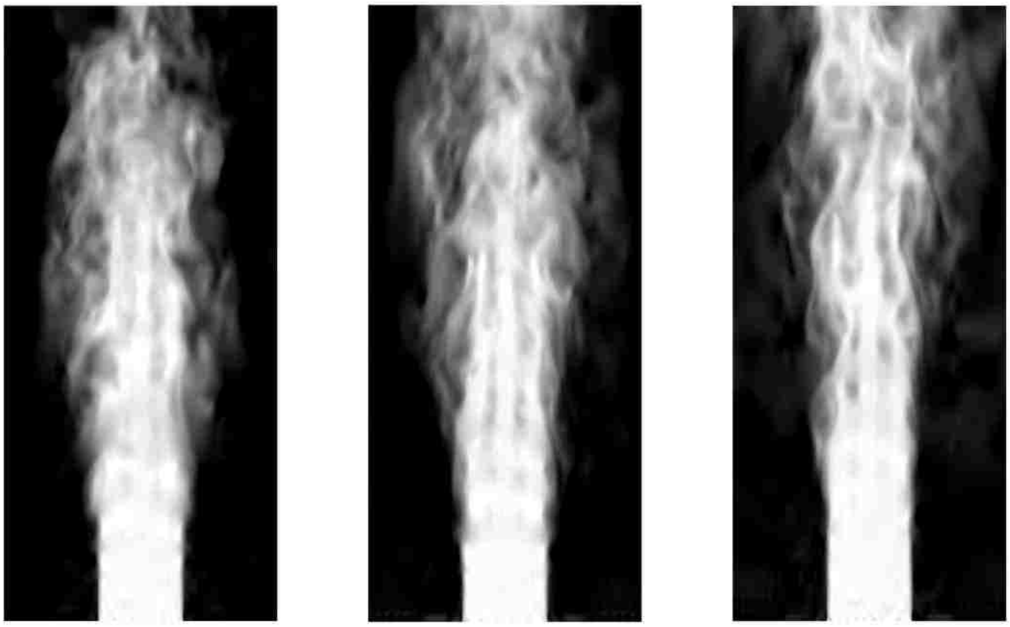

(d) t=0.0083s (e) t=0.0139s (f) t=0.0255s

Figure 40 Instantaneous flow images of 6-lobed jet at major plane streamwise velocity for Re=72000 case, at (a) 0.0015s; (b) 0.0021s; (c) 0.0051s; (d) 0.0083s; (e) 0.0139s; (f) 0.0255s

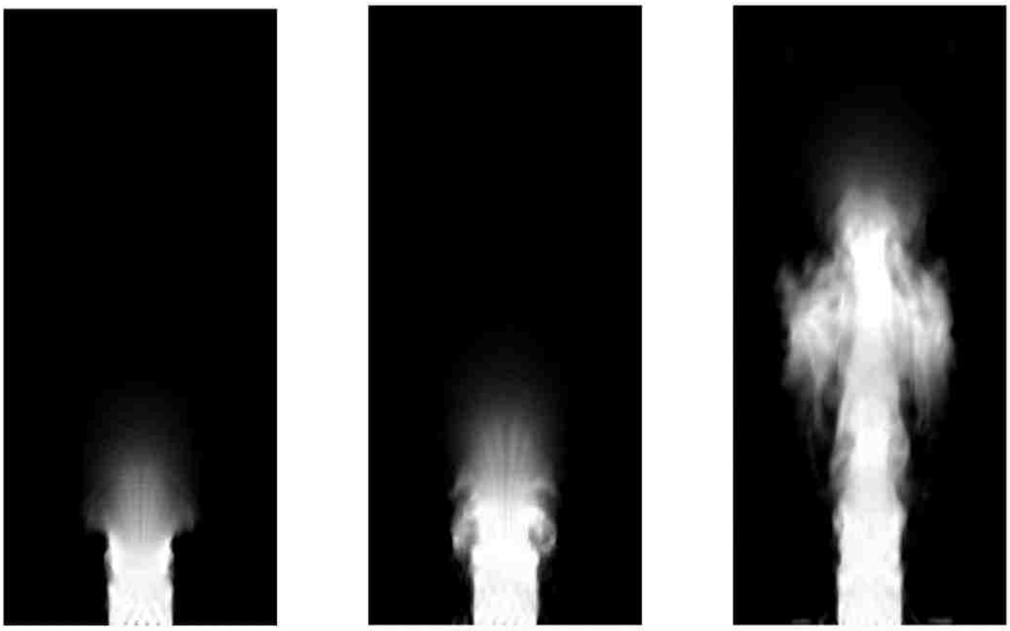

(a) t=0.0015s (b) t=0.0021s (c) t=0.0051s

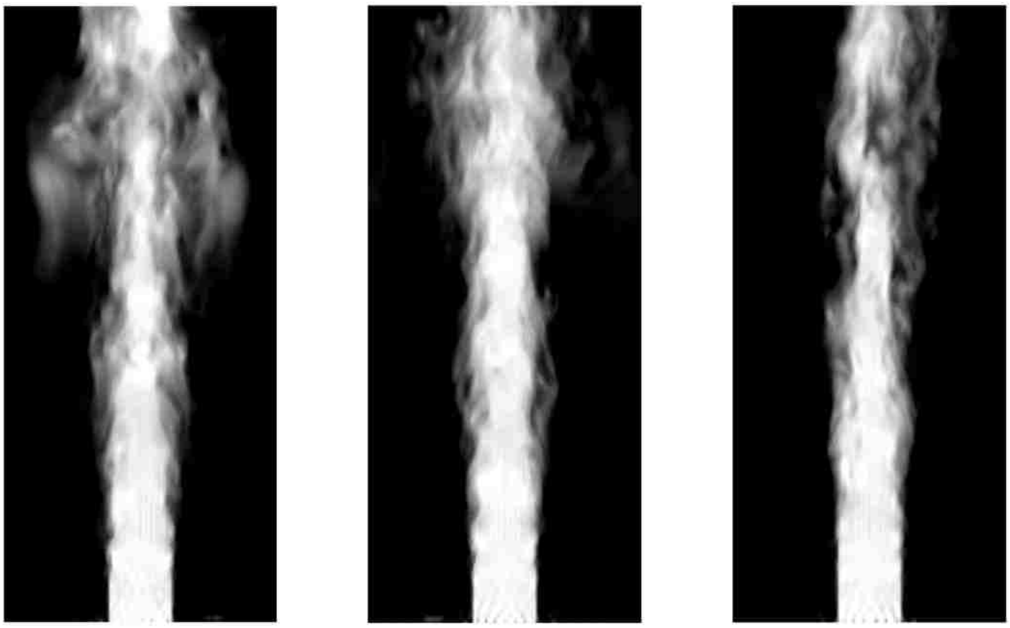

(d) t=0.0083s (e) t=0.0139s (f) t=0.0255s

Figure 41 Instantaneous flow images of 6-lobed jet at minor plane streamwise velocity for Re=72000 case, at (a) 0.0015s; (b) 0.0021s; (c) 0.0051s; (d) 0.0083s; (e) 0.0139s; (f) 0.0255s

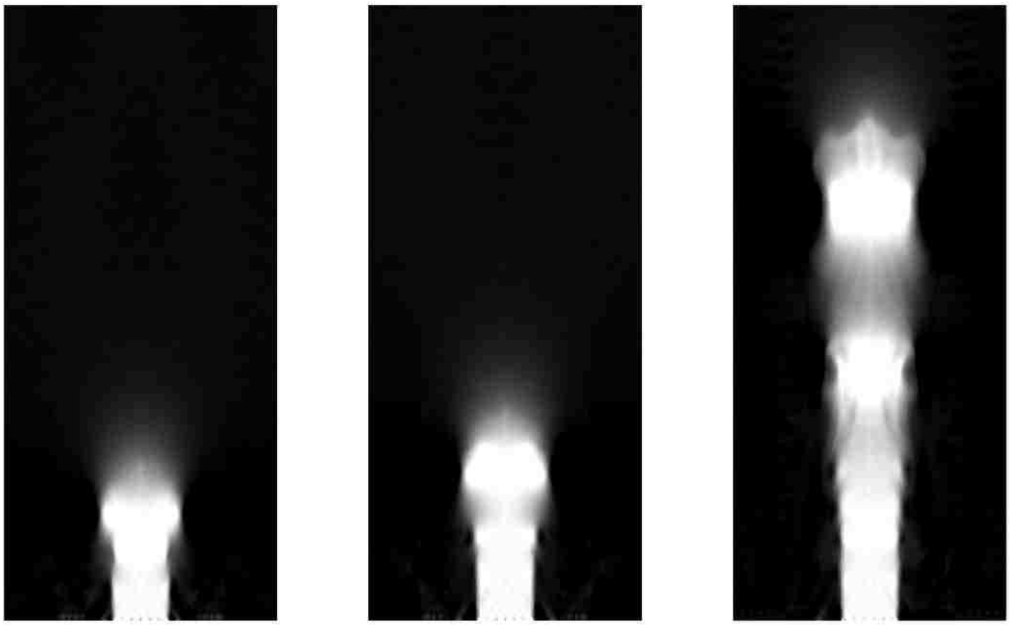

(a) t=0.0015s (b) t=0.0021s (c) t=0.0051s

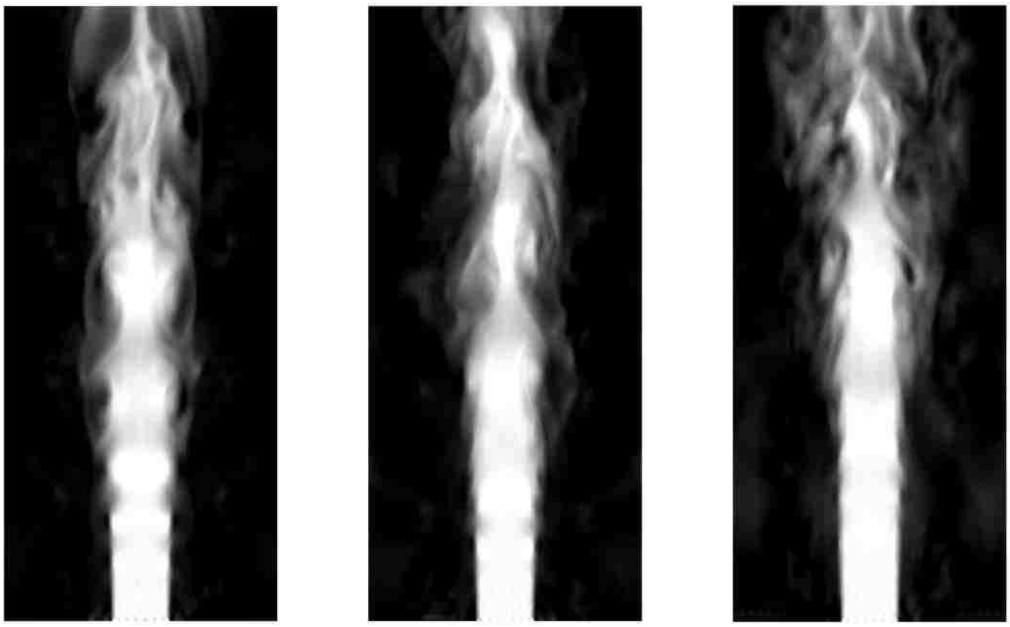

(d) t=0.0083s (e) t=0.0139s (f) t=0.0255s

Figure 42 Instantaneous flow images of circular jet at minor plane streamwise velocity for Re=72000 case, at (a) 0.0015s; (b) 0.0021s; (c) 0.0051s; (d) 0.0083s; (e) 0.0139s; (f) 0.0255s

We report here some flow images, which illustrate the most important characteristics that were presented and discussed earlier. Figure 40 and Figure 41 display six flow images at Re=72000 for the 6-lobed orifice at various flow times. Flow topologies are identified in the region close to the orifice *(Z/D* < 8.5). The images show the major plane and the minor plane jet generation and the core jet breakup phenomenon from 0.0015s to 0.0255s. Before 0.0021s, the jet generation is nearly symmetric and regularly shed from the main core. In the region very close to the orifice exit (*Z/D* < 0.2), high amplitude fluctuations are observed, which corresponds to the effect of the jet orifice vena contracta. The more irregular vortex generation is observed along the mixing layer between core jet region and the ambient air. After 0.0051s, the core jet region becomes asymmetric and the jet decay phenomenon is observed. After 0.0015s, the jet spreads out rapidly, where the core jet breaks up. The sub core jets, which are produced by the lobed orifice geometry, are very clear. The interaction between sub core jets results in decay of the main jet. The decay occurs in the region to the orifice exit compared to the circular jet. It is also demonstrated that the jet breakup and spreads out to the ambient occurs with a greater rate compared to that of the circular jet. On the other hand, for the minor plane images, the jet concentrate on the main region until the core jet breakup phenomenon is observed [40]. Comparison of flow images between the 6-lobed jet orifice case and the flow images of the circular orifice jet flow at the same Reynolds number is shown in Figure 42.

3.3.6 Conclusion

Lattice Boltzmann Method is utilized to simulate the single-phase jet flows issued from the 6-lobed rectangular orifice and the circular orifice. The velocity profiles and flow images are acquired for jet flows emanating from the lobed and circular orifice. Predicted flow field agrees well with the experimental measurements.

The predicted flow field at a wide range of Reynolds number for the 6-lobed rectangular jet is compared to its counterpart circular jet. In the region close to the orifice exit, the volumetric flow rate for the notched jet is significantly higher than that in the circular jet. It is shown that large ambient air is submerged at the orifice exit of the 6-lobed rectangular jet is due to the generation of large-streamwise structures in the troughs of the jet orifice, evidenced by flow images and mean streamwise distributions of axial mean velocity.

The 6-lobed rectangular jet exhibits a higher net entrainment of the ambient fluid over the entire measured region. The higher initial rate of turbulent diffusion is reflected in a faster initial decay of the mean velocity although this appears to decrease with the axial distance. Similarly, the notched jet has a shorter unmixed core. In this region, its cross-sectional-averaged (major and minor plane) kinetic energy grows faster than that in circular jet. However, the 6-lobed jet also presents a higher rate of destruction of the turbulence kinetic energy.

Chapter 4

Multiphase jet flows issued from a circular orifice

4.1 Introduction

Liquid atomization is an important process in engineering applications such as aerospace propulsion systems, automotive engines and inkjet printing. For engine applications, the fuel spray characteristics are critical to determine the engine performance such as fuel consumption rate or exhaust gas cleanness. Rapid liquid fuel atomization exerts an important influence on fuel/air mixing, and thus affects combustion performance significantly [41]. Here we study this atomization process using MCMP Lattice Boltzmann Method.

The liquid atomization process consists two steps: the near-field primary breakup and the downstream secondary breakup. As Figure 43 shows, liquid fuel is thought to be in the form of a continuous flow within a finite distance from the nozzle exit, beyond which the primary breakup occurs due to flow instabilities generated by aerodynamics as well as nozzle disturbances. Secondary breakup refers to further breakup of the droplets into smaller ones [42].

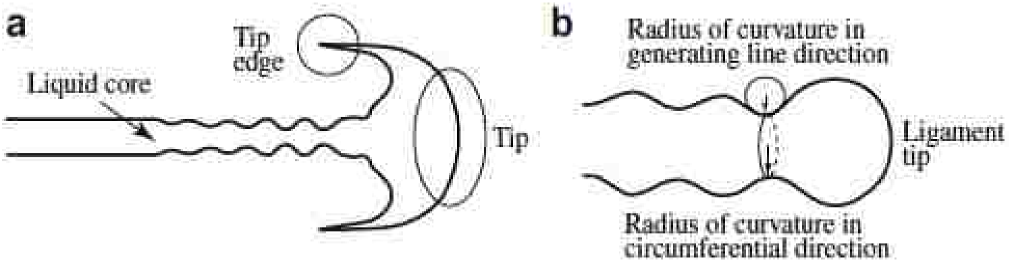

Figure 43 Name definitions for the propose investigation (a) liquid jet and (b) ligament

Multi-phase and multi-components flows appear in many natural and industrial processes. A liquid fluid flow jetting into another fluid is a wildly concerned and interesting example of such flow. Outstanding researches and works have been put into investigating the breakup and atomization phenomenon of a liquid jet for more than a century [43]. Drops form directly from the nozzle at low injection velocity and rate, and a liquid jet issues from the nozzle and then breaks into droplets in various patterns at higher injection velocities. The occurrence of such a regime is of interest in the study of liquid-jet breakup [44]. Ohnesorge classified his results into four types of breakup regimes: I: dripping, II: varicose, III: sinuous, and IV: atomization [23]. He also provided a regime map of liquid jets using the Ohnesorge number and Reynolds numbers as Figure 44 shown.

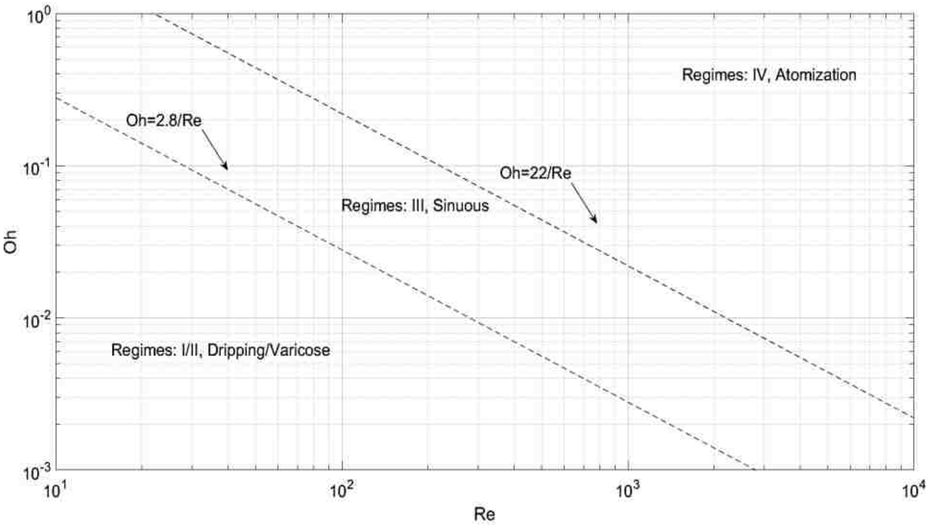

Figure 44 Location of simulation parameters on the regime map mentioned

After Ohnesorge's work, many researches on this subject have been performed. Most of investigation have focused upon liquid-gas systems. Breakup of jets in liquid-liquid systems has not been investigated extensively, especially implemented pseudopotential Lattice Boltzmann Method for numerical investigations. Saito et al.

applied color-fluid models, which are often referred to as P-K or color-gradient models, into water/silicon oil systems jet breakup study [45]. Similar with traditional multi-phase fluid flow method such as VOF and level set, color-fluid Lattice Boltzmann Method needs to define the phase fractions and track the phase separation processes. In our study, we use pseudopotential Lattice Boltzmann Method to avoid the phases tracking and implement the interaction forces to separate the two phases automatically by the algorithm itself. In this section, we present the three-dimensional two-phase Lattice Boltzmann Method for immiscible two-phase flows and its application to liquid-liquid jet breakup.

4.2 Droplets

Firstly, we simulated classical droplet case as the validation of this pseudopotential model. We set the non-dimensional density for oil to be 9.0 and for gas to be 0.01, so the density ratio is 900. The validation is the simulation of a circular droplet in a 200*200 lattice 2D square domain for a liquid-gas system with gravity force. The radius of droplet is set to be 20 lattice unit and gravity force is set to be 2.0e-5 lattice unit. No-slip nun-wetting boundary condition is applied on the four boundaries. Figure 46 shows the density contours at different times and Figure 45 shows the comparison of the density of the two components along the centerline (y=100, $0 \ll \mathrm{x} \ll 200$) on a log10 scale. In Figure 45, the density of component 1 in the droplet ($\rho_{component1}$,max) is on the order of 10^1, while the density of component 2 around the droplet ($\rho_{\mathrm{component2}}$,max) is on the order of 10^{-3}. Hence, the density ratio of these two components is around 900:1. In general, the density ratio of a system refers to the ratio between the maximum densities of the two components

$(\frac{\rho_{component1},\max}{\rho_{component2},\max})$. The diffusion effect is reduced to critical level, which means two unmixable components cannot occupy the same physical space at the same time. In this validation, oil cannot flow into the space that the gas has already occupied. This means that the density of oil should be zero (or an extremely small value) in the area where the density of air takes precedence.

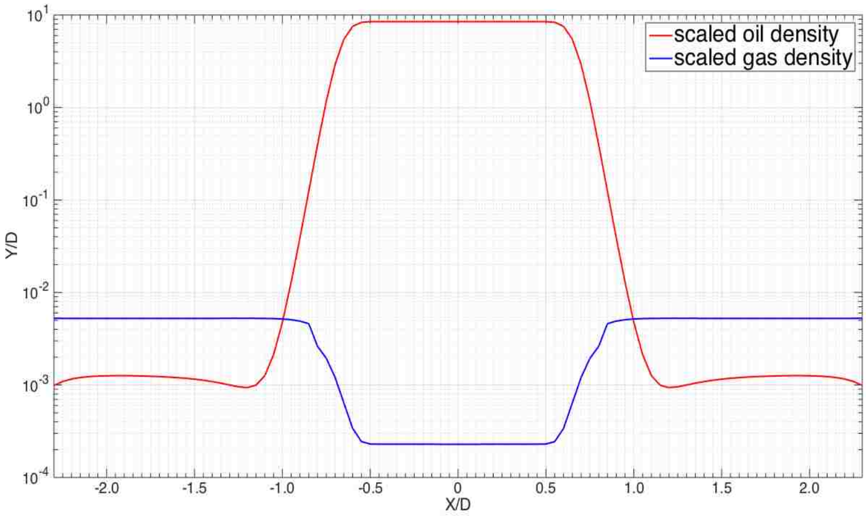

Figure 45 Comparison of log10 scales density of components along y=100 for oil and air system 900:1

In Figure 46, the droplet density contours at different times are shown. The diffusion effects and mixture nodes are limited to significantly small level. The density inside and outside of the droplet is converged around the initialized values. The droplet falls, which is dominated by the gravity force. After the droplet touched the bottom boundary, the deformation of droplet shape is observed clearly. The droplet spreads as time passing. Due to the nun-wetting boundary, the droplet bounces back eventually, and the shape of droplet restores to circle. From this validation, the modified Shan/Chen model with Peng-Robinson EOS can handle large density ratio multi-phase problems and will be implemented into the liquid-gas Lattice Boltzmann Method solver development.

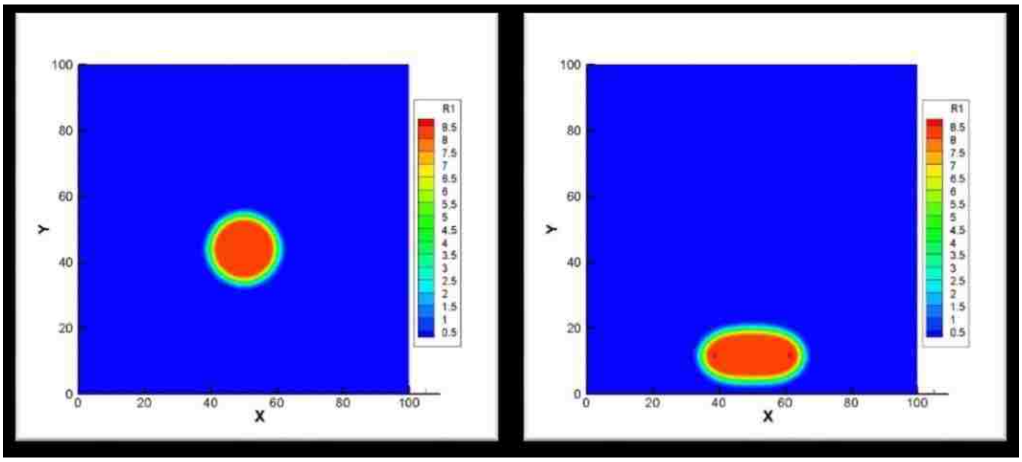

T=0.001s

T=0.00283s

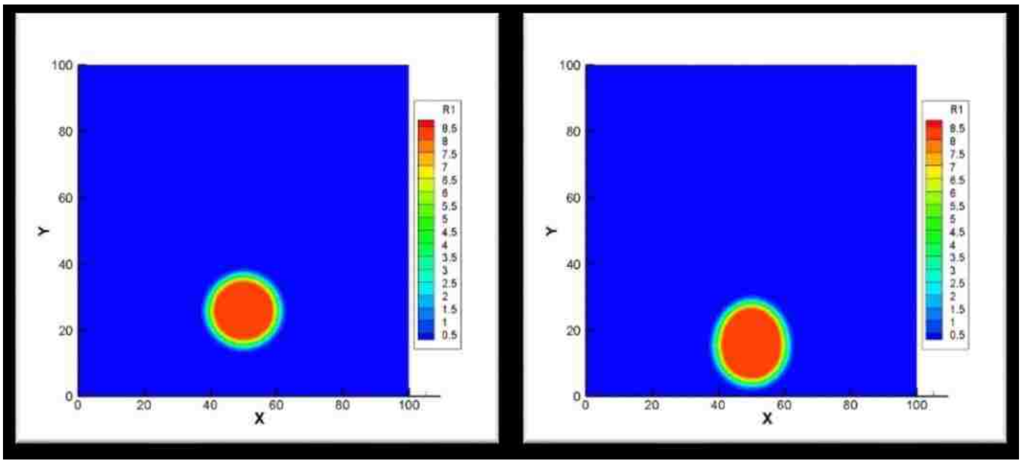

T=0.002s

T=0.0032s

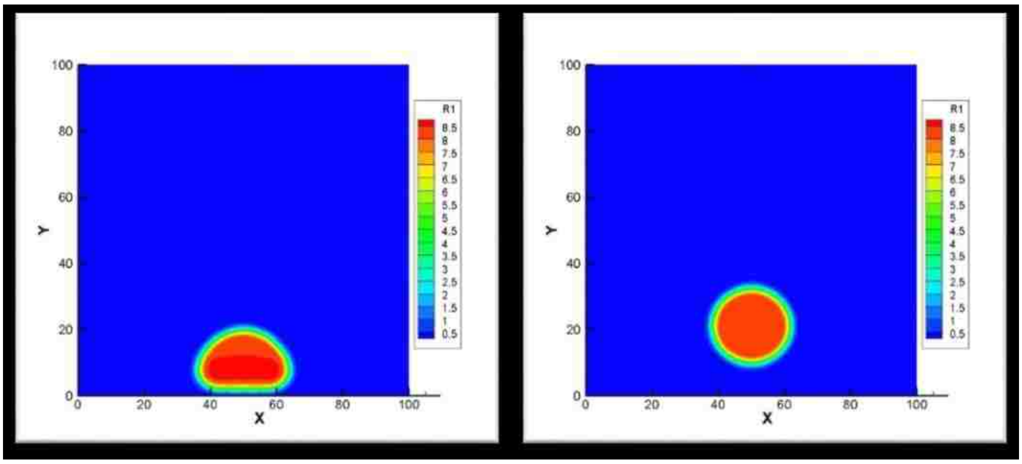

T=0.00273s

T=0.0036s

Figure 46 Density of Oil contour at t=0.001s, 0.002s, 0.00273s, 0.00283s, 0.0032s and 0.0036s

For the study of interaction strength G_{ij} between different components, we set up various static droplet without body forces and external forces with different G_{ij} simulations to compare the diffusion effects. The domain size is 60*60*100 and the droplet is mounted in the middle of the domain. The no-slip boundary condition is implement on top, bottom and four side walls. We increase G_{wo} from 0.2 to 0.7 and G_{ow} from 0.2 to 1.0 as the Figure 47 shown, which is the densities of two components along centerline z=30, y=30, 0≤x≤100.

We set $\tau = 1$, $G_{w/w} = -5.7$, $G_{o/o} = -3.7$.

Comparing with large density ratio case, we set the effective mass as:

$$\psi_w(\rho) = 1 - e^{(1-\rho_w)}$$

$$\psi_o(\rho) = 1 - e^{(1-\rho_o)}$$

Where ρ_w and ρ_o are the local density.

We set $\rho_w = 2.6$, $\rho_o = 1.98$ and $\rho_{initial} = 0.1$ and $\vartheta_w = 0.1667$ (the relaxation time for water is $\tau_w = 1$) and $\vartheta_o = 0.119$, thus the density ratio is 1.3 and viscosity ratio is 1.4. Unlike the previous large density ratio droplet validation, in this simulation, we set the density ratio as same as water and silicon oil as reference shown at small level [45]. Hence, we use original Shan/Chen model to modify the effective mass and calculate the interaction forces between same and different components. Our objective density ratio for water-silicon oil jet breakup is under small level, thus original Shan/Chen pseudopotential model can limit the diffusion effect between two components under acceptable small range. As G_{ow} increased from 0.2 to 1.0, the density of oil inside the droplet decreased to the initialized density. Oppositely, for water component, the density of water inside the droplet increase with G_{wo} increases and cannot be converged around initial density. Also, as G_{ow} increases, the radius of droplet is converged to the initial value, and the droplet maintains the original shape that we set at the initialization step.

Through the interaction strength study, we find at $G_{wo} = 0.2$ and $G_{ow} = 1.0$, the densities of water and silicon oil are converged well around the initial values both inside and outside of the droplet. Thus, after interaction strength study, we choose $G_{wo} = 0.2$ and $G_{ow} = 1.0$ for the Laplace analysis simulations and 3D droplets with gravity force for the validation purposes.

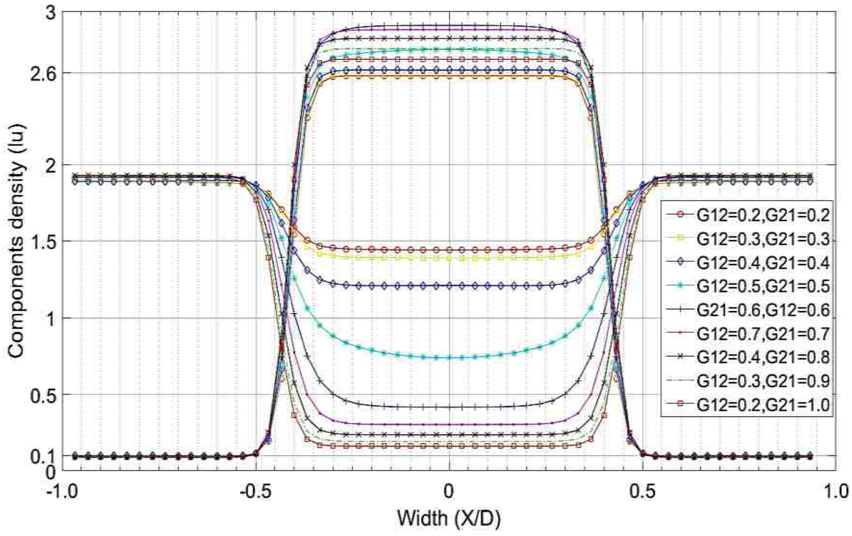

Figure 47 Comparison of density of components along centerline (z=30, y=30, 0≤x≤100)

The comparison of normalized density of components (Droplet radius is 15) along the centerline (z=30, y=30, $0 \leq x \leq 100$) at $G_{wo} = 0.2$ and $G_{ow} = 1.0$ is shown as Figure 47 and Laplace analysis is shown in Figure 49. We use the following equation to normalize the density of each component:

$$\rho_{w.n} = \frac{\rho_w - \rho_o}{\rho_w + \rho_o} \qquad (62)$$

In the Figure 48, Inside the droplet, $\rho_{w,n} \approx 0.89$ and $\rho_o \approx -0.89$, and outside the droplet, , $\rho_{w,n} \approx -0.91$ and $\rho_o \approx -0.91$. For inside of the droplet, silicon oil occupies 11% of the component density, and can be considered as pure water. On the other hand, water occupies 9% of the component density outside of the droplet and can be considered as the pure silicon oil. The diffusion effect occupies 6 lattice nodes, which means two unmixable components cannot occupy the same physical space at the same time and the diffusion effects is limited under significant level.

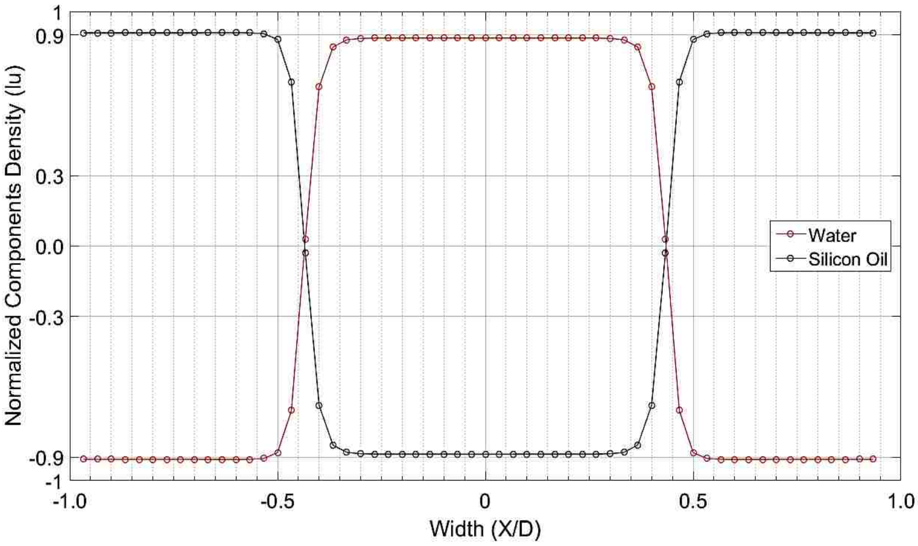

Figure 48 Normalized components density along centerline (z=30, y=30, $0 \leq x \leq 100$) at G12=0.2, G21=1.0

Before setting up the further multi-phase simulations, we want to discuss about the simulation of surface tension. The typical numerical experiment to assess the surface tension is to simulate a droplet in a gravity-free domain. Laplace law is used to calculate the surface tension force, which states that the pressure jump across the phase interface is linearly proportional to the reciprocal of the radius of the droplet, and the slope of the line is the surface tension force [46].

The Laplace equation in three dimensions is given by

$$\Delta P = \frac{2\sigma}{R} \tag{63}$$

Where ΔP is the pressure difference between cross-face inside and outside of the droplet, R is the droplet radius and σ is the analytical surface tension.

A series of simulations are conducted by changing initialized droplet radius from 18 to 27. Figure 49 plots ΔP as a function of 1/R, where the linear relationship can be clearly observed, which satisfies Laplace law [47]. The slop of the line is the surface tension σ, which is assessed as 0.9193.

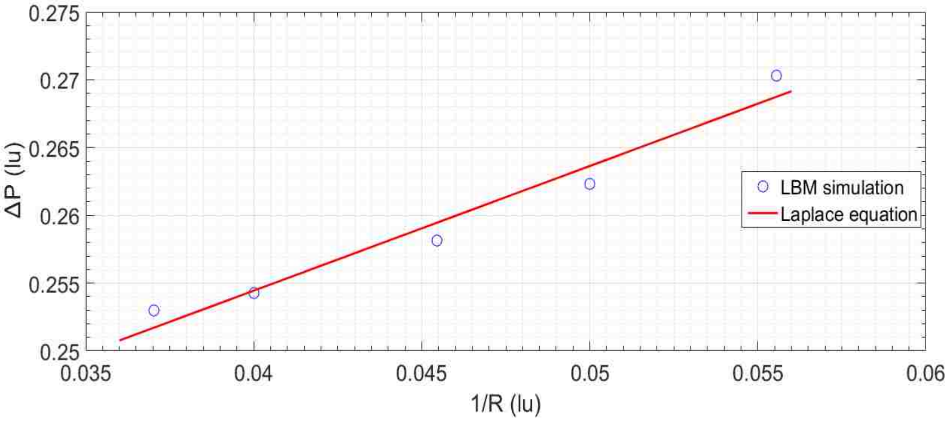

Figure 49 LBM results of pressure difference versus inverse of droplet radius for static droplet radius

For the gravity force included investigation, we set the 3D simulation domain to be 60*100*60 lattice unit for a water-silicon oil system with gravity force 4e-5. No-slip boundary condition is applied on the top and bottom boundaries, and periodic boundary condition is implemented for four sides.

We set $\tau_w = 1$, $G_{w/w} = -5.7$, $G_{o/o} = -3.7$, $G_{wo} = 0.2$ and $G_{ow} = 1.0$. The density ratio is 1.3 and the viscosity ratio is 1.4. Thus, the density of water and silicon oil is $\rho_w = 2.6$, $\rho_o = 1.98$, and the viscosity of water and silicon is $\vartheta_w = 0.1667$ and $\vartheta_o = 0.119$. The initial location of droplet is at x=30, y=60 and z=30. The effective mass is set as the previous static droplet simulations following original Shan/Chen model. The initialization is same as the previous static droplet simulations. The total simulation time step is 1200 with time scale 1.23e-3s, thus the total simulation time is 1.46s.

Wetting phenomena are not only wide spread in nature but also play an important role in many scientific and industrial processes. For most problems involving surface effects, fluid-solid interactions are particularly important for meso-/micro-/nano-scale devices, where the physical behavior is largely affected by high surface volume ratios [48]. Contact angle is usually considered as a measure of the solid surface wettability. It is defined as the angle at which the fluid/fluid interface meets a solid phase [49]. A fluid is wetting if its contact angle $\theta < 90^o$, and this fluid tends to spread as a film on the solid surface. Oppositely, the fluid is non-wetting if $\theta > 90^o$, and the fluid tends to form a droplet on the solid surface [15]. In our liquid-liquid system jet, we implement the wetting boundary for the top no-slip wall and need to control the contact angle between water and solid boundary.

It is easy to implement the fluid-solid interaction and wetting conditions in pseudopotential Lattice Boltzmann Method. The interaction force between the fluid and the solid wall can be calculated by the following Eq. 64:

$$F_{s,\sigma}(X) = g_w \psi(\rho_\sigma) \sum_{\alpha=1}^{N} w(|e_\alpha|^2)\, \psi(\rho_{solid}) s(x + e_\alpha) e_\alpha \tag{64}$$

where ψ_{solid} is an indicator function that equals 1 for solid nodes and 0 for fluid nodes. g_w and ρ_w can be tuned separately or jointly to achieve different contact angles. There are generally two methods to obtain different contact angles. First, with fixed g_w and tuning ρ_w to obtain the desired contact angle. Second, a widely used approach is fixing $\psi(\rho_w) = 1$ and tuning g_w to achieve the desired contact angle [15].

Here, we use the second way to do the validation droplets simulations with modified g_w to obtain the desired contact angles. The validation simulation experiment for obtaining different contact angles is putting an initial static droplet with fixed radius and changing F_{ads}. The simulation domain size is 60 * 100 * 60, and the droplet with $R_{initial} = 15$ located at x=30, y=30, z=30 initially. We set gravity force to be 1.9e-5, $\rho_{water,initial} = 2.6, \rho_{oil,initial} = 1.98, \vartheta_{water} = 0.1667\ and\ \vartheta_{oil} = 0.119$ to obtain the density ratio $r_{density} = 1.3, and\ r_{vosicosity} = 1.4$ accord with the liquid-liquid systems jet investigations setting. We simulate the $\tau = 1$ case for the validation. The simulation of using the second method of fixing $\psi(\rho_w) = 1$ tuning g_w in the range from -4.0 to -1.5 is presented. The top and bottom boundaries are set to no-slip wall and the four surrounding sides use periodic boundary conditions. Since the difference of two components densities is small, we use classical Shan/Chen model. The effective masses of two components are set as:

$$\psi_w(\rho_w) = 1 - e^{(1-\rho_{water})}$$

$$\psi_o(\rho) = 1 - e^{(1-\rho_{oil})}$$

The insets in the Figure 50 show typical droplets with different contact angles. After the simulation is converged, the base length of the interface between water and oil at the bottom wall 2b, and the height of steady state droplet form h are measured in the post-process. To this end, phase interface should be determined which is defined at the position where the density is $(\rho_{water,inital} + \rho_{oil,initial})/2$. The contact angle can be calculated by

$$r = \frac{h^2+b^2}{2h} \tag{65}$$

$$\theta = \begin{cases} arcsin\left(\frac{b}{r}\right), & \theta \leq 90^o \\ \pi - arcsin\left(\frac{b}{r}\right), & \theta > 90^o \end{cases} \tag{66}$$

In Figure 50, the insets show droplets with different contact angles. The contact angle increases from 53.1^o to 129.2^o with the interaction strength g_w increases from -4.0 to -1.5. The clear linear relationship between contact angles and interaction strength of fluid-solid is observed. Unlike the traditional top down approach where macroscopic properties including surface tension and contact angle can be prescribed, in the pseudopotential model, the value of the contact angle is not modified directly in the model itself, although there is a linear functional relationship between the steady state contact and the interaction strength, which is shown in Figure 50:

$$\theta = 28.4 g_w + 165.13$$

[redacted]

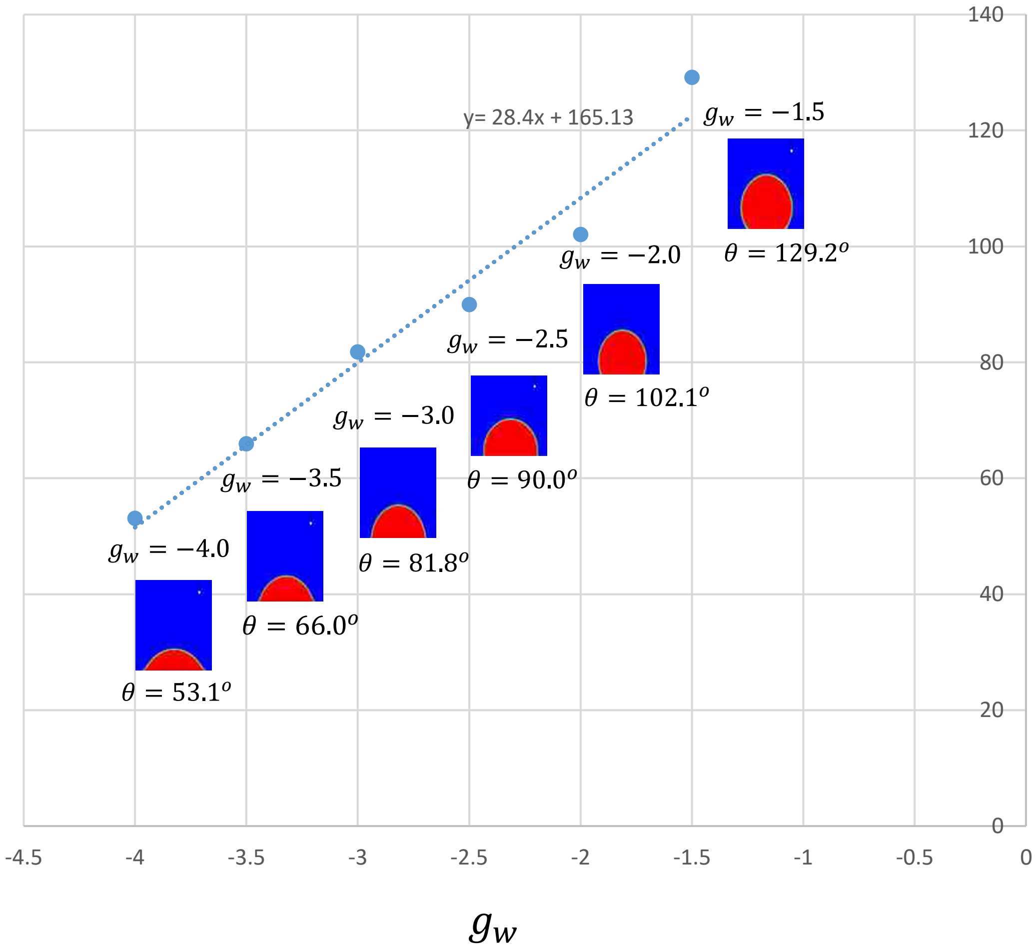

Figure 50 Simulation results of different equilibrium contact angels for a liquid droplet on a flat and uniform no-slip solid wall with different liquid-solid interaction strength g_w

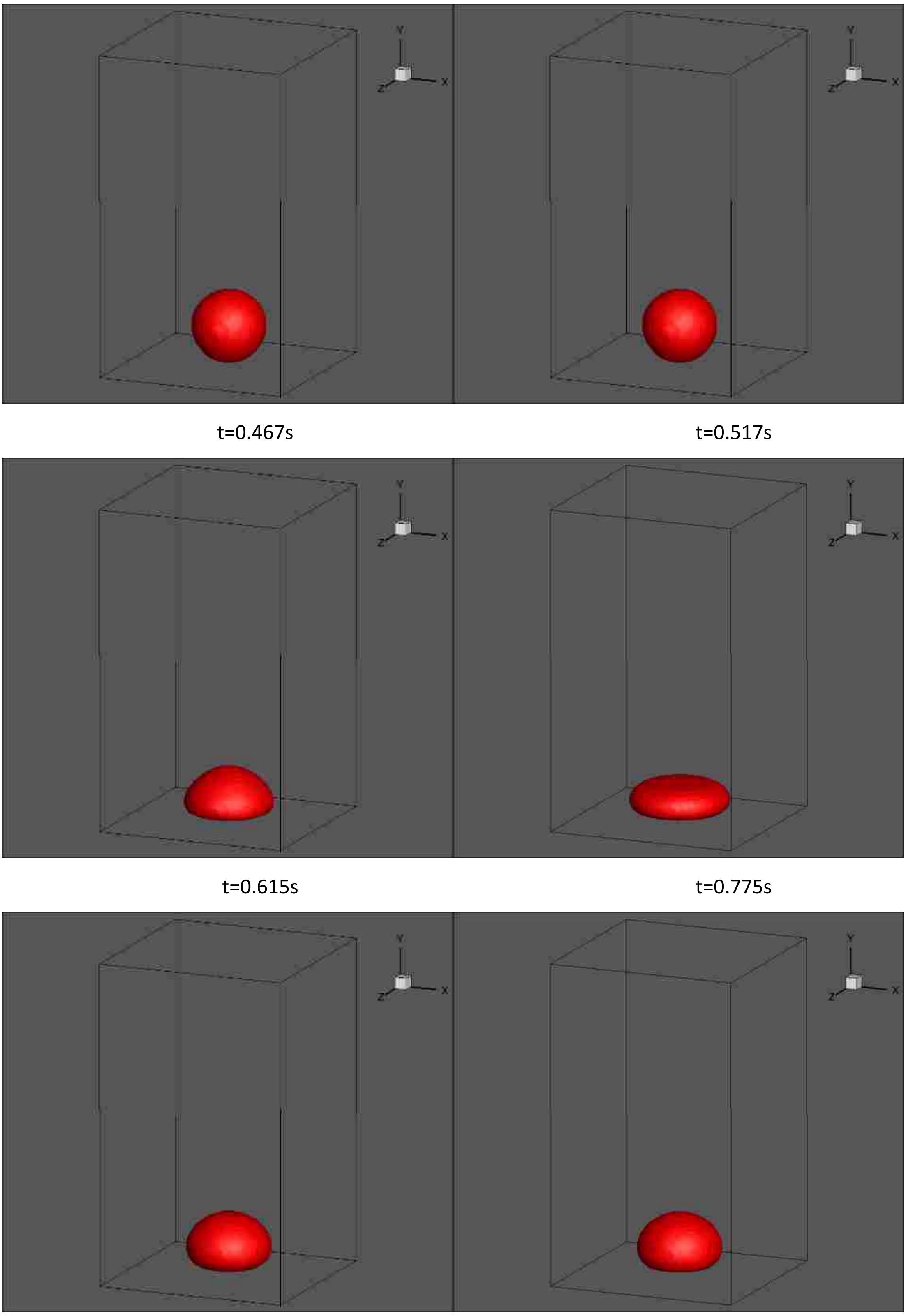

t=0.467s

t=0.517s

t=0.615s

t=0.775s

t=1.107s

t=1.476s

Figure 51 Instantons Iso-surface of Droplets deformation at g_w = -1.5

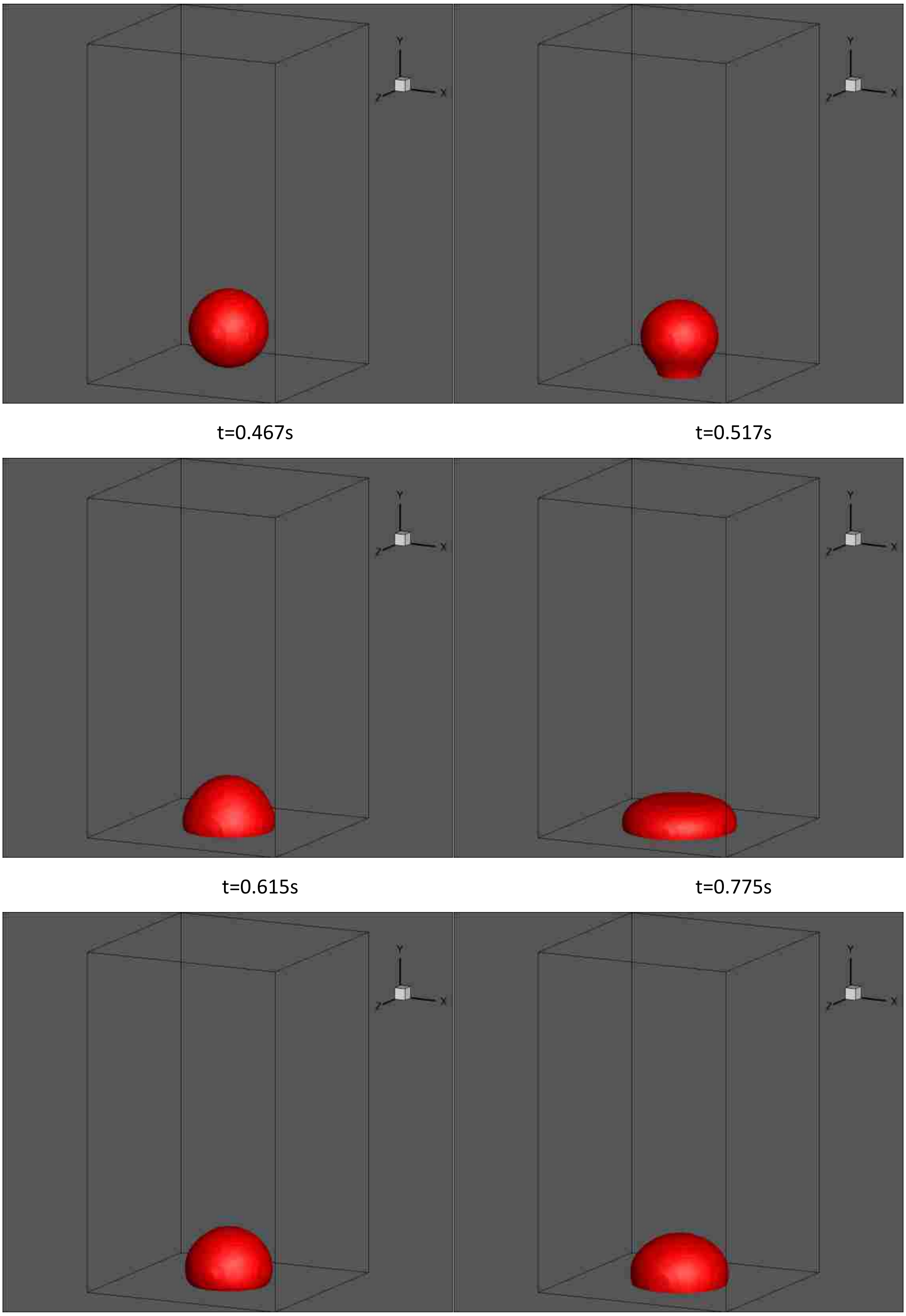

t=0.467s t=0.517s

t=0.615s t=0.775s

t=1.107s t=1.476s

Figure 52 Instantons Iso-surface of Droplets deformation at g_w = -2.5

The lattice unit properties for each component and the body force included such as gravity force determines this linear regression functional relationship we set initially [15].

The instantaneous iso-surface of droplets formation is shown in Figure 51 and Figure 52 for different two strength of interaction force between fluid-solid, which are $g_w = -1.5$ and $g_w = -2.5$.

As Figure 51 shows, the instantaneous Iso-surface of droplets deformation with fluid-solid interaction $g_w = -1.5$ included are presented. Before t=0.467s, the deformation of droplet appears since the initialization, then the shape of droplet is converged to the original setting and the radius of droplet is converged to 15 lattice unit. At t=0.517s, the droplet touched the bottom, and the deformation of the droplet, which is mainly due to the interaction force between fluid and solid, is observed. After t=1.476s, the form of droplet is converged with the predicted contact angle attached the solid bottom no-slip wall.

As Figure 52 shown, with the fluid-solid interaction strength increased to $g_w = -2.5$, the form of droplets attached to the bottom is converged after t=1.476s lattice time step and the contact angle is 90^o as we predicted.

4.3 Simulation setup

Figure 53 illustrates a schematic diagram of the boundary conditions for liquid-liquid system jet simulations. In the initial state, the computational domain is filled with silicon oil particle-distribution functions, g_∂, with zero velocity and initial density value, $\rho_{initial} = 0.1$. The boundaries consist an inflow boundary, periodic boundaries and outflow boundary. A circular inflow boundary is implemented at the top within $(x - x_c)^2 + (y - y_c)^2 < D_e^2$, where (x_c, y) is the center location of nozzle exit and D_e is the equivalent jet orifice diameter.

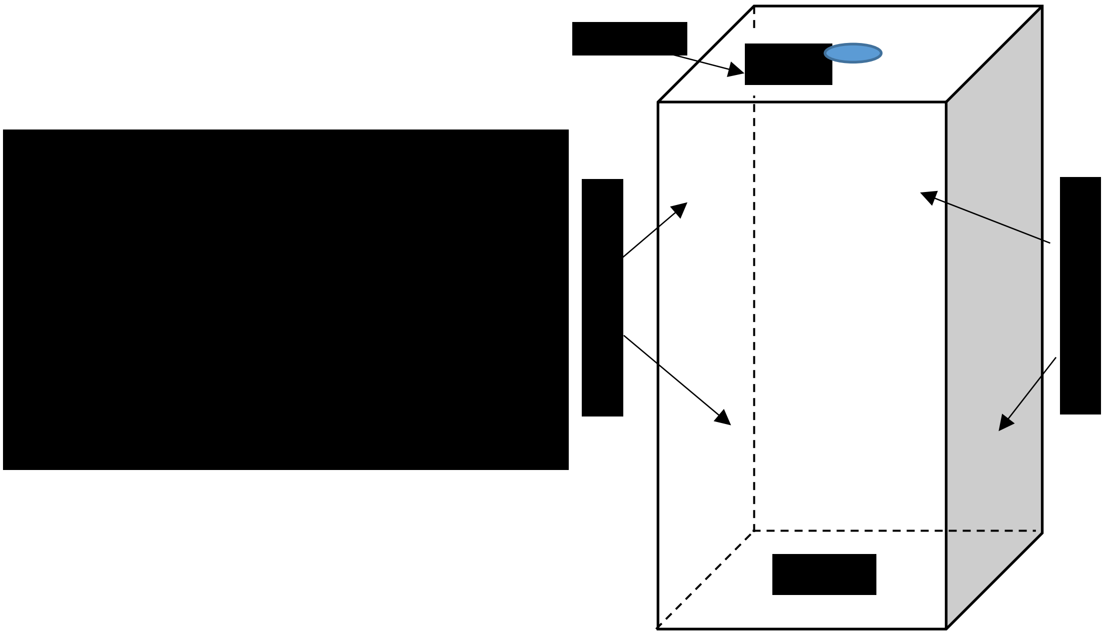

[redacted]

[redacted]

[redacted]

[redacted]

[redacted]

[redacted]

Figure 53 boundary conditions for liquid-liquid system circular jet simulation

The uniform streamwise velocity is applied for the inlet boundary conditions, with the corresponding equilibrium distribution functions given at this site. A no-slip bounce back boundary condition is implemented on the top except the inflow region. In order to increase the computational efficiency, save computational time and reduce the domain size, we use the periodic boundary condition for the side boundaries. At the outflow, we use the fully-developed boundary condition, which is mentioned in Chapter 3 as the following equations for both components:

$$f_a(nz) = f_a(nz - 1)$$

$$g_a(nz) = g_a(nz - 1)$$

The body force in Eq 32. for the liquid-liquid system jet simulation is set as

$$F_{b,\sigma}(X) = \rho_\sigma g \tag{67}$$

with $\vec{g} = (0,0,g)$.

We investigate low Reynolds number case with our pseudopotential Shan/Chen Lattice Boltzmann Method for Re=460, and compare the result with reference, Saito, et al [45]. The conditions of the simulation are summarized in Table 6 and in the dimensionless groups in Eq. 68-73.

We determine the dimensionless inlet diameter $D_e = 20$ and the computational domain $5D_e \times 5D_e \times 15D_e$. In this investigation, the density of the water $\rho_w = 2.6$ and the inlet velocity $w_{inlet} = 0.1$. Other parameters can be determine using the relations

Table 6 Simulation conditions for dimensionless numbers under lattice unit through experiment *[45]*

Density ratio (γ_ρ)	Viscosity ratio (γ_ϑ)	Re	Fr
1.3	1.4	460	0.052

$$\gamma_\rho = \frac{\rho_{water}}{\rho_{oil}} \tag{68}$$

$$\gamma_\vartheta = \frac{\vartheta_{water}}{\vartheta_{oil}} \tag{69}$$

$$Re = \frac{U_{inlet} D_e}{\vartheta_{water}} \tag{70}$$

$$We = \frac{\rho_{water} U_{inlet}^2 D_e}{\sigma} \tag{71}$$

$$Fr = \frac{U_{inlet}^2}{g D_e} \tag{72}$$

$$Oh = \frac{We^{1/2}}{Re} \tag{73}$$

of dimensionless groups in lattice unit: $\rho_o = 1.98$, $\vartheta_w = 0.0043$, $\vartheta_o = 0.0031$ and $g = 1.0 \times 10^{-3}$. For the strength of interaction force of pseudopotential Shan/Chen model, as the previous validation simulations setup, we set $G_{w/w} = -5.13$, $G_{o/o} = -2.6$, $G_{wo} = 0.2$ and $G_{ow} = 1.0$. The total domain is decomposed into 16 sub-domains along the streamwise direction for the parallel computing using openMPI as Chapter 2 mentioned.

4.4 Results

The extension of Ohnesorege's classification for liquid-gas systems is mentioned in Satio, 2016 [45] and Satio, 2017 [23] both for experimental and numerical investigations. The classified breakup relationship between Reynolds number and Ohnesorege's number is shown in following Figure as four main regions: I, dripping; II, varicose breakup; III, sinuous breakup; and IV, atomization. Based on the observations and phenomenological considerations from the references Satio, 2016 [45] and Satio, 2017 [23], the flow-transition critical equations were derived:

$$Oh = 2.8Re^{-1}, \text{ for Regimes I, II and III} \tag{74}$$

$$Oh = 22Re^{-1}, \text{ for regimes III and IV} \tag{75}$$

where Reynolds number is defined as Eq. 70 and the Ohnesorge' number can be given by Eq 73. By using the above transition criteria, we can predict the breakup regimes of an immiscible liquid-liquid system jet from initial parameters.

In our Method low Reynolds number Lattice Boltzmann simulation, Re=460, as the Figure 44 predicted, the liquid-liquid jet flow-transition should locate in the regimes of I/II. We calculate the surface tension with Laplace analysis using Eq. 63, where, R and ΔP is the average of formation droplet radius and pressure difference cross the droplets for the global values, σ is the surface tension obtained through Laplace analysis and We and Oh is the corresponding Weber number and Ohnesorege number.

Table 7 Surface tension, Weber number and Oh number obtained through Laplace analysis

	D	ΔP	σ	We	Oh
LBM	20	0.142	0.79	0.65	1.75e-03
Experiment	7 (mm)	-	40 mN/m	0.63	1.73e-03

Figure 54 shows the instantaneous flow images for case Re=460. At t=600, the swollen part generates at the tip of jet, where the region close to the nozzle exit. The mushroom-like head does not appear at the low Reynolds number investigation. The swollen part moves downstream with the growth and generation of neck part at t=800. Then the corresponding part breaks up into a single and disjunct droplet at t=1000. At this point, the following swollen part generates at the tip of jet at the similar location as the previous swollen part on a liquid column. The formation of swollen part, the growth of neck part and the generation of breakup into a single disjunct droplet are observed through the simulation. In this low Reynolds number and Weber number case, a so-called satellite-droplet formation just after the primary droplet formation is not observed. This series of processes is a characteristic of the so-called pinch-off behavior [50]. This corresponds to the varicose breakup, which is locate in the regimes of II in Fig 56.

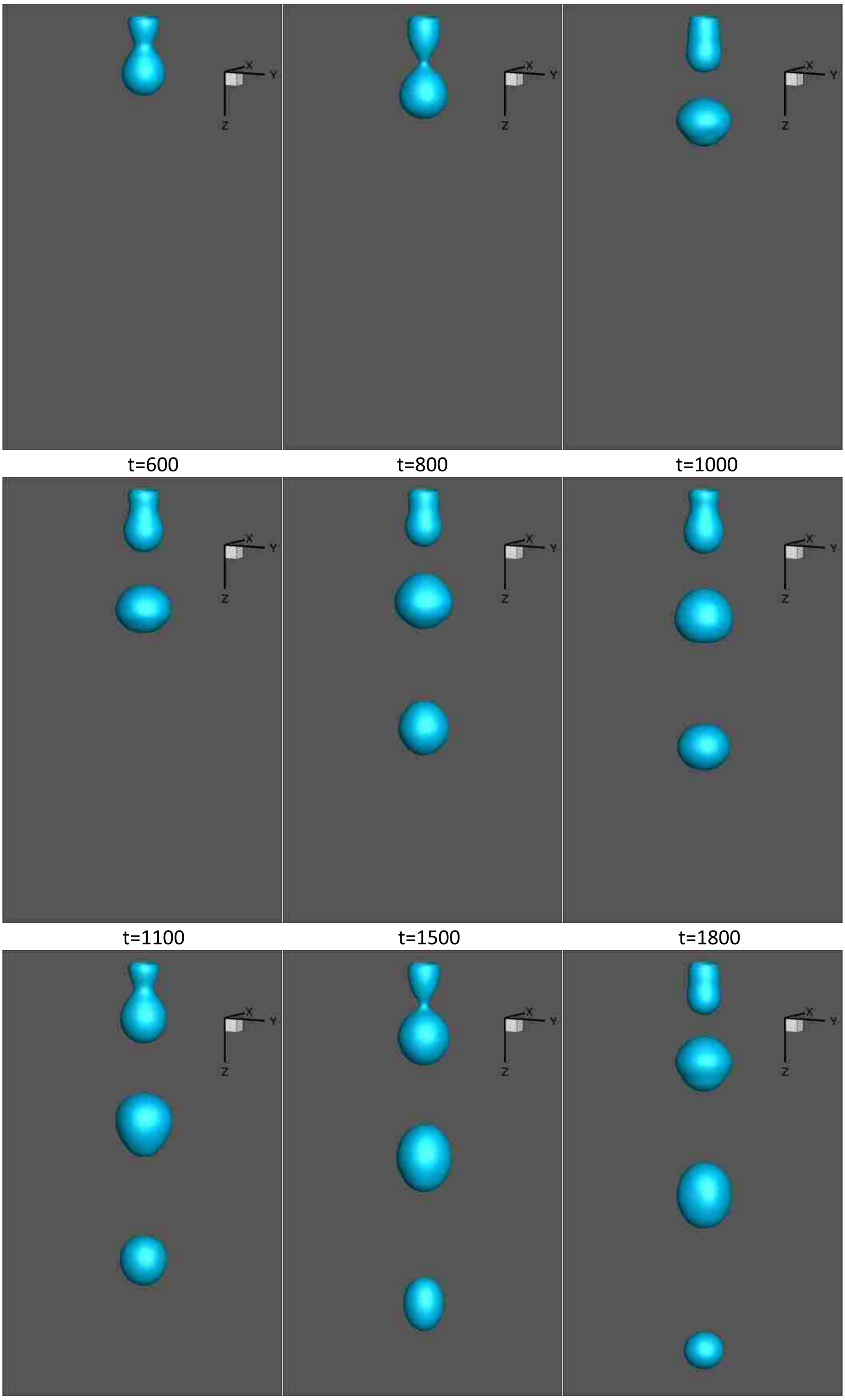

t=600 t=800 t=1000

t=1100 t=1500 t=1800

t=2100 t=2300 t=2500

Figure 54 Instantaneous flow images of Re=460 case: $\gamma_\rho = 1.3, \gamma_\vartheta = 1.4$ and We=1.52. The computation domain is set to be 100×100×300. A droplet forms mainly at the tip of jet; the character of varicose breakup (Regimes II) appear.

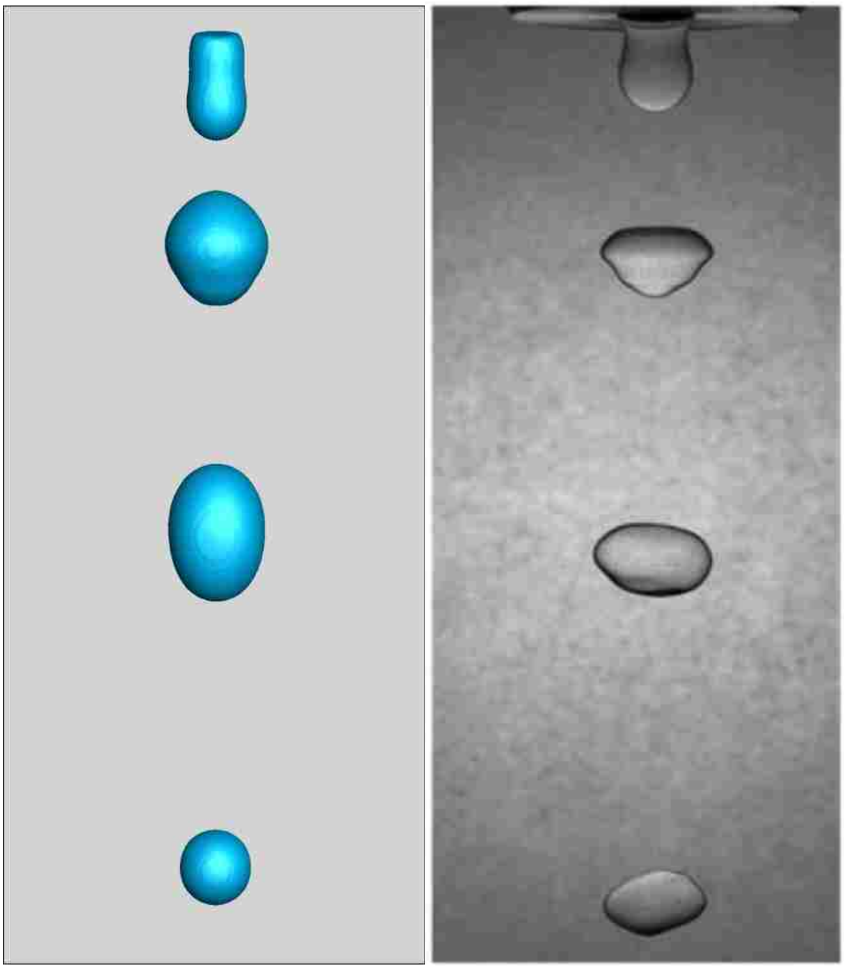

Figure 55 Flow images comparison of Re=460 case between pseudopotential LBM simulation and experiment *[45]*

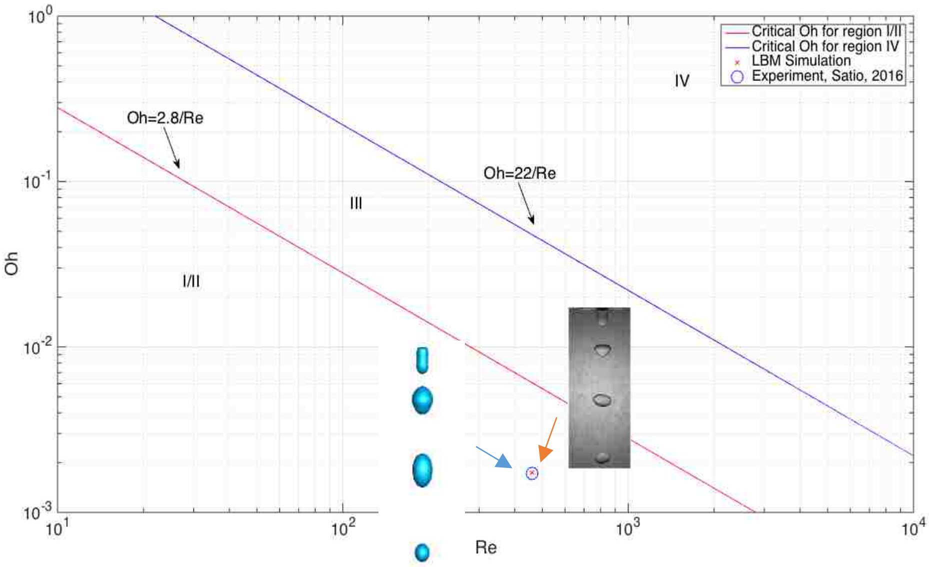

Figure 56 Comparison of the present result of Re=460 case in the dimensionless diagram

By choosing the parameters based on the regime map for jet breakup in liquid-liquid system circular jet, we performed simulations to evaluate the reproducibility of the regime map in the varicose regime. The pinch-off jet breakup phenomenon is observed, corresponding the droplet formation in the tip of the liquid column, occurred.

The Figure 55 shows the comparison of LBM simulation and experimental investigation by Satio et al [45] for same Reynolds number. Since the surface tension is not modified directly and calculated through Laplace analysis, we cannot reach the Weber number exactly same as the reference, which is We_{ref}=0.63. Thus, the Ohnesorege's number in our simulation is larger than that in the reference, which is $Oh_{ref} =$ 1.73e-03. We can observe the similar phenomenon, which we mentioned in previous discussion as pinch-off jet breakup, growth of neck part and single corresponding droplet formation in the tip of the jet. However, the core jet length in our simulation is longer than that in the reference, which is mainly corresponding the larger Weber number and Ohnesorege's number [23]. In other word, with setting the parameters of liquid-liquid jet system in our simulation, the jet breakup phenomenon is closer to regimes I (dripping) on the Oh-Re regimes map. On the other hand, the liquid-liquid jet breakup phenomenon is closer to regimes II (varicose) in the reference.

For higher Reynolds number and very high Weber number, our pseudopotential Shan/Chen Lattice Boltzmann Method always meet the numerical instability, and the parameters of interaction strength between same component and different components still need to be modified. Here, we investigate the high Reynolds number and Weber number case, Re=3400 and We=1.0e4, using openFOAM, and compare the results with reference.

The investigation is simulated by openFOAM 4.1. The STL file for the *snappyHexMesh* to patch the circular inlet on the top boundary were generated by MATLAB R2016b code. *snappyHexMesh* utility requires a base mesh for snapping. The results of simulation illustrate that the key length scale for development is about $16mm \times 16mm \times 40mm$, and the uniform mesh size is $\Delta x = 0.067mm$, and the domain size is $240 \times 240 \times 600$, correspondingly. We set the properties of two components as the table 8 shown.

Table 8 Physical properties of test fluids

	Dispersed phase	Continuous phase
Substance	Water	Silicon Oil
Density $[kg/m^3]$	997	766
Viscosity $[m^2/s]$	8.93×10^{-7}	6.38×10^{-7}
Interfacial tension $[mN/s^2]$	0.46×10^{-3}	

The nozzle exit diameter is $2mm$, and the uniform inlet velocity is set to $1.5181\ m/s$, correspondingly to reach the Reynolds number. The Weber number match the design value as $We = 1.0 \times 10^4$. With this Weber number, the Froude number is $Fr_{openFOAM} = 8.49$ with Eq. 72, which can match the reference value as $Fr_{reference} = 8.5$. Since the Froude number is different, some distinctions between the results of openFOAM simulation and that of reference are observed.

Table 9 Simulation conditions for dimensionless numbers to be invested

	Reynolds number (Re)	*Weber Number (We)*	*Ohnesorege's number (Oh)*	*Froude Number (Fr)*
openFOAM	3400	1.0×10^4	2.9×10^{-2}	8.49
Satio, et, al. 2017	3400	1.0×10^4	2.9×10^{-2}	8.5

The Figure 57 and Figure 58 are the Iso-surface flow images of openFOAM simulation and reference for $Re = 3400$ and $We = 1.0 \times 10^4$. The dimensionless number is obtained as Eq. 71, Eq. 72 and Eq. 73 and is shown in the above Table 9.

In the Iso-surface flow images of our simulation, a mushroom like head appears at very beginning time step at t=0.012s. Through t=0.012s-0.028s, the jet continues penetration with active entrainment. The liquid-liquid system jet primary breakup along the core jet part is presented, which is similar with low Reynolds number and low Weber number case. However, the core jet keeps continuous for this high Weber number. From t=0.04s, the liquid atomization phenomenon is observed. The sizes of the generated droplets is much smaller than the inlet diameter. In the downstream region, the secondary liquid-liquid system jet breakup is presented clearly, and the ligament between disconnected small droplets is observed. At t=0.052s, more droplets generated and spread out to ambient environment. In the downstream region, the liquid column is almost fully covered.

The Figure 58 is the flow images of reference Satio, et al [23]. Compared with the reference results, a mushroom like head, primary core jet breakup along the core jet part and secondary liquid jet atomization in the downstream region are observed at early time step both in openFOAM simulation and reference. However, for later time step, when the atomization phenomenon is observed, the number of unconnected droplets generated in the downstream region is smaller in our simulation. And the occupied downstream region with atomized liquid is larger in the reference than that in our simulation. The liquid-liquid system jet breakup characteristics expected by the Ohnesorege regime map, which we mentioned above is presented in the Figure 59.

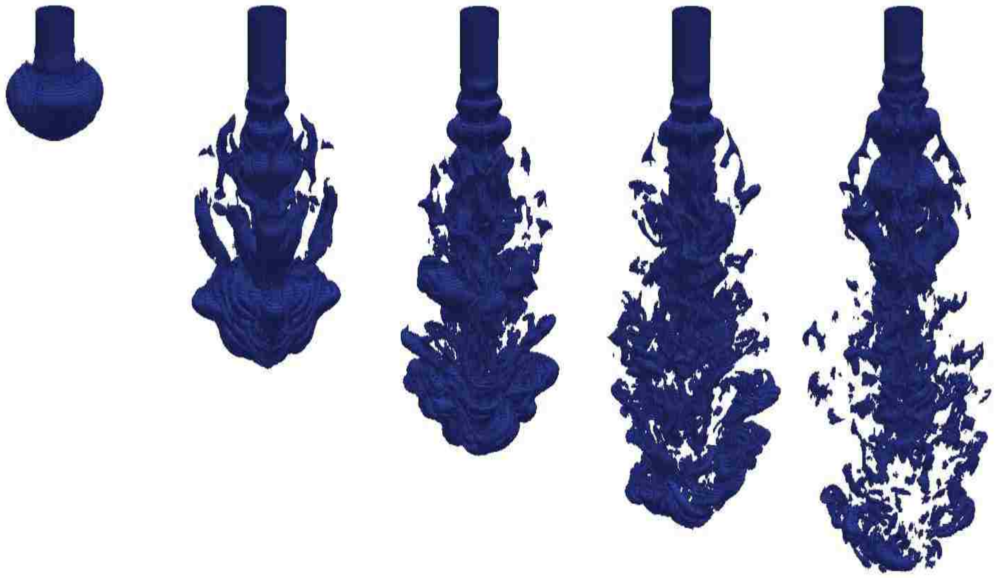

t=0.012s t=0.028s t=0.032s t=0.040s t=0.052s

Figure 57 Instantaneous Iso-surface flow images of Re=3400 case: $\gamma_\rho = 1.3$, $\gamma_\vartheta = 1.4$ and We=1×10^4. The computation domain is set to be $240 \times 240 \times 600$. the character of atomization breakup (Regimes IV) appear.

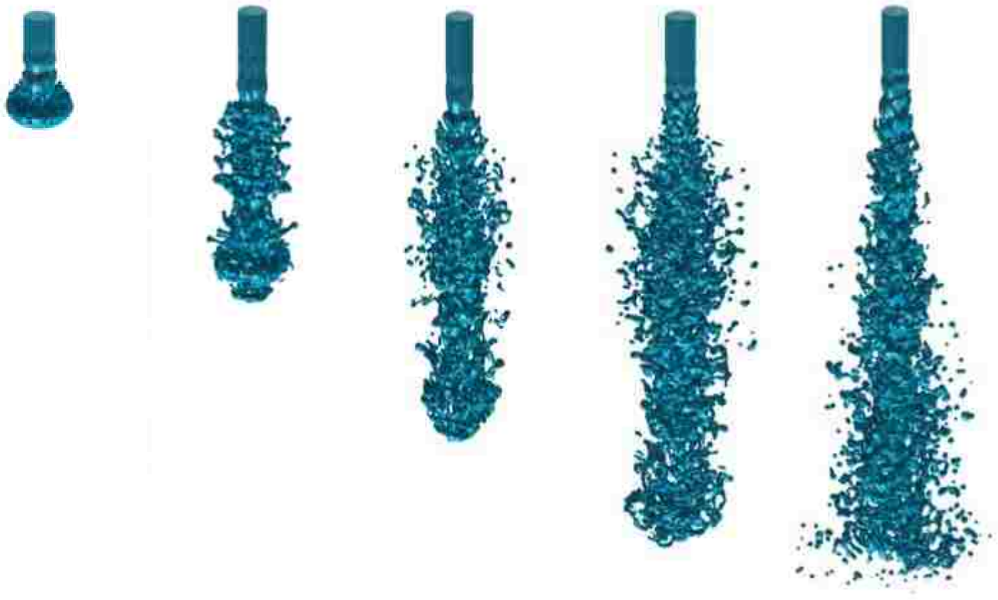

t=0.011s t=0.025s t=0.035s t=0.043s t=0.050s

Figure 58 Reference using color-fluid Lattice Boltzmann Method results of Re=3400, $\gamma_\rho = 1.3$, $\gamma_\vartheta = 1.4$, We=1×10^4 and Fr=8.5 case. The computational domain is set to be $240 \times 240 \times 600$. A large number of droplets are entrained from the jet surface; the character of atomization breakup (Regimes IV) appear.

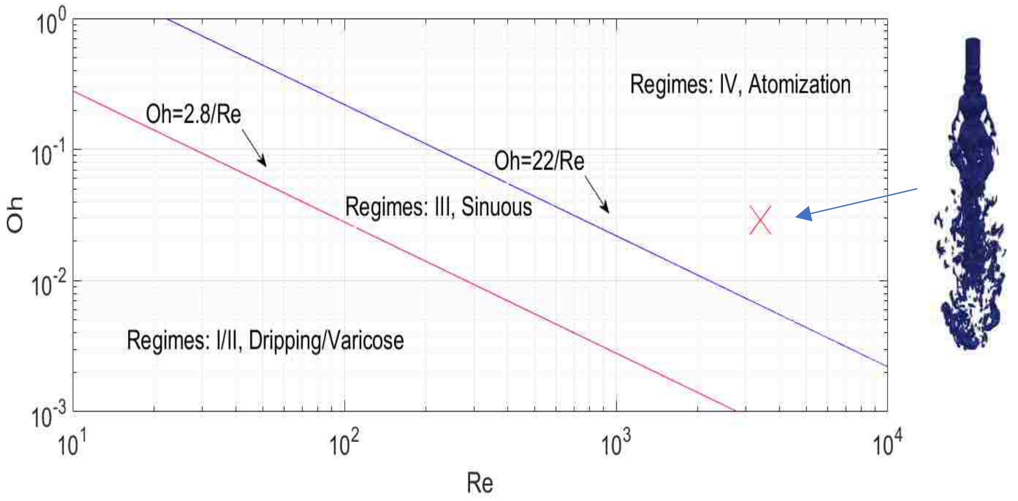

Figure 59 Summary of the openFOAM simulation result in the dimensionless diagram

4.5 Conclusion

In this chapter, the pseudopotential Shan/Chen multi-phase Lattice Boltzmann Method is discussed and implemented to different validation simulation cases and the liquid-liquid system jet breakup investigation. In the series of droplet simulations, with Laplace test, the clearly linear relationship between pressure difference cross two components interface and the reverse of droplet radius is presented. And through Laplace analysis, the surface tension can be obtained. The improved Shan/Chen model with modified Equation of State as P-R EOS is also discussed for large density ratio simulation. The diffusion effect between two different components is decreased to the significant level, and the amount of lattice which is occupied by the mixture fluid is limited to small number. After a series of droplet simulations with different interaction strength coefficients, which are between different components and between same component, we obtain the appropriate values for the designed dimensionless diameters and parameters to limit the diffusion effect and mixture fluid occupied space to reasonable level. For the fluid-solid validation, we test different fluid-solid interaction strength coefficient to reach the linear relationship between fluid-solid contact angle and strength of interaction for given parameters. With this relationship, the fluid-solid contact angle can be predicted. We investigate the low Reynolds number liquid-liquid system jet from circular orifice using pseudopotential Shan/Chen model at Re=460, and compare the results with Saito, et, al [45]. As the Ohnesorege regime map predicted, the pinch-off jet breakup phenomenon, corresponding droplet formation in the tip of the liquid column is observed and agree with varicose regime with Ohnesorege regime map. For high Reynolds number and very high Weber number case at Re=3400 and We=1×10^4, the results of openFOAM simulation is compared with the reference, Satio, et, al [45] and Satio, et, al [23]. The atomization phenomenon and a bunch of satellite droplets generation is observed. The liquid column is fully occupied with entrainment droplets, which are smaller than the nozzle exit diameter.

Chapter 5

Conclusion

Single phase and multiphase jet flows are investigated by employing Lattice Boltzmann Method. Single-phase jets issued from the circular and the 6-lobed orifice and multiphase jet issued from a circular orifice are considered. The LBM solver contains serval modules, which is developed by C++. The multi-block approach is applied for mesh refinement. Smagorinsky LES turbulence model is implemented for high Reynolds number flow simulations. The extrapolation method is used to impose boundary conditions along the curved surfaces. The pseudopotential Shan/Chen multi-phase model and improved Shan/Chen model with P-R EOS are adopted for the droplet validation and multiphase jet flow simulations. The numerical codes are parallelized by applying the openMP and openMPI approach. The LBM solver is validated by a series of benchmark simulations, and the results of LBM simulations are compared with results of experimental measurements.

We observed several flow regimes for single-phase jet flows for Reynolds number from 1050 to 6750. These distinct flow regimes are dominated by the jet breakup, the vortex generation, the jet decay and turbulence intensity. Flow regimes are identified and spatial and temporal characteristics of the flow are revealed by averaged and instantaneous profiles and flow images acquired various regions of the computational domain. For Re=1620, the flow is nearly laminar near the orifice. With weak dissipation of energy, the jet decay starts away from the jet orifice, and the jet spreads out to ambient at a low rate after the core jet structure breaks up. For

Re>1620 flows, a stronger dissipation, concomitant to a turbulent regime within the shear layer, is observed. The phenomenon of velocity decay can be captured at a location that is closer to the jet orifice exit, and jet expands and spreads radially out to ambient with a relatively higher rate compared to that for the lower Reynolds number jets.

Single-phase jets emanating from the 6-lobed orifice are simulated for Re=2700 and Re=72000. The velocity decay, vortex structures and turbulence intensity for jets issued from the 6-lobed orifice are compared with those for jets issued from the orifice. In the region near the orifice, the volumetric flow rate for the notched jet is significantly higher than that in the circular jet. It is shown that large ambient air is submerged at the orifice exit of the 6-lobed rectangular jet. The 6-lobed rectangular jet exhibits a higher net entrainment of the ambient fluid over the entire observed region. The higher initial rate of turbulent diffusion is reflected in a faster initial decay of the mean velocity although this appears to decrease with the axial distance. Similarly, the notched jet has a shorter unmixed core. In this region, its cross-sectional-averaged (major and minor plane) kinetic energy grows faster than that in circular jet. However, the 6-lobed jet also presents a higher rate of destruction of the turbulence kinetic energy.

For pseudopotential multi-phase solver validation, Laplace test and prediction of fluid-solid contact angle for two-dimensional and three-dimensional droplets. The Ohnesorege regime is observed, for low Reynolds number jets. The pinch-off jet breakup phenomenon, corresponding to the droplet formation in the tip of the liquid column is observed. For high Reynolds number and high Weber number multiphase jets, the results predicted by employing openFOAM solver agree reasonably well with those observed by reported experiments. Formation of the liquid atomization and the satellite dropletsis the main feature of the flow structures. Simulations are performed using parallel codes with openMP and openMPI algorithm developed by in house using the LINUX operation system.

5.1 Future work

Development of LBM model for high Reynolds number multi-phase jets

Simulations of multiphase jet flows at high Reynolds number and high Weber number are still challenging tasks for Lattice Boltzmann Method utilizing Shan/Chen pseudopotential model. In the present study, we only simulated multiphase jet flows for Reynolds number up to 500 and Weber number up to 10. The limitation is due to the surface tension and the strength of interaction force in Shan/Chen model. For the single-phase flow solver, however, high speed flow simulation is only limited by the lattice relaxation time, which is obtained from molecular viscosity and could be resolved with Smagorinsky LES model, or Entropy methods. Studying atomization flow regimes in these systems cannot be accomplished the method utilized in this study, and future study is needed to address this issue. In recent multiphase fluid flow jet simulation with Lattice Boltzmann Method, Satio et, al. [23] investigated the atomization phenomenum with high Reynolds number and Weber number using multi-relaxation time and color-fluid model with phase interface tracking. It is expected that a method with single-relaxation time with LES model, color-fluid model and openMPI parallel algorithm would be implemented for multiphase fluid flow jet atomizaition simulations.

References

[1] N.O.Systems, Gases. Processes, 1954.

[2] S. Chen and G. D. Doolen, "Lattice Boltzmann Method for fluid flows," *Annual Review of Fluid Mechanics,* p. 329, 1998.

[3] X. He and L. Luo, "Lattice Boltzmann Method for the incompressible Navier-Stokes Equation," *Journal of Statistical Physics,* vol. 88, pp. 927-944, 1997.

[4] P.L.Bhatnagar, E.P.Gross and M.Krook, "A Model for Collision Processes in Gases. I. Small Amplitude Processes in Charged and Neutral One-Component Systems," vol. 94, p. Physical Review, 1954.

[5] J. G. M. Eggels, "Direct and large-eddy simulation of turbulent fluid flow using the lattice-Boltzmann scheme," *International journal of heat and fluid flow,* vol. 17, no. 3, pp. 307-323, 1996.

[6] S. Chen, "A large-eddy-based lattice Boltzmann model for turbulent flow simulation," *Applied Mathematics and Computation,* vol. 215, pp. 591-598, 2009.

[7] Z. Guo, C. Zheng and B. Shi, "An extrapolation method for boundayr conditions in lattice Boltzmann method," *Physics of Fluids 14,* vol. 14, no. 6, 2007.

[8] A. Ladd, "Numerical simulations of particulate suspensions via a discretized Boltzmann equation. Part1. Theoretical foundation.," *Journal of Fluid Mechanics271,* pp. 285-309, 1994.

[9] R. Mei, L. Luo and W. Shyy, "An accurate curved boudnary treatment in the lattice Boltzmann method," *Journal of Computational Physics 155,* pp. 307-330, 1999.

[10] X. He and G. Doolen, "Lattice Boltzmann Method on Curvilinear Coordinates System: Flow around a Circular Cylinder," *Jouranl of Computational Physics,* vol. 134, pp. 306-315, 1997.

[11] Z. Lu, Y. Liao, D. Qian, J. Mclaughlin, J. J. Derksen and K. Kontomaris, "Large Eddy Simulations of a Stirred Tank Using the Lattice Boltzmann Method on a Nonuniform Grid," *Journal of Computational Physics,* vol. 181, pp. 675-704, 2002.

[12] Y.Peng and C.Shu, "Application of multi-block approach in the immersed boundary-Lattice Boltzmann method for viscous fluid flows," vol. 218, pp. 460-478, 2006.

[13] X. Shan and H. Chen, "Lattice Boltzmann model for simulating flows with multiple phases and components," *Physical Review E,* vol. 47, 1993.

[14] H. Huang, M. Krafczyk and X. Lu, "Forcing term in single-phase and Shan-Chen-type multiphase lattice Boltzmann models," *Physical Review E,* vol. 84, pp. 046710-1-046710-15, 2011.

[15] L. Chen, Q. Kang, Y. Mu and W.-Q. Tao, "Acritical review of the pseudopotential multiphase lattice Boltzmann model: Methods and applications," *International Journal of Heat and Mass Transfer,* pp. 210-236, 2014.

[16] H. Yu, L.S.Luo and S.S.Girimaji, "LES of turbulent square jet flow using a MRT Lattice Boltzmann model," *Computers & Fluids,* vol. 35, pp. 957-965, 2006.

[17] X. He and L.-S. Luo, "Some Progress in Lattice Boltzmann Method. Part I. Nonuniform Mesh Grids," *Journal of Computational Physics,* vol. 129, pp. 357-363, 1996.

[18] A. Fakhari and T. Lee, "Numerics of the Lattice Boltzmann Method on Nonuniform Grid: Standard LBM and Finite-difference LBM," *Computers & Fluids,* vol. 107, pp. 205-213, 2015.

[19] A. Fakhari and T. Lee, "Finite-difference lattice Boltzmann method with a block-structured adaptive-mesh-refinement technique," *Physical Review E,* vol. 89, pp. 033310-1-033310-12, 2014.

[20] Q. Zou and X. He, "On pressure and velocity boundary conditions for the lattice Boltzmann BGK model," *Physics of Fluids,* vol. 9, pp. 1591-1598, 1997.

[21] P. Yuan and L. Schaefer, "Equations of state in a lattice Boltzmann model," *Physics of Fluids,* vol. 18, pp. 042101-1-042101-11, 2006.

[22] J. Bao and L. Schaefer, "Lattice Boltzmann equation model for multi-component multi-phase flow with high density ratios," *Applied Mathematical Modelling,* vol. 37, pp. 1860-1871, 2013.

[23] S. Saito, Y. Abe and K. Koyama, "Lattice Boltzmann modeling and simulation of liquid jet breakup," *Physical Review E,* vol. 96, pp. 013317-1-013317-18, 2017.

[24] V. Todde, S. P.G. and M. Sandberg, "Experimental analysis of low-Reynolds number free jets," *Experimental Fluids,* vol. 47, pp. 279-294, 2009.

[25] F. F. Grinstein, "Vortex dynamics and entrainment in rectangular free jets," *Journal of Fluid Mechanics,* vol. 437, pp. 69-101, 2001.

[26] P. O'Neill, J. Soria and D. Honnery, "The stability of low Reynolds number round jets," *Experiments in Fluids,* vol. 36, pp. 473-483, 2004.

[27] W. R. Quinn and J. Milizer, "Experimental and numerical study of a turbulent free square jet," *Physics of Fluids,* vol. 31, pp. 1017-1025, 1988.

[28] I. Nastase, A. Meslem and P. Gervais, "Primary and secondary vortical structures contribution in the entrainment of low Reynolds number jet flows," *Exp Fluids,* vol. 44, pp. 1027-1033, 2008.

[29] M. E. Hassan, A. Meslem and K. Abed-Meraim, "Experimental investigation of the flow in the near-field of a cross-shaped orifice jet," *Physics of FLuids,* vol. 23, pp. 045101-1-045101-16, 2011.

[30] J. Mi, J. Nathan and R. E. Luxton, "Centreline mixing characteristics of jets from nine differently shaped nozzles," *Experiments in Fluids,* vol. 28, pp. 93-94, 2000.

[31] F. Grinstein, E. Gutmark and T. Parr, "Near field dynamics of subsonic free square jets. A computational and experimental study," *Phys. Fluids,* vol. 7, pp. 1483-1497, 1995.

[32] A. Meslen, R. Greffet, I. Nastase and A. Ammar, "Experimental investigation of jets from rectangular six-lobed and round orifices at very low Reynolds number," *Meccanica,* vol. 49, pp. 2419-2437, 2014.

[33] J. Mi, P. Kalt and J. Nathan, "On Turbulent Jets Issuing from Notched-Rectangular and Circular Orifice Plates," *Flow Turbulence Combust,* vol. 84, pp. 565-582, 2010.

[34] M. Junk and Z. Yang, "Outflow boundary conditions for the latticec Boltzmann method," *Progress in Computational Fluid Dynamics,* vol. 8, pp. 38-48, 2008.

[35] D. Y. M. T. G. K. G.V. Papaioannou, "On the effect of spacing on the vortex-induced vibrations of two tandem cylinders," *Journal of Fluids and Structures,* vol. 24, pp. 833-854, 2008.

[36] J. Lin, R. Jiang, Z. Chen and X. Ku, "Poiseuille flow-induced vibrations of two cylinders in tandem," *Journal of FLuids and structures,* vol. 40, pp. 70-85, 2013.

[37] J. J. Flora and V. W. Coldschmidt, "Virtual Origins of a Free Plane Turbulent Jet," *AIAA,* vol. 7, pp. 2344-2346, 1963.

[38] A. N. KOLMOGOROV, "The Local Structure of Turbulence in Incompressible Viscous Fluid for Very Large Reynolds' Numbers," *Doklady Akademiia Nauk SSSR,* vol. 30, pp. 301-305, 1941.

[39] H. Hu, T. Saga, T. Kobayashi and N. Taniguchi, "Mixing Process in a Lobed Jet Flow," *AIAA,* vol. 40, pp. 1339-1345, 2002.

[40] F. F. Grinstein, "Self-induced vortex ring dynamics in subsonic rectangular jets," *Physics of FLuids,* vol. 7, pp. 2519-2521, 1994.

[41] X. Yang and A. Turan, "Simulation of liquid jet atomization coupled with forced perturbation," *Physics of Fluids,* vol. 29, pp. 022103-1-022103-12, 2017.

[42] J. Shinjo and A. Umemura, "Simulation of liquid jet primary breakup: Dynamics of ligament and droplet formation," *International Journal of Multiphase Flow,* vol. 36, pp. 513-532, 2010.

[43] I. L. Omocea, C. Patrascu, M. Turcanu and C. Balan, "Breakup of Liquid Jets," in *Sustainable Solutions for Energy and Environment*, Bucharest, Romania, 2015.

[44] L. S. P. and Z. W. Lian, "Mechanisms of the Breakup of Liquid Jets," *AIAA,* vol. 28, pp. 121-126, 1990.

[45] S. Saito, Y. Iwasawa, A. Kaneko and T. Kanagawa, "Jet Breakup and Droplet Formation in Immiscible Liquid-Liquid System," in *24th International Conference on Nuclear Engineering*, Charlotte, North Carolina, 2016.

[46] R. Zhang, X. He, G. Doolen and S. Chen, "Surface tension effects on two-dimensional two-phase Kelvin-Helmholtz instabilities," *Advances in Water Resources,* vol. 24, pp. 461-478, 2001.

[47] V. A. Lubarda and K. A. Talke, "Analysis of the Equilibrium Droplet Shape Based on an Ellipsoidal Droplet Model," *Langmuir,* vol. 27, pp. 10705-10713, 2011.

[48] A. Komrakova, O. Shardt, D. Eskin and J. Derksen, "Lattice Boltzmann simulations of drop deformation and breakup in shear flow," *International Journal of Multiphase Flow,* vol. 59, pp. 24-43, 2014.

[49] J. Wu, "Dynamics of falling droplets impact on a liquid film: Hybrid lattice Boltzmann simulation," *Colloids and Surface A: Physicochem. Eng. Aspects,* vol. 472, pp. 92-100, 2015.

[50] S. P. Lin and R. D. Reitz, "Drop and Spray Formation from a Liquid Jet," *Annu. Rev. Fluid Mech,* vol. 30, pp. 85-105, 1998.

[51] C. Ji and D. Zhao, "Lattice Boltzmann investigation of acoustic damping mechanicsm and performance of an in-duct circular orifice," *Journal of the Acoustical Society of America,* pp. 3243-3251, 2014.

[52] J. Lin, R. C. Z. Jiang and X. Ku, "Poiseuille flow-induced vibrations of two cylinders in trandem," *Journal of Fluids and Structures,* vol. 40, pp. 70-85, 2013.

[53] K. Zaman and F. Wang, "Noise, Turbulence, and Thrust of Subsonic Free Jets from Lobed Nozzles," in *40th AIAA Aerospace Sciences Meeting & Exhibit*, Reno, NV, 2002.

[54] K. B. M. Q. ZAMAN, "Axis switching and spreading of an asymmetric jet: the role of coherent structure dynamics," *Journal of Fluid Mechanics,* vol. 316, pp. 1-27, 1995.

[55] W. v. Ohnesorge, *Applied Mathematics and Mechanics,* vol. 16, p. 355, 1936.

[56] B. Dauyeshova, L. Rojas-Solorzano and E. Monaco, "Study of the Motion of a Droplet in a Microchannel using Shan-Chen Multiphase Lattice Boltzmann Model," *Chemical Engineering Transactions,* vol. 57, 2017.

[57] C. Nor Azwadi and A. W. M.Y., "Simulation of multicomponent multiphase flow using lattice Boltzmann method," in *The 4th International Meeting of Advances in Thermofluids AIP Conf Proc.*, 2012.

[58] C. Josserand and S. Thoroddsen, "Drop Impact on a Solid Surface," in *Annu. Rev. Fluid Mech*, 2016.

[59] W. v. Hoeve, G. Stephane, J. H. Snoeijer and M. Versluis, "Breakup of diminutive Rayleigh jets," *Physics of Fluids,* vol. 22, pp. 122003-1-122003-11, 2010.

VITA

Yang Chen was born on May 24, 1988 in Dongyiing, Shandong, China. His father is Yuangang Chen and mother Jinchuan Shi. Yang attended Beijing Chaoyang Foreign Language School, where his passion for math and physics got excited. He graduated from high school in June of 2006. Yang enrolled at Sun Yat-Sen University in September of 2006 and received his Bachelor of Science in Theoretical and Applied Mechanics degree in June 2010. In January 2011, Yang went to Lehigh University in Bethlehem, Pennsylvania. There, he mainly worked on Lattice Boltzmann Method and implement LBM into multiple simulations of single-phase and multi-phase air and liquid jet projects. He received his Master of Science in Mechanical Engineering degree in February 2013. Yang pursed his doctoral degree and received in September 2018.